

Seismic and stability analysis of component-based extraterrestrial vaults



Master's Thesis
Peter Manos

Seismic and stability analysis of component-based extraterrestrial vaults

Thesis by
Peter Lukasz Manos

In Partial Fulfilment of the Requirements for the
Degree of
Master of Science

Defended 10 February 2023



DELFT UNIVERSITY OF TECHNOLOGY
Delft, Netherlands

Graduation Committee

Dr. Anjali Mehrotra – TU Delft, *Chair & Daily Supervisor*
Dr. Marina Konstantatou – Foster + Partners, *Daily Supervisor*
Dr. Giorgia Giardina – TU Delft
Dr. Mariana Popescu – TU Delft

For my friends and family, near and far.

ACKNOWLEDGEMENTS

Firstly, I am profoundly grateful to my co-supervisors, Dr. Anjali Mehrotra and Dr. Marina Konstantatou for the patience and steadfast support they've given me during the past year. They truly helped me get as much out of this project as possible. I would like to sincerely thank them for the unique and exciting opportunities that they made possible, from speaking at ICONHIC 2022 in Athens, to model-making at the F + P headquarters. I've continuously felt a remarkable sense of appreciation for their encouragement.

I would also like to thank Dr. Giorgia Giardina and Dr. Mariana Popescu for their help and understanding throughout my journey towards completing my master's degree. I greatly value the perspectives they shared during our meetings.

I would like to extend my gratitude to everyone at the Specialist Modelling Group for their input and support during my brief stay in London. I cherished the opportunity to spend time with such a bright team of design professionals.

I am thankful for all my friends from TU Delft that uplifted me throughout the past few years, as well as my friends from back home who were always around for a call or a game of online chess, no matter the time difference.

Lastly, I would like to thank my family for their love and understanding. None of this would have been possible without their support.

ABSTRACT

For the first time since the 1970s, concrete plans are in motion to bring humans back to the Moon through the Artemis programme. The dawning era of space exploration aims to set the groundwork for long-term off-Earth settlement, with sights on bringing the first humans to Mars. In order to provide a safe means of inhabiting extraterrestrial (ET) environments, a self-supporting habitat shield concept has been developed by the Specialist Modelling Group at Foster + Partners, which is based on the use of mechanically interlocking masonry manufactured from in-situ resources. Significant progress must still be made in the structural design and validation of such systems, however, before they can be safely implemented. Due to the novelty of the proposed structure, existing research does not provide numerical evidence of its stability under self-weight, or under seismic loading. Research in this direction is valuable, as it explores alternatives to popular design concepts based on monolithic additive manufacturing and addresses research gaps related to the analysis of mechanically interlocking structures.

The aim of this project is to provide novel insight into the stability of self-supporting dry-stone vaults under the influence of microgravity and ground motions. This is achieved through a three-part analysis approach, which starts with an investigation into the fundamental structural behaviour of dry-stone, Nubian-type vaults based on a series of parametric studies. Key geometric parameters of the vaults are varied, and the resulting distinct element models are subjected to quasi-static pushover-type analysis in 3DEC. The parametric studies indicate what configuration of the vault geometry can maximise seismic capacity. This optimal vault geometry is modelled in Rhino using geometric constraint solving, which is used to produce a model which can be assembled from mechanically-interlocking components. Through pushover-type testing and dynamic time-history analysis, the performance of the resulting vault model is assessed with respect to possible moonquake loading. The final part of the design process accounts for uncertainties in material properties by conducting sensitivity studies, which indicate what degree of variation in performance is possible.

After completing the three main sets of analysis needed to design a moonquake-resistant vault, several comparative analyses are carried out to provide context to the structural performance of the Nubian-type vault. The first of these additional investigations models an equivalent monolithic vault geometry in DIANA and conducts finite element analysis to determine its capacity for lateral acceleration. The second comparative study determines how covering the vault in loose regolith may influence its structural performance. The third study investigates how the variation of gravity affects the stability and seismic performance of the vault.

Several key findings are obtained in this project, leading to an understanding of the structural behaviour of Nubian-type vaults and how they may be a possible solution to shielding demands in ET contexts. The final vault model was shown to remain stable under a uniform lateral acceleration equivalent to the PGA for a possible moonquake with a 475-year return period. Dynamic analysis conducted using an artificial ground motion record obtained for the same return period produced less favourable results, resulting in partial collapse of the outermost six courses of the vault. Computational constraints necessitated the imple-

mentation of an undamped analysis, however, so these results are considered to be conservative. Further analysis is needed, but these results suggest that with minor adjustments, the vault may be able to safely resist moonquake loading. The comparative monolithic vault analysis demonstrates that an additively manufactured vault may provide slightly better resistance to static lateral acceleration than a component-based vault. When considering the structural redundancy and energy dissipation necessary for safe seismic design, however, the discrete vault is expected to perform better. Results show that covering the vault in loose regolith is expected to reduce its overall stiffness. Conclusions about changes in stability cannot be made with confidence due to modelling issues at the interface between the regolith and the structure. By studying the influence of gravitational variation on the vault, results indicate that it may perform favourably on the Earth or on Mars, though the possibility of material damage must be studied further.

TABLE OF CONTENTS

Acknowledgements	iii
Abstract	iv
Table of Contents	vi
List of Illustrations	viii
List of Tables	xi
Chapter I: Introduction	1
1.1 Motivation	1
1.2 Objectives	2
1.3 Scope	3
Chapter II: Literature Review	5
2.1 Overview	5
2.2 Design context	5
2.3 Seismic hazard definition	10
2.4 Structural analysis of dry-stone masonry	15
2.5 Material definition	18
Chapter III: Modelling framework	22
3.1 Overview	22
3.2 Geometric definitions	23
3.3 Geometric constraint solving	26
3.4 Resulting vault model	27
3.5 Distinct element modelling	29
Chapter IV: Numerical analysis framework	31
4.1 Overview	31
4.2 Boundary conditions	31
4.3 Block type	32
4.4 Material definition	33
4.5 Configuration of quasi-static analyses	35
4.6 Configuration of dynamic analyses	36
Chapter V: Analysis Phase I - Parametric studies of idealised vault geometry	39
5.1 Overview	39
5.2 Methodology	39
5.3 Results	44
5.4 Discussion	48
Chapter VI: Analysis Phase II – Assessment of simulated vault geometry	52
6.1 Overview	52
6.2 Methodology	53
6.3 Results	56
6.4 Discussion	63
Chapter VII: Analysis Phase III - Material sensitivity studies	66
7.1 Overview	66
7.2 Methodology	67

7.3	Results	69
7.4	Discussion	72
Chapter VIII:	Comparative Analysis I - Equivalent monolithic vault	74
8.1	Overview	74
8.2	Methodology	74
8.3	Results	78
8.4	Discussion	81
Chapter IX:	Comparative Analysis II - Regolith overburden	83
9.1	Overview	83
9.2	Methodology	83
9.3	Results	85
9.4	Discussion	87
Chapter X:	Comparative Analysis III - Variation of gravity	89
10.1	Overview	89
10.2	Methodology	89
10.3	Results	89
10.4	Discussion	91
Chapter XI:	Conclusions	93
11.1	Summary	93
11.2	Scientific contributions	99
11.3	Future research	99
Bibliography		101
Appendix A:	Addenda for Chapter VI	107
1.1	Subcontact density variation	107
1.2	Local stability analysis	108
Appendix B:	Addenda for Chapter VIII	110
2.1	Preliminary analysis with tetrahedral mesh	110
2.2	Mesh refinement study	111

LIST OF ILLUSTRATIONS

<i>Number</i>	<i>Page</i>
1.1 Overall project structure	3
2.1 Comparison between AM and discrete assembly of vaulted structure (Konstantatou et al., 2021)	7
2.2 Illustration of planar topological interlocking (Dyskin et al., 2005)	7
2.3 Possible configurations of proposed component geometry (Konstantatou et al., 2022)	8
2.4 Proposed vault geometry informed by dimensions of a habitat module (Konstantatou et al., 2022)	9
2.5 Comparison between vault types investigated by Ochsendorf and Block (2009)	10
2.6 Overview of a) Apollo seismic network and b) Lunar structure and moonquake sources	11
2.7 Uniform hazard spectra (Ruiz et al., 2022)	13
2.8 Point contact representation (Gonen et al., 2021)	17
2.9 3DEC calculation cycle (Itasca Consulting Group Inc., 2019)	17
2.10 Illustration of PBF-related manufacturing processes (Karl et al., 2022)	20
2.11 Illustration of microwave sintering apparatus Farries et al. (2021)	21
3.1 Modelling tools	22
3.2 Illustration of 3DEC-compatible component	24
3.3 Parametric variation of component geometry	24
3.4 Generation of input geometry	25
3.5 Tessellation detail for initial vault model	25
3.6 Flowchart of logic for Kangaroo simulation	27
3.7 Resulting geometry	28
3.8 Continuity enforcement	28
3.9 Rigid block model generation	29
3.10 Deformable block model generation	29
4.1 Illustration of boundary conditions	32
4.2 Illustration of potential foundation system leading to fixed condition of ground blocks	32
4.3 Illustration of in-plane and out-of-plane interface spacing	34
4.4 Illustration of irregularities with in-plane interface spacing for simulated courses	34
4.5 Pushover script flowchart	35
4.6 Application of ground motion data in 3DEC	36
4.7 SimQKE configuration	37
4.8 Dynamic input configuration	38
5.1 Analysis Phase I workflow	40
5.2 Idealised arch modelling procedure	40

5.3	Illustration of offset joint pattern employed for idealised vault modelling	41
5.4	Variation of component width	41
5.5	Variation of inclination	42
5.6	Overhang for 0.25 m wide components with a 25° inclination	42
5.7	Deviation of thrust line shape from funicular curve	43
5.8	Vault model at different construction stages	43
5.9	Variation of inclination for various component widths (realTL)	45
5.10	Variation of width for various inclinations (realTL)	46
5.11	Problematic tessellation	46
5.12	Variation of inclination for 0.5 m component width	47
5.13	Comparison between thrust line shapes for a component width of 0.5 m and varying inclination	48
5.14	Variation of course number (realTL)	49
5.15	1.5 m width, 45° inclination model; X-displacement contour plot	49
5.16	Final model state for 0.5 m component width and 45° inclination	50
6.1	Analysis Phase II workflow	52
6.2	Component comparison (dimensions in mm)	53
6.3	Gridpoint tracking for staged vault models	54
6.4	Final vault model in 3DEC	55
6.5	Course number variation for simple components	57
6.6	Course number variation for complex components	57
6.7	Comparison of complex, simple, and ideal component results	58
6.8	Demonstration of residual deformation present after unloading	59
6.9	Extended loading and unloading	59
6.10	Velocity vectors showing convergence under design acceleration	60
6.11	Natural modes of final vault model	61
6.12	Time history of relative displacement	62
6.13	Damage due to moonquake	62
6.14	Post-moonquake stability	63
7.1	Analysis Phase III workflow diagram	66
7.2	Matching pushover curves	67
7.3	Contour plots of displacement in X-direction	68
7.4	Component friction angle variation	70
7.5	Component interface stiffness variation	70
7.6	Wedge friction angle variation	71
7.7	Wedge interface stiffness variation	71
7.8	Influence of friction angle in Mohr-Coulomb joint model (Itasca Consulting Group Inc., 2019) .	72
8.1	Monolithic vault modelling approach	75
8.2	DIANA FEA model	75

8.3	Monolithic vault boundary condition properties	76
8.4	Tracking point definition	78
8.5	Pushover analysis of monolithic vault	79
8.6	Principal stresses in monolithic vault state before failure	79
8.7	Natural modes of monolithic vault	80
8.8	Monolithic vs. discrete pushover	82
9.1	Model with regolith overburden	84
9.2	Comparison between arch pushover behaviour with and without overburden	86
9.3	Comparison between arch displacement magnitudes under self-weight	86
9.4	Comparison between arch displacement magnitudes at failure	87
9.5	Detail of failed regolith model	88
10.1	Pushover plots for Earth, Moon, and Mars	90
10.2	Pushover plots for Earth, Moon, and Mars (locally normalised)	90
10.3	Comparison of final model states for varying gravity	91
10.4	Out of plane instability in final model state (g_{Earth})	92
A.1	Matching simple and complex component behaviour through subcontact edge length	107
A.2	Models with partially completed courses; a) 8 components; b) 12 components; c) 16 components; d) 20 components	109
A.3	Equilibrium under self-weight for models with partially completed courses; a) 8 components; b) 12 components; c) 16 components; d) 20 components	109
B.1	Principal stress contour plot at onset of failure in vault modelled with tetrahedral elements	110
B.2	Principal stress contour plot at onset of failure in vault modelled with hexahedral elements	111
B.3	Mesh convergence plot	112

LIST OF TABLES

<i>Number</i>	<i>Page</i>
2.1 Variation of relative density for Lunar regolith - adapted from Heiken et al. (1992)	18
2.2 Mechanical properties of GRC-3 Lunar regolith simulant (Dewoolkar et al., 2018)	19
2.3 Mechanical properties of sintered regolith (Indyk & Benaroya, 2017)	21
4.1 Assumed interface properties	34
6.1 Natural modes of final vault model	61
7.1 Comparison between properties of equivalent simple components and complex components	69
8.1 Monolithic vault material properties	77
8.2 Natural mode comparison between discrete and monolithic vaults	82
9.1 Deformable block constitutive definition	85
B.1 Maximum principal stresses for different element sizes	112

Chapter 1

INTRODUCTION

1.1 Motivation

Increased institutional and corporate investment into furthering prospects of permanent off-Earth habitation has triggered growing interest in the design of extraterrestrial (ET) infrastructure. This presents exciting opportunities for the architecture, engineering, and construction (AEC) industry to learn how to adapt to extreme conditions found outside Earth, and to use these insights to improve terrestrial design practices. Due to the acute scarcity of processed structural material, labour, machinery, and miscellaneous imports, infrastructural designs should be based on in-situ resource utilisation (ISRU), automated fabrication techniques, and reusability. Aside from severe resource constraints, extraterrestrial environments are characterised by a unique set of natural hazards, namely seismicity, meteorites, extreme temperatures, and radiation. These hazards generate risks that present challenges for the development of safe habitation systems. Popular proposals for permanent off-Earth habitats are based on inflatable, deployable, or 3D-printed structures, but their development has not progressed significantly beyond conceptualisation (Kalapodis et al., 2020). The structural design of extraterrestrial structures must undergo significant development before they can be safely implemented.

Recent studies regarding the design of off-Earth infrastructure tend to focus on the use of additive manufacturing (AM) to fabricate continuous geometries, specifically shield structures. Shielding is needed to protect a wide range of assets such as habitats, vehicles, or other mission infrastructure from space hazards (Sanders & Larson, 2013). Novel research is being developed, which investigates the design of such structures based on the arrangement of discrete, brick-like interlocking components rather than on AM. Such component-based systems offer several advantages over 3D-printed monolithic structures, namely the potential for reconfiguration and reuse. The use of interlocking elements decouples fabrication from assembly, which increases process robustness and promotes a circular (ISRU) framework. Furthermore, these elements can be fabricated without the use of imported materials via mature technologies based on sintering techniques. Such methods are used extensively in ceramics manufacturing on Earth and have been shown to produce high-strength samples from Lunar regolith simulants (Meurisse et al., 2017). As such, discrete assembly is seen as a promising fabrication technique for extraterrestrial structures, but further research in this field must be done to assess its feasibility. Several component-based design concepts have been proposed for extraterrestrial applications, but their structural design must be explored in more detail.

Konstantatou et al. (2022) propose a two-fold assembly and structural design methodology which can be used to derive geometries for self-supporting, component-based structures. This framework is underpinned by the development of a bespoke mechanically interlocking system which enables mortarless construction. Form finding techniques were used to derive structural forms which could efficiently resist their own

weight in a compression-only manner. This approach marks a shift away from the precedent set by existing proposals for component-based extraterrestrial infrastructure, which investigate the use of topologically interlocking components (Dyskin et al., 2005; Imhof et al., 2017). Structures based on topological interlocking are typically designed in a top-down way, with a global geometry leading to a discretisation based on unique components. In the framework developed by Konstantatou et al. (2022), however, various structural configurations can be obtained using a repeating unit geometry. Amongst these structural configurations, Nubian-type vaults, also known as pitched-brick vaults, offer a particularly compelling solution to shielding demands. Unlike conventional barrel vaults, these structures are composed of inclined masonry courses, which allows for scaffoldless construction. This aspect is particularly appealing in extraterrestrial contexts, where there is a significant cost incentive to limit dependency on additional machinery or temporary support structures.

The performance of the component-based, self-supporting vault developed by Konstantatou et al. (2022) has not been investigated — specifically in relation to natural hazards such as moonquakes — so structural analysis is needed to assess its viability. Moreover, the structural performance of systems belonging to this category has not been thoroughly examined in literature, which provides an opportunity for this project to contribute novel insight into the behaviour of interlocking, dry-stone component assemblies.

1.2 Objectives

The main objective of this thesis project is to analyse the stability of self-supporting dry-stone vaults proposed by Konstantatou et al. (2022) under the combined influence of microgravity and seismic loading. The main research question and the sub-questions that are addressed in this project are:

"How do pitched-brick vaults composed of regolith-based mechanically interlocking components perform under the combined effects of microgravity and ground motion present on the Moon?"

- What is the influence of component width and course inclination on the performance of these structures?
- How does the stability of these structures evolve throughout different stages of the construction process?
- Can these structures safely resist moonquake loading?
- What is the dynamic response of the structures when subjected to Lunar ground motions?
- How does the performance of an assembly of interlocking components compare to that of an equivalent monolithic structure?
- How does the addition of a covering of loose regolith influence the stability and seismic response of the completed structures?
- How does gravity influence the stability and seismic performance of these structures?

1.3 Scope

In order to fulfil the objectives stated above, a framework for the modelling and analysis of component-based structures is developed, which is then implemented in the preliminary design of a vault that may resist expected moonquake loading. A Lunar setting is assumed because conditions on the Moon are expected to lead to more extreme loading than on Mars, but the methodology presented in this thesis can readily be adapted to different environments. An overview of the scope and structure of the project is provided in Figure 1.1.

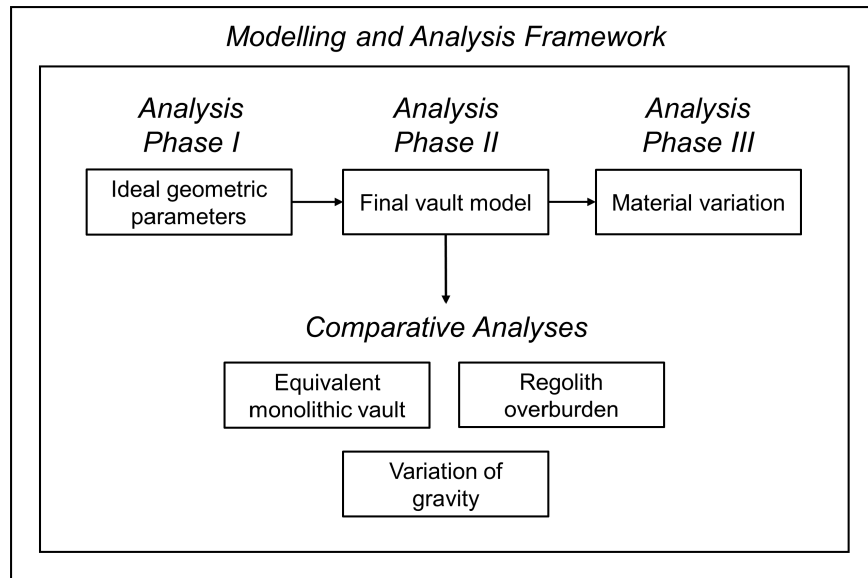


Figure 1.1: Overall project structure

In Chapter 2, a comprehensive literature review is conducted. Within the scope of this phase is a review of existing design concepts for extraterrestrial structures, as well as mortarless and scaffoldless masonry structures on Earth. Literature about extraterrestrial natural hazards is studied, with particular focus on ground motions. Sources on engineering seismology are studied in order to understand how to simulate time-histories of Lunar ground motions. Analytical and numerical tools are reviewed which can be used for the analysis of dry-stone masonry. Existing numerical analyses of masonry structures are used to inform the research methodology for this project. The properties of regolith, regolith simulants, and potential component manufacturing techniques are studied. This information is used to determine appropriate constitutive definitions in the numerical models.

In Chapter 3, the modelling framework is presented. Parametric modelling is carried out using Grasshopper in Rhino 7 (Robert McNeel & Associates, 2020), which generates models of the proposed vault according to a given component geometry. Emphasis is placed on accurately modelling the interlocking connections, which is accomplished using geometric constraint solving. A method for translating the model geometry into a format compatible with numerical analysis software is presented at the end of Chapter 3. Detailed modelling of the foundation system and other considerations relating to soil-structure interaction are not within the scope of this project.

In Chapter 4, a framework which defines the numerical analysis methodology is presented. This chapter provides details about assumptions which are common to all of the analyses carried out in the project, namely regarding boundary conditions, block definition, constitutive laws and application of seismic loading. This framework is applied to several phases of analysis, which build on each other to aid the design of a vault structure.

In Chapter 5, the first Analysis Phase is presented, which consists of a parametric study of idealised vault models. Components in these models do not interlock mechanically, and their shapes are defined based on ideal stereotomy of a constant-thickness arch. Through idealisation of the vault geometry, the influence of irregular tessellation and mechanical interlocking present in the real vault model is removed. In this way, the analyses carried out in this chapter aim to provide insight into the fundamental structural behaviour of dry-stone, Nubian-type vaults, which is absent in existing literature. These results help define an appropriate geometric configuration for a real, unidealised vault model. Additionally, staged analyses are conducted to provide an indication of how stability and seismic capacity evolve as the number of courses in the model increases.

In Chapter 6, the optimal geometric parameters derived from the previous Analysis Phase are used to model a dry-stone, Nubian-type vault composed of mechanically interlocking components. The performance of the vault geometry is assessed at several construction phases and compared to the results of Analysis Phase I. Afterwards, a final vault model is defined and is subjected to quasi-static pushover analyses with a maximum lateral acceleration equal to the PGA of a governing moonquake. Additionally, dynamic analyses of the final vault model are carried out to determine its natural modes of vibration and to assess its response to a ground motion time history.

In Chapter 7, material sensitivity studies are conducted for the final vault model to determine how material uncertainty may influence the overall structural performance.

The three main Analysis Phases carried out in this project build a basis for the structural design of a potentially viable Lunar vault. Several additional studies are carried out to explore possible variations in the configuration and loading of the vault. The first of these tasks consists of modelling and analysing a monolithic vault variant that is geometrically equivalent to the component-based vault, which is presented in Chapter 8. The results of this chapter serve to provide a basic illustration of how the performance of an additively manufactured vault compares to the component-based vault designed in this project. Chapter 9 provides a preliminary examination of how covering the vault in loose regolith may influence stability and seismic performance. Chapter 10 demonstrates how the vault, as designed for the Lunar context, may perform under the gravity loading present on Earth and on Mars.

Chapter 11 provides a summary of this report and a reflection on the degree to which the research objectives were fulfilled. Noteworthy findings are emphasised, with commentary on their novelty and scientific contribution. Finally, several compelling subjects for future research are identified.

Chapter 2

LITERATURE REVIEW

2.1 Overview

The literature reviewed for this project spans a range of subjects relevant to the design and analysis of an ET shielding structure, starting with an examination of the context behind existing design concepts in this field. Emphasis is placed on illuminating the research gap for masonry-based approaches in extraterrestrial design, particularly related to mortarless construction techniques. Seeking inspiration from terrestrial precedents, this work derives valuable insight from brick-based vernacular building techniques on how to adapt to extreme material scarcity through the use of local resources. Afterwards, the off-Earth hazards that confront humans and their supportive infrastructure are studied in detail. Focus is placed on defining hazards for the Moon because it is expected to present significant structural design challenges due to its particularly low gravity and high potential for seismic risk. After studying how to accurately define the expected environmental demands, literature is reviewed on the subject of structural assessment methods for dry-stone masonry. The final part of this section examines the properties of bulk regolith, as well as regolith-based structural materials.

2.2 Design context

2.2.1 Infrastructural requirements

Given the exorbitant costs of transporting material to the Lunar surface (Bell, 2011), it is evident that a sustained human presence on the Moon will only be feasible if missions efficiently utilise locally-sourced materials. Research by Sanders and Larson (2013) indicates that the incorporation of ISRU into mission architectures can reduce cost and risk of missions, which will increase the sustainability and affordability of off-Earth exploration. A key area of interest for developing ISRU frameworks for mission architecture relates to civil engineering and surface construction, such as radiation shields, landing pads, and habitats (Sanders & Larson, 2013). Fortunately, the fine dust that covers the Moon's surface can be processed in a number of ways to produce construction materials, which will be addressed in more detail in Chapter 2.5. Out of the main assets identified by Sanders and Larson (2013), this work focuses on structures that protect humans from radiation, extreme temperatures, and meteoroid impacts (Jablonski & Ogden, 2008).

2.2.2 State of ET habitat design

Many design concepts for ET habitats exist, with varying levels of development in terms of structural verification and fabrication methodologies. Commonly-proposed habitation systems centre around covering an inflatable or deployable module imported from Earth with a locally-fabricated shell in order to provide hazard

protection (Cesaretti et al., 2014; Konstantatou et al., 2022; Malla, 1991; Ruess et al., 2006; Spedding et al., 2020). Although the development of extraterrestrial infrastructure has not progressed significantly beyond architectural conceptualisation (Kalapodis et al., 2020), the field has potential to grow rapidly since space agencies have shown significant interest in advancing the maturity of various technologies related to ET construction. However, many of these advancements take place in the private sphere through public-private partnerships, which obscures access to information about the true state of extraterrestrial infrastructure development. Overall, structural design in this field appears to be lacking with respect to complex load cases deriving from impacts or ground motions. Notable exceptions include novel research by Kalapodis, Málaga-Chuquitaype, et al. (2022), Kalapodis, Zalachoris, et al. (2022), Kampas et al. (2021), and Málaga-Chuquitaype et al. (2022), which study the performance of monolithic regolith-based arches under micro-gravity and seismic loading. Most current research into ISRU-based fabrication focuses on the use of AM for extraterrestrial infrastructure, and often only considers static loading in its structural design. Additively-manufactured structures are presently receiving a significant amount of attention because of their ability to be robotically fabricated using local resources—demonstrated in a high-profile manner by the NASA Centennial Challenge (Mueller et al., 2019)—which is a crucial aspect of achieving sustained off-Earth human habitation (Ferrone et al., 2022; Gatto et al., 2014; Sanders & Larson, 2013). Although the possibility of producing structures using regolith-based 3D-printing has been demonstrated (typically in combination with imported binding materials), the structural performance of proposed concepts has not been assessed to a significant degree (Cesaretti et al., 2014; Khoshnevis & Zhang, 2012; Mueller et al., 2019). Other AM techniques are being developed which largely focus on continuous sintering of regolith, but these have only been used to create small samples of potential structural material and may be far from maturing to a state where large-scale structures are achievable (Imhof et al., 2017; Laot et al., 2021; Meurisse et al., 2017; Meurisse et al., 2018).

Continuous structures based on AM are not the only concepts under development for ET construction, however. Discretely-assembled structures offer a compelling alternative. Dry-stone, masonry-based construction techniques are considered particularly well-suited to the material and fabrication constraints found outside of Earth, but research towards applying these techniques in extraterrestrial environments is limited in comparison to AM. As shown in Figure 2.1, a mortarless discrete approach makes it possible to disassemble and reconfigure structures, which is not possible for continuous geometries fabricated through AM. This figure also illustrates how component-based approaches offer a more robust manufacturing approach, since they decouple structural element fabrication from on-site assembly. Mortar-based masonry approaches have been conceptualised (Khoshnevis & Zhang, 2012; Roberts et al., 2021; Warren et al., 2022), but the resulting structures would not be readily reconfigurable due to the permanent binding with mortar.

Out of the research that has been done on mortarless component-based ET design, focus has mostly been placed on the use of topologically interlocking components (Dyskin et al., 2005; Fateri et al., 2019; Imhof et al., 2017). According to Dyskin et al. (2005), topological interlocking occurs in an assembly of components

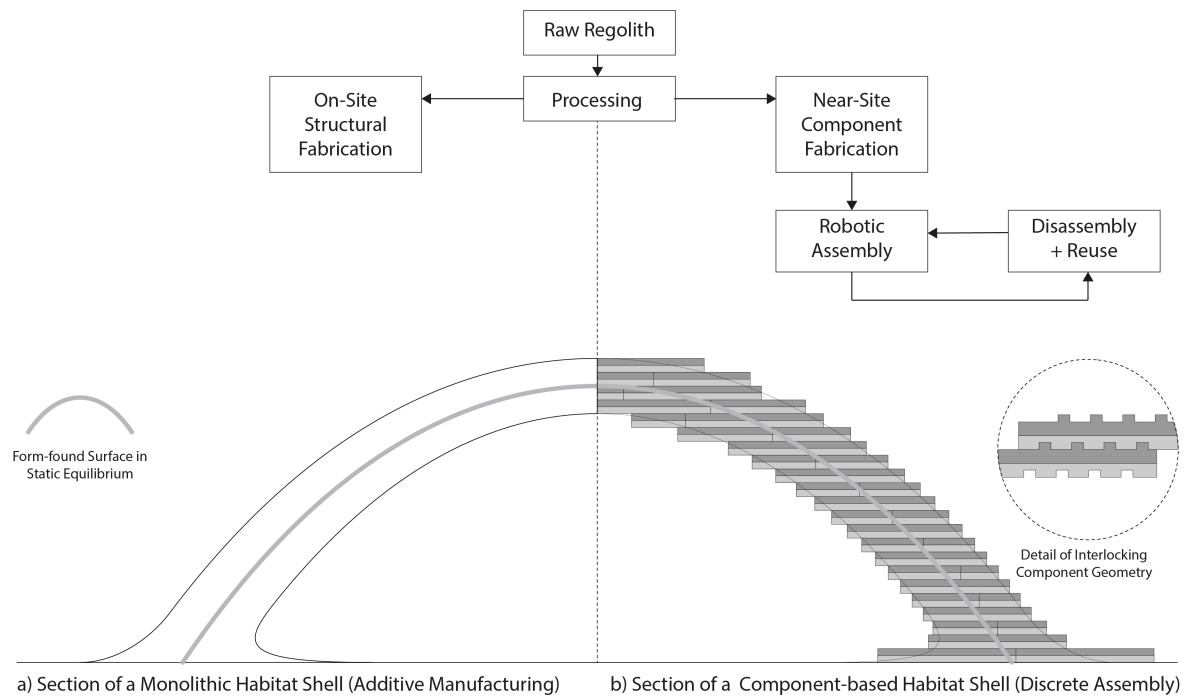


Figure 2.1: Comparison between AM and discrete assembly of vaulted structure (Konstantatou et al., 2021)

when each unit is held in place by kinematic constraints imposed by neighbouring components. The first example of this type of interlocking in history is identified by Dyskin et al. (2005) to be a planar assembly of tetrahedral components, which is shown in Figure 2.2 in order to provide a simple illustration of the concept of topological interlocking. On Earth, remarkable structures have been designed and constructed using topologically interlocking masonry based on principles of thrust network analysis developed by Block and Ochsendorf (2007). These methods can conceivably be applied to the structural design of extraterrestrial structures, but the geometric complexity and variability of resulting components may make such an approach undesirable in terms of manufacturing constraints.

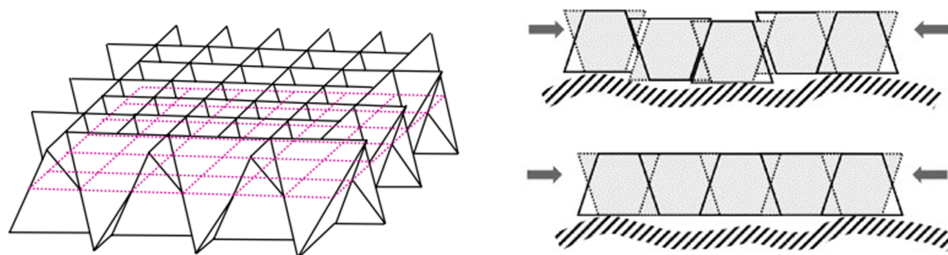


Figure 2.2: Illustration of planar topological interlocking (Dyskin et al., 2005)

Novel research investigates the design of structures based instead on mechanically interlocking components, as illustrated in Figure 2.3 (Konstantatou et al., 2021; Konstantatou et al., 2022). It is advantageous to design 3D structures with such components as opposed to ones connected through topological interlocking because the same building element can be used repeatedly to create various structures, while topological

interlocking typically requires a more constrained design approach where the global structure must first be defined and the shape and location of components follows from its tessellation. Konstantatou et al. (2022) propose several mechanically interlocking component-based infrastructure geometries derived with form-finding methods, but their structural performance has not been investigated. Literature is generally limited with regard to the nonlinear stability analysis of complex interlocking component-based assemblies, but this is particularly true for mechanically interlocking components. Zhou et al. (2020) propose the design of a vault constructed from mechanically interlocking bricks, but their analysis uses a continuum modelling approach that does not effectively capture the possible influence of inter-block movements. Similar limitations are present in research by Yazici (2018), where a shell composed of repeating mechanically interlocking panels is modelled geometrically, but the continuum-based, linear-elastic structural analysis carried out for the geometry does not verify that components interlock in a way that guarantees stability. The research gap with respect to mechanical interlocking assemblies is exaggerated in ET contexts, where microgravity introduces novel uncertainties that do not have a strong precedent.

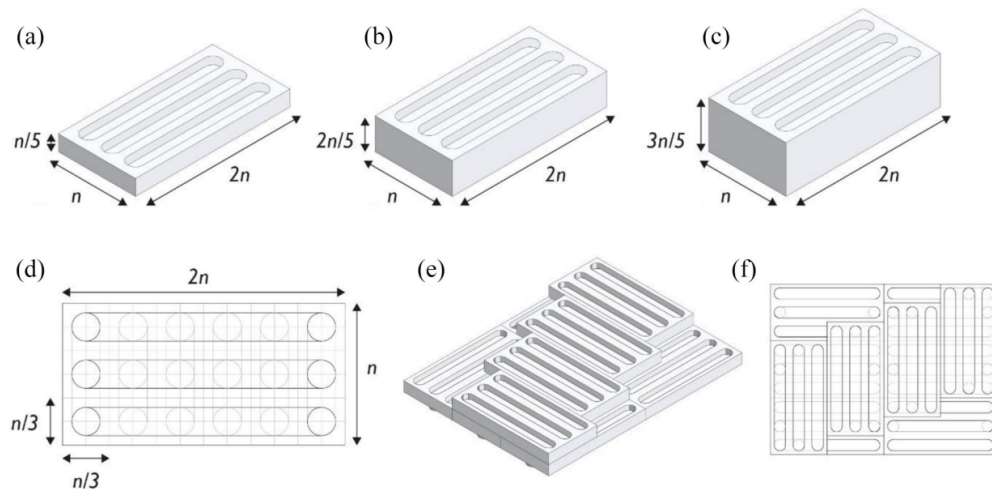


Figure 2.3: Possible configurations of proposed component geometry (Konstantatou et al., 2022)

Of the various structural concepts for shielding structures or habitat shells that exist, few investigate the effects of non-static actions such as seismic or impact loads. Most concepts reviewed were only analysed for gravity and internal pressure using linear methods. Research by Mottaghi and Benaroya (2015) conducts basic dynamic analysis of a 3D vault, but overall, existing literature does not comprehensively address the performance of structures exposed to ground motions in combination with microgravity. Some notable research investigates the performance of monolithic arches under static and dynamic seismic loading in extraterrestrial gravity (Kalapodis, Málaga-Chuquitaype, et al., 2022; Kalapodis, Zalachoris, et al., 2022; Kampas et al., 2021; Málaga-Chuquitaype et al., 2022), but seismic analysis of 3D geometries is lacking in literature. Lunar seismic events, specifically shallow moonquakes, have been identified as a potential risk to future Moon bases, so the need for comprehensive seismic analysis cannot be overlooked (Oberst & Nakamura, 1992). There is still significant progress to be made in the nonlinear seismic and stability analysis of extraterrestrial structures, especially for 3-dimensional geometries such as vaults.

There are numerous examples of masonry structures from vernacular architecture which may be worth considering for future explorations of ET design. Such structures provide an interesting perspective on how humans can effectively create settlements in extraterrestrial environments, since they arose in contexts defined by various forms of scarcity; early construction efforts were inherently based on efficient use of local resources, leading to impressive forms such as Nubian vaults, Trulli domes, and others (Duarte et al., 2021; Fathy, 1973; Todisco et al., 2017; Wendland, 2007). These examples can inform the design of off-Earth structures due to their compatibility with ISRU techniques, as well as their structural efficiency. Some relevant research has been conducted into the structural performance of dry-stone vernacular constructions, such as seismic analysis of "Trulli" structures by Venerito et al. (2017), or stability analysis of "Nuraghe" by Roberti and Spina (2001). These studies can be used to inform the numerical modelling methodology developed in this project, but there is still significant room for novel research. This is particularly true for contemporary adaptations of vernacular architecture, such as the vault geometry proposed by Konstantatou et al. (2022). The conceptual design of this geometry is shown in Figure 2.4, which is based on a type of structure known as a Nubian vault. Also called a pitched-brick vault, this type of structure is compared with a conventional barrel vault in Figure 2.5 to illustrate how the former does not require temporary formwork during construction.

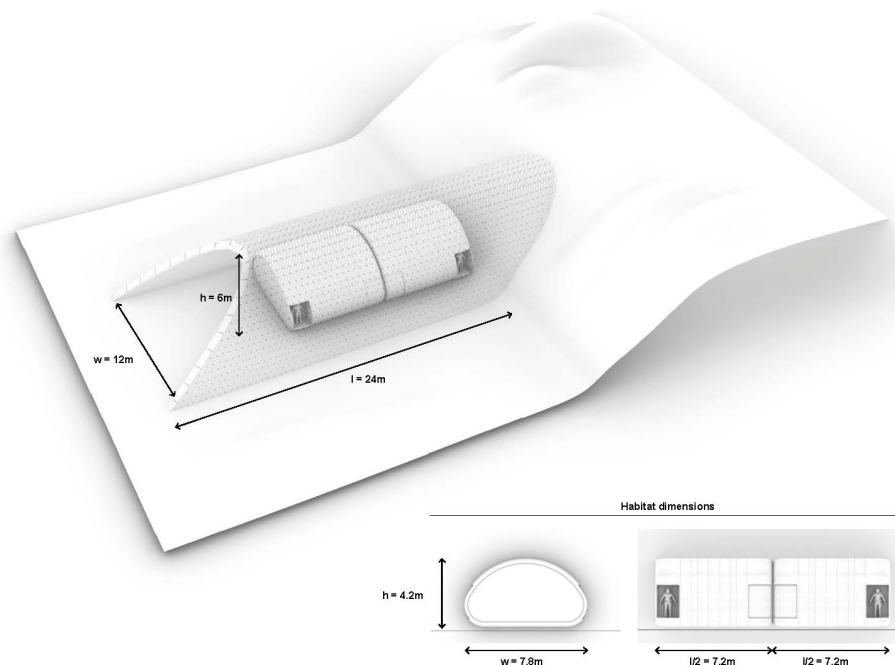


Figure 2.4: Proposed vault geometry informed by dimensions of a habitat module (Konstantatou et al., 2022)

The pitched-brick vault is an example of vernacular architecture originating from Northern Africa (Ochsendorf & Block, 2009), which is still being utilised in contemporary design. Its most notable feature is that it can be assembled without the use of formwork due to the use of inclined courses, in combination with a particularly cohesive mortar. The inclination reduces the destabilising component of self-weight, while the mortar holds bricks in place through adhesion. This allows for each new course to be stable during assembly, even though

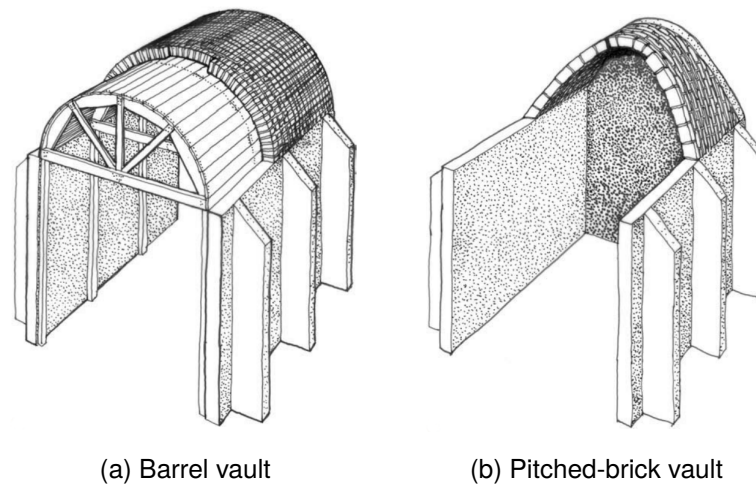


Figure 2.5: Comparison between vault types investigated by Ochsendorf and Block (2009)

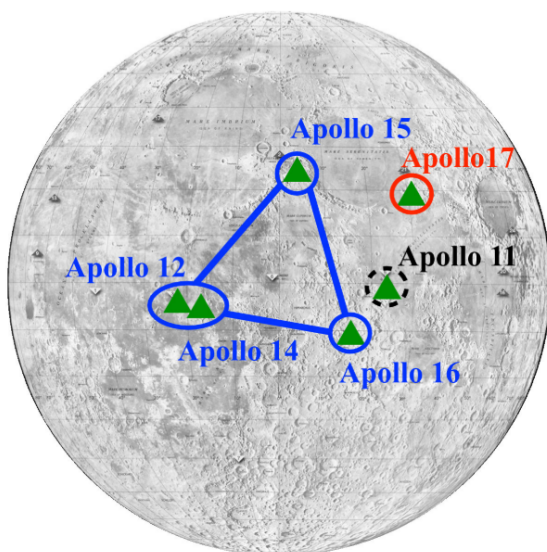
the course is not kinematically stable in the traditional sense discussed in Chapter 2.4.1. Scaffoldless construction is particularly appealing in the field of space manufacturing, so Konstantatou et al. (2022) proposes a mortarless adaptation of the Nubian vault which uses mechanical interlocking instead of mortar to maintain stability during assembly. This novel type of structure is classified in this thesis as a "Nubian-type" vault, and is interchangeably referred to as a pitched-brick vault. It is not clear to what degree the mechanical interlocking mechanism may influence structural behaviour of the dry-stone Nubian-type vault, which otherwise would be governed solely by friction at the interfaces between consecutive courses. Unless the interlocking tolerances are very small, this mechanism will not be engaged until frictional deformations are large enough to close gaps between a given pin and its corresponding groove. Given the loose-fit nature of the component-based approach proposed by Konstantatou et al. (2022), it is more appropriate to consider the interlocking mechanism as a tool for facilitating scaffoldless construction, which may have secondary effects in influencing the structural behaviour of the Nubian-type vault. These considerations will be investigated in this project.

2.3 Seismic hazard definition

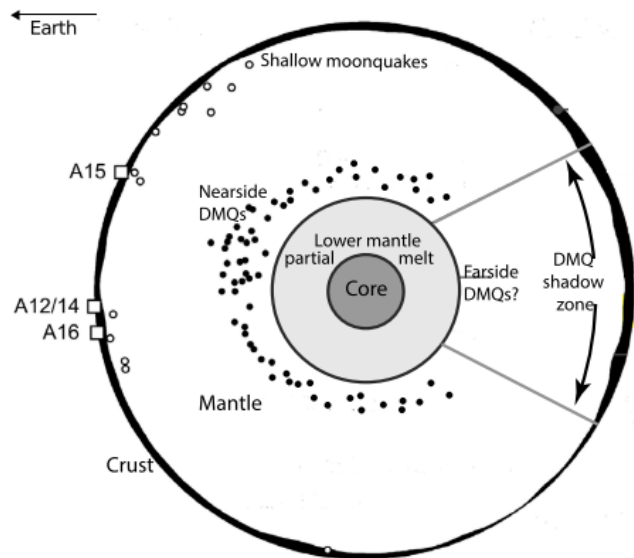
Conditions for off-Earth construction are harsh, with extraterrestrial environments presenting unique hazards to human life and infrastructure. The most significant hazards on the Moon include extreme temperatures, radiation, lack of atmospheric pressure, meteoroid impacts, microgravity, space dust, and seismic activity (Jablonski & Ogden, 2008). Hazards of a similar nature can be expected on Mars (Giardini et al., 2020; Karl et al., 2022). Of the main Lunar hazards, the combined influence of microgravity and seismicity has been identified to be crucial to early-stage structural design of the dry-stone masonry vaults studied in this project. Micrometeorite impacts are also of significant concern due to the large amount of energy carried by space debris (Allende et al., 2021), but such loading is not considered in this project due to the complex nature of impact modelling. As such, this section serves to gather the information necessary to define the expected structural demands that result from ground motions and microgravity.

2.3.1 Lunar seismology

A significant portion of what is known about Lunar seismology stems from data obtained from the Apollo Lunar Seismic Experiments Package (ALSEP). These experiments were conducted as part of the Apollo 11, 12, 14, 15, 16, and 17 missions, which ran from 1969-1977. No seismic observations have been performed on the Moon since transmissions from this program were terminated, but the wealth of data obtained from these experiments during their eight years of operation has been used extensively to study the interior structure of the Moon (Nunn et al., 2020). Research by Garcia et al. (2011), Lognonné et al. (2003), and Nakamura et al. (1982) and Garcia et al. (2019) has developed a fundamental understanding of the structure of the Moon, while providing important insight into the nature of Lunar seismicity. ALSEP led to the development of a basic seismic monitoring network, shown in Figure 2.6a, which allowed for determination of moonquake epi/hypocentres by comparing arrival times of the strong ground motion between different stations (Nakamura et al., 1979). This seismic network led to the identification of several sources of seismic activity: deep moonquakes, shallow moonquakes, and meteoroid impacts (Nakamura et al., 1982). Figure 2.6b shows the characteristic Lunar structure defined by Garcia et al. (2019), along with the location of deep and shallow moonquake sources.



(a) Nunn et al. (2020)



(b) Garcia et al. (2019)

Figure 2.6: Overview of a) Apollo seismic network and b) Lunar structure and moonquake sources

Deep moonquakes are low magnitude events that experience significant attenuation during their long travel path to the surface of the Moon, so they are not expected to pose a risk to Lunar infrastructure (Oberst & Nakamura, 1992). However, Oberst and Nakamura (1992) do identify shallow moonquakes as a source of risk. These events have a considerable magnitude and occur close to the Lunar surface, which means that they can cause significant ground motions. Research by Nakamura et al. (1982) compares the seismicity of the Moon to that of the Central United States, which experiences intra-crustal seismic activity. It is important to clarify that seismicity in this context refers to the rate of energy release, and does not necessarily provide

any clear indication of similarities in hazard definition; seismic hazard is highly dependent on source-to-site effects, as well as local soil conditions. The Apollo seismic data contained insufficient data to develop an understanding of the source-to-site effects, which are defined in earthquake design by Ground Motion Prediction Equations (GMPE), also known as attenuation laws (Ruiz et al., 2022).

The majority of research stemming from ALSEP focuses on defining global seismological mechanisms, with limited applicability to defining specific seismic hazards. This is largely because the short observation period prevents the development of meaningful probabilistic models. Furthermore, the quality of the raw moonquake data is relatively low due to the limited frequency response of the instruments, as well as degradation of the signal during transmission (Nunn et al., 2020). Lunar seismic data may be too limited to yield reliable hazards models, but several studies have used newer data obtained from NASA's Lunar Reconnaissance Orbiter (LRO) program to study moonquake hazards in more detail (Mohanty et al., 2020; Ruiz et al., 2022; Watters et al., 2019).

2.3.2 Seismic risk

To ensure structural safety, a statistical understanding of both demand and capacity is needed to define the risk of failure and to accordingly design a structure with a sufficiently low probability of failure. Actions that may damage a structure are called hazards, and the probability of these hazards leading to damage is defined as risk. Risk is a function of probabilistic variation in both the structural capacity and the applied loading. The capacity of a structure can be determined with a high degree of confidence through computational modelling and laboratory testing, while the precise definition of actions can present significant uncertainties, particularly for seismic design. The determination of statistical models which can be used to assess the probability of damage due to seismic events is called Probabilistic Seismic Hazard Analysis (PSHA). This type of analysis provides information about the likelihood of ground motion characteristics being exceeded during the service life of a structure. By conducting PSHA, site-specific Uniform Hazard Spectra (UHS) can be determined and used to define loading for performance-based seismic design.

In the case of Lunar seismic hazards, there is a large amount of uncertainty in defining a probabilistic model that reliably predicts how often events with a certain PGA may occur. As mentioned earlier, the Apollo data alone cannot be accurately used for a PSHA because it lacks the specificity to define source-to-site effects for shallow moonquakes affecting a particular site. Novel research stemming from LRO data, however, has provided the necessary GMPEs for use with a site near the location of the Apollo 17 landing. In combination with a catalogue of the 28 recorded shallow moonquake events, the newly-obtained GMPE has been used to define a set of preliminary response spectra for the seismic design of a Lunar structure. These spectra are shown in Figure 2.7.

In the absence of usable seismic design spectra for the Lunar South Pole, which is the most likely site for future human settlements—due to its nearly constant illumination and potential for water ice extraction (Cannon & Britt, 2021; Gatto et al., 2014)—the UHS developed by Ruiz et al. (2022) may be used to define preliminary moonquake loading for Lunar structural design. Although it is uncertain whether the assumed

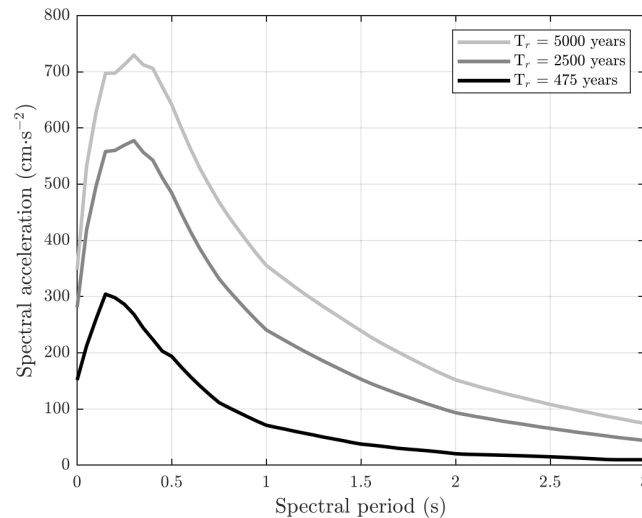


Figure 2.7: Uniform hazard spectra (Ruiz et al., 2022)

hazards are representative of a realistic design case, they are useful for developing a framework for analysis which can be readily updated once hazards can be accurately defined. Spectra corresponding to three return periods are represented in Figure 2.7, but it is unclear which is the most appropriate for the design of a Lunar vault. In their research, Kalapodis, Zalachoris, et al. (2022) reflect on the required performance of Lunar infrastructure in general, explaining that its high cost and importance should lead to a designation of high importance. How this qualitative observation may translate to quantification of reliability requirements is not clear, however. Official guidance on performance level definition for Lunar structures is lacking, so it is uncertain what recurrence period is appropriate to use for defining ultimate limit state (ULS) loading for Lunar structures. This uncertainty is associated with possible differences in service life and reliability requirements between Earth and off-Earth environments. In terrestrial design codes, the designated use of a structure informs its reliability requirements, such that structures which have a higher importance in protecting human life must resist higher, though less probable, loading. Without clear regulations defined by a governing body, an accurate basis for defining performance levels is not available and significant assumptions must be made regarding design-level loading. Still, terrestrial design standards may provide a reasonable background for informing preliminary design choices.

In seismic design, hazard is typically described in terms of a peak ground acceleration (PGA). Eurocode 8 (EN1998-1, 2004) recommends the reference value for PGA to be based on a 475-year return period for a given site, assuming Type A (rocky) soil. Depending on soil characteristics and the importance class of the structure, the PGA is scaled by a soil factor, S and an importance factor, γ_1 . By default, ordinary buildings are assigned an importance class of II, which corresponds to a γ_1 equal to 1.0 according to Chapter 4.2.5 of EN1998-1 (2004). For important structures, a γ_1 value larger than 1.0 is used to account for a greater degree of reliability, which reflects the choice of longer return periods. Although Kalapodis, Zalachoris, et al. (2022) suggest that a high importance class is warranted for ET infrastructure, there is a significant amount of uncertainty associated with how reliability requirements will be defined for habitat shields or

other unique structures that have limited precedent in terrestrial design. One factor to consider is that the vaults studied in this project can be used to protect human habitats or mission assets, both of which may result in different reliability requirements. Another important consideration is that shielding structures will likely need to be treated as sacrificial elements with respect to providing space debris impact protection (Benaroya & Ettouney, 1992; Buslov et al., 2019; Gunasekara & Jablonski, 2021; Steiner & Malla, 2022). According to Gunasekara and Jablonski (2021), a habitat shield should be easily repairable using in-situ resources. Impact considerations further complicate reliability considerations, but they are expected to lead to shorter service life definition and more regular repair than standard terrestrial structures. Given the various uncertainties associated with Lunar structural design, this project assumes that a return period of 475 years can be used for preliminary seismic analysis.

2.3.3 Application of moonquake loading

Seismic loading can be applied quasi-statically, in the form of a pushover test, or dynamically, in the form of a time-history analysis. In many cases, quasi-static analysis is sufficiently accurate to study a structure's seismic capacity. Such analysis is significantly more computationally efficient than fully dynamic analysis, though it may be overly conservative. For quasi-static analysis, the effect of ground motions can be applied as an equivalent lateral load in an incremental manner until failure occurs (Gonen et al., 2021; Kalapodis, Málaga-Chuquitaype, et al., 2022; Kalapodis, Zalachoris, et al., 2022; Lemos, 2019; Michiels & Adriaenssens, 2018).

Dynamic analysis is more realistic and can simulate complex structural responses, but it requires more computational investment. To conduct fully dynamic analyses, a time history of ground motion data is necessary. According to Elnashai and Di Sarno (2008), there are three main approaches in the field of seismic engineering for obtaining ground motion time histories. These include utilising natural records, generating a random signal that fits a target spectrum, or using complex mathematical formulations based on geophysics and wave propagation modelling. In the limited field of Lunar seismic design, most studies use an approach consistent with the second method, in combination with theoretical or empirical attenuation models (Mottaghi & Benaroya, 2015, Cadena et al., 2020). Mottaghi & Benaroya (2015) utilise a theoretical energy diffusion model to determine the power spectral density of a moonquake with a given magnitude and distance, which is used to generate a time history from a white noise signal. If a design hazard spectrum is available, SIMQKE can be used to simulate statistically independent accelerograms, which is consistent with the second approach described above.

Aside from generating synthetic seismograms or directly using the original seismograms, there is precedent in using earthquake time histories to approximately represent Lunar ground motions, despite significant differences in rise time, duration, and frequency content in the signal which arise due to the differences between the Lunar interior structure and that of Earth. Málaga-Chuquitaype et al. (2022) utilise several time histories of earthquakes from Central and Eastern North America for a seismic analysis of a Lunar structure. This is motivated by the research from Oberst and Nakamura (1992) which claims that the chance of a

randomly chosen site to experience a shallow moonquake with a body wave magnitude of greater than 4.5 within 100 km is approximately one in four hundred years, an occurrence rate similar to that of intraplate earthquakes in Central United States. Based on this, Málaga-Chuquitaype et al. (2022) chose events that had a magnitude greater than 5.5, epicentral distances of less than 90 km, and were recorded on sites with V_{s30} values of between 396 and 1700 m/s. These shear wave velocities are not consistent with literature on Lunar soil properties in the upper parts of the crust, however. According to Kovach & Watkins (1973), the P-wave velocity at a depth from 8.5 m to somewhere between 25.5 and 62.5 meters is approximately 300 m/s, with an S-wave velocity calculated as $0.61V_p = 183$ m/s. This value is less than half of the lowest S-wave velocity from the stations chosen by Málaga-Chuquitaype et al. (2022), with most V_{s30} values being significantly higher. The overall approach may provide viable time histories that may more confidently approximate Lunar ground motions if different events were chosen with V_{s30} values closer to 183 m/s.

2.4 Structural analysis of dry-stone masonry

2.4.1 Analytical methods

Given the negligible tensile strength of stone and cementitious materials, masonry structures must be designed to resist loads only through compression. In most cases, compressive working stresses in these structures are expected to be low with respect to the strength of the material, so their design is often governed by stability (Heyman, 1966). Structural mechanical formulations of arch stability under vertical loading were first published in the 18th and 19th centuries, most notably by Coulomb (1773) and De La Hire (1712), whose work was then revisited and expanded upon by Jacques Heyman in the 1960's (Michiels & Adriaenssens, 2018). Heyman's "safe theorem" has been highly influential in studies of masonry stability. This theorem is based on an equilibrium method known as thrust line analysis and states that an arch will be stable if a compression load path exists within the bounds of the structure (Heyman, 1966; Michiels & Adriaenssens, 2018). This path is what is referred to as a thrust line. In more recent years, analytical formulations for studying the stability of masonry arches under horizontal loading have been developed (McLean et al., 2021; Michiels & Adriaenssens, 2018; Oppenheim, 1992). These approaches approximate seismic loading by applying an equivalent horizontal acceleration and can be used to determine the acceleration which leads to the onset of instability or find the minimum thickness for an arch to resist a given static loading. The concept of thickness optimisation has been addressed in research by Michiels and Adriaenssens (2018) and McLean et al. (2021), the latter of which led to the development of OpenArch, an open-source Matlab package for finding optimal arch forms under horizontal loading.

The concepts behind thrust line and limit state analysis have been expanded to the design and analysis of vaults (Gaetani et al., 2017; Michiels et al., 2019) in the form of thrust network analysis (Block & Ochsendorf, 2007), but this research has limited applicability to the novel type of vault studied in this project. Heyman writes about analysing vault stability by conducting thrust line analysis on its vertical cross-sections; if all of the "slices" are stable, then the original structure must be stable (Heyman, 1966). A similar approach is demonstrated with the addition of horizontal loading in Michiels et al. (2019), where a global vault geometry

is constructed. These approaches are based on the assumption that the vault can be treated as a homogeneous shell, where there is no sliding between components. The absence of sliding is one of Heyman's three key assumptions in defining thrust line analysis (Heyman, 1966). In many cases of masonry design, this is a reasonable assumption due to the presence of mortar. Although mortar provides negligible tensile strength, it does have significant capacity to prevent sliding between components. Due to the inclination of the Nubian-type dry stone vault, consecutive courses are primarily coupled through frictional forces, which vary along the length of the vault and may not be large enough to prevent sliding. In 3D mortarless masonry structures, the no-sliding assumption can be satisfied through topological interlocking. In cases of simpler dry-stone structures such as walls, arches, or corbelled domes, large frictional forces can be expected to prevent sliding. Since it is unclear whether the assumptions of thrust line analysis are satisfied for the vault considered in this project, numerical modelling will be necessary to study its structural behaviour.

2.4.2 Numerical methods

Due to the novelty and complex structural behaviour of dry-stone Nubian-type vaults, a numerical approach is needed. The distinct element method, also called the discrete element method (DEM) is chosen because of its ability to accurately and efficiently simulate the behaviour of systems characterised by nonlinear failure modes such as joint sliding or separation between elements (Lemos, 2007). It is possible to account for some degree of joint discontinuity using interface elements in FEM software, but the definition of these elements can be challenging and the degree of deformation is typically limited (Roberti & Spina, 2001). Accounting for joint sliding and separation is particularly important for dry-stone masonry, where the absence of mortar often makes it unreasonable to model structures in a continuum-based manner that is consistent with the finite element method. A discontinuum modelling approach is therefore more appropriate for these structures. DEM readily accounts for this type of non-linearity through automatic redefinition of contacts (Lemos, 2007). A software package commonly used for distinct element method analysis for masonry structures is known as 3DEC (Itasca Consulting Group Inc., 2019).

In 3DEC, as in other DEM software, masonry units are modelled as blocks, which can be rigid or deformable, with joint properties represented by zero-thickness interfaces (Gonen et al., 2021). When using rigid blocks, deformations are concentrated in the joints, while deformable blocks are represented by finite element meshes that can deform internally as well. The use of rigid blocks is common for modelling many masonry structures, and is particularly appropriate for problems where inter-block movements are dominant (Gonen et al., 2021; Lemos, 2019). Introducing block deformability is useful when weak materials are used or when stress concentrations are expected, but deformable block models are more computationally expensive and are not commonly used for dynamic analysis (Lemos, 2007, 2019).

In the distinct element method, interaction between blocks is defined through sets of point contacts which are periodically updated as connectivity between blocks changes during loading (Lemos, 2019). 3DEC employs a soft-contact approach, where these point contacts can overlap slightly and are treated as a system of springs with stiffness in the shear and normal directions, as depicted in Figure 2.8. In rigid block models,

the deformation of these contacts at the interfaces between blocks can approximate the deformability of the blocks themselves. This is accomplished by dividing the elastic modulus of the material by the centroidal distance between blocks which share the interface (Gonen et al., 2021). Continuum-based modelling can be incorporated into DEM modelling through the use of deformable blocks. This approach results in blocks being internally discretised into finite element meshes, but still allows for the simulation of highly nonlinear behaviour at block interfaces (Lemos, 2019).

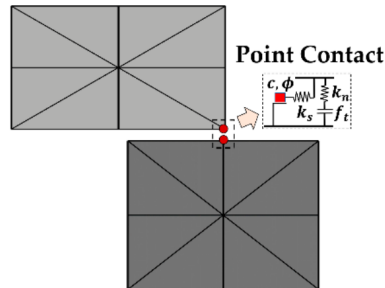


Figure 2.8: Point contact representation (Gonen et al., 2021)

All analyses in 3DEC, both static and dynamic, are based on a dynamic, time-domain algorithm that explicitly solves the equations of motion of a system of blocks through the finite difference method (Itasca Consulting Group Inc., 2019). The basic structure of this algorithm is presented in Figure 2.9. Static problems are solved using a type of damping termed *local damping*, which approximates a static response. A static analysis is assumed to reach equilibrium when the velocity of all blocks in the model converges toward zero (Lemos, 2007). For dynamic analysis, 3DEC allows for the use of Rayleigh or Maxwell damping. Rayleigh damping is commonly used for the analysis of masonry structures (Lemos, 2019). Parameters for Rayleigh damping depend on the characteristics of a given model, since this type of damping is frequency dependent. According to Itasca Consulting Group Inc. (2019) the governing timestep will be reduced as the stiffness component of damping is increased, so the inclusion of damping can worsen the computational bottleneck that occurs for models with small or stiff components.

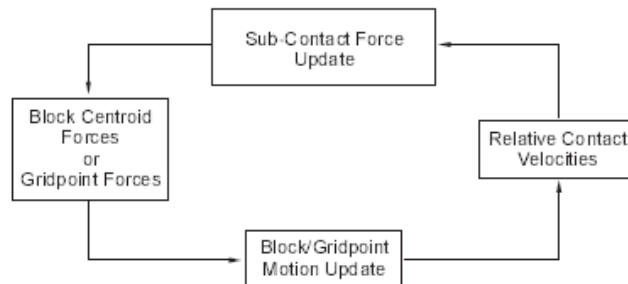


Figure 2.9: 3DEC calculation cycle (Itasca Consulting Group Inc., 2019)

The solution scheme implemented in 3DEC is conditionally stable, meaning that the timestep resulting in a stable solution will vary based on model characteristics. A stable timestep is proportional to the ratio of

mass divided by stiffness. This can create a significant computational bottleneck for models with very small or highly stiff components.

2.5 Material definition

In order to assign appropriate constitutive models, it is necessary to understand the expected mechanical properties of the bricks used in this project. As explained in Chapter 2.2.1, there is significant value in maximising the proportion of locally-derived materials in any type of off-Earth construction. Therefore, emphasis is placed on structural materials derived entirely from Lunar resources, namely regolith, which has demonstrated significant potential for use as construction feedstock.

This section first examines the properties of raw regolith, which were determined from experiments on real Lunar samples obtained during the Apollo era. This information is used in the modelling and analysis of regolith overburden in Chapter 9, but also provides important context to how it can be processed to create structural materials. Based on research into the properties of Lunar soil, simulants have been designed which mimic its key properties and composition. The creation of such simulants was necessary due to the scarcity of real regolith samples. Using various types of regolith simulants, a wide range of research has been carried out into the possibility of manufacturing structural elements using regolith.

2.5.1 Unprocessed regolith properties

The mechanical properties of Lunar soil are known based on data collected during various unmanned and manned missions to the Moon in the late 1960s and early 1970s (Heiken et al., 1992). Regolith is fairly uniform in terms of its composition, so relative density controls most of its physical properties (Heiken et al., 1992). Table 2.5.1 indicates how relative density varies with depth below the Lunar surface.

Depth range (m)	Relative density (%)	Description
0.00-0.15	65 ± 3	Medium to dense
0.00-0.30	74 ± 3	Dense
0.30-0.60	92 ± 3	Very dense

Table 2.1: Variation of relative density for Lunar regolith - adapted from Heiken et al. (1992)

According to Dewoolkar et al. (2018), elastic modulus values were not obtained for Lunar regolith, which is crucial in defining its mechanical behaviour. Shear stiffness values could not be found in literature either. Comprehensive testing has been done, however, using various regolith simulants which approximate the behaviour of Lunar soil. GRC-3 simulant was analysed by Dewoolkar et al. (2018), yielding key mechanical properties summarised in Table 2.2. The minimum bulk density was shown to be 1.52 kg m^{-3} . Mechanical properties were obtained for several relative densities, but the results for a value of 42% are highlighted here. Although this relative density is significantly lower than those shown in Table 2.5.1, it is not clear what the relative density of the regolith will be after excavation from the surface. Therefore, results for a lower relative density are expected to provide a conservative estimation of mechanical properties for loose

regolith. Cohesion was found to be 3.1 MPa and the friction angle was 41.8°. Under a confining stress of 25 kPa, the elastic modulus for this sample was determined to be 18.9 MPa, along with a Poisson's ratio of 0.42. These properties are needed for definition of Mohr-coulomb deformable block models in 3DEC.

Density (kg m^{-3})	E (MPa)	ν	c (MPa)	ψ (deg)	ϕ (deg)
1.52E+03	1.89E+01	0.42	3.10E-03	8.6	41.8

Table 2.2: Mechanical properties of GRC-3 Lunar regolith simulant (Dewoolkar et al., 2018)

Research by Akisheva and Gourinat (2021) seeks to find the degree of shielding that ensures a radiation dose of under 150 mSv per 180 days. This limit is informed by dose limits set by NASA. In order to achieve this level of radiation protection, regolith with an areal density of at least 1600 kg m^{-2} is needed (Akisheva & Gourinat, 2021). In terms of volumetric density, this translates to a minimum of 1.0 m of bulk regolith at a density of 1600 kg m^{-3} . Such shielding dimensions are expected to fulfil thermal and micrometeorite protection requirements based on research by Spedding et al. (2020), which determined that an areal shielding density of 1450 kg m^{-2} is needed to protect against these additional hazards.

2.5.2 Regolith-based manufacturing techniques

This section provides an overview of potentially viable techniques for manufacturing regolith-based structural materials. An extensive array of manufacturing techniques have been proposed for extraterrestrial construction, which can be roughly grouped into continuous and discrete manufacturing techniques; continuous techniques are classified as those which bond regolith in a layer-by-layer fashion, while discrete techniques produce objects where the regolith is uniformly bonded together. Both of these categories have shown promising results for producing regolith-based structural materials. Focus is placed on methods which directly utilise regolith in the absence of any foreign binding material, due to considerations mentioned in Chapter 2. Therefore, out of the different potential approaches for utilising regolith as a construction material, those based on binding dry regolith particles are primarily considered.

2.5.2.1 Continuous manufacturing techniques

A number of studies have researched continuous regolith-based manufacturing techniques in the Lunar and Martian context. These are often envisioned as being used to 3D print a global geometry on-site. The main continuous, or additive, manufacturing approaches considered for extraterrestrial applications are defined by concepts such as material extrusion, vat photopolymerisation, powder bed fusion, direct energy deposition, binder jetting, material jetting, and sheet lamination (Karl et al., 2022). Among these, the techniques that do not require any binders or foreign additives are powder bed fusion (PBF) and directed energy deposition (DED). As shown in Figure 2.10, PBF uses concentrated thermal energy to fuse particles in a powder bed. There is a significant amount of research into regolith processing with PBF, so this process is further examined in the literature review to determine appropriate properties for the equivalent monolithic

vault studied in Chapter 8. However, these approaches could also be used to additively manufacture brick-like units rather than directly fabricating a structure. Samples obtained through selective laser sintering by Goulas et al. (2019) had a density $2.3\text{E}+03 \text{ kg m}^{-3}$, an elastic modulus up to 287.3 MPa, and a compressive strength of up to 4.2 MPa.

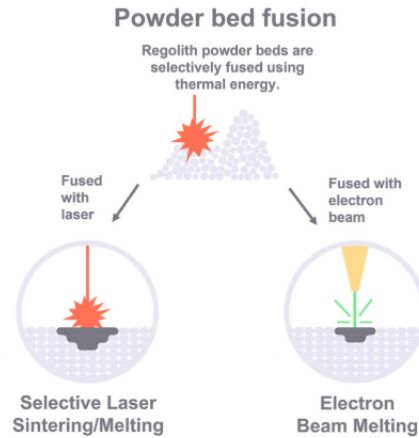


Figure 2.10: Illustration of PBF-related manufacturing processes (Karl et al., 2022)

Tensile testing of SLS regolith material has not been carried out, but Kalapodis, Málaga-Chuquitaype, et al. (2022) have estimated its tensile strength to be equal to one-tenth of the compressive strength based on the strength properties of other cementitious and ceramic materials. Along this same logic, Kalapodis, Zalachoris, et al. (2022) assume that the cracking behaviour of SLS regolith materials can be approximated using a bilinear traction-separation law based on typical material parameters of ceramic materials. The researchers define their nonlinear constitutive model based on a Mode I fracture energy derived from a conservative fracture toughness value for ceramic materials. The researchers assume a value for K_{Ic} equal to $0.5 \text{ MPa m}^{0.5}$, which they obtained from work by Ashby (1999). From this value, fracture energy, Γ , is calculated to be $8.35\text{E}-07 \text{ N mm}^{-1}$. Given the novelty of this type of material, it is difficult to validate if the assumed tension softening model is accurate, but it can be a useful approximation for preliminary analysis.

It is important to note that despite these approaches being apparently aligned with a 3D-printed approach to extraterrestrial manufacturing, they have not been demonstrated to work on a large scale and may present significant challenges in their application to printing entire habitats (Fateri et al., 2019). To date, the only AM-based approaches that have been demonstrated clear potential for printing large scale objects such as habitats are those based on material extrusion (Cesaretti et al., 2014; Khoshnevis & Zhang, 2012; Mueller et al., 2017). These approaches require imported binding materials, which is a significant downside.

2.5.2.2 Discrete manufacturing techniques

In contrast to an AM approach, products made using discrete manufacturing take shape in distinct steps, ultimately reaching a final state where the regolith is uniformly bonded together. There are seven main categories of bonding regolith according to Karl et al. (2022): sintering, melting, powder pressing, powder

agglomeration, aggregate bonding, chemical fusion, and freezing. Each of these shows promise in the fabrication of structural elements, although aggregate bonding, chemical fusion, and freezing require additional material aside from regolith and are thus not considered at this stage of the project.

The potential for applying conventional sintering techniques to produce structural bricks from regolith has been understood for decades (Steurer, 1982), and significant research has been conducted on this subject over time. Conventional sintering involves compacting and bonding fine particles in a furnace at a temperature below their melting point (Cooper, 2008). This process is illustrated in Figure 2.11. Temperatures above a material's melting point can be used in alternative manufacturing techniques based instead on melting and casting crystalline materials. Melting and casting result in materials classified as glass, glass-ceramics, or cast products (Farries et al., 2021). The principles behind the approaches classified by Farries et al. (2021) as sintered or melted regolith (SoMR) have been used extensively in ceramics and glass manufacturing on Earth. In principle, they could readily be applied in the Lunar context, provided that the required energy and mechanical infrastructure can be implemented there. In conventional sintering methods, heat can be applied using resistive radiant heating or microwave radiation. A significant number of studies have investigated the feasibility of applying this technique to manufacturing regolith-based structural materials, particularly bricks or similar components. Many of these studies have produced material samples with properties that meet or exceed the performance of traditional masonry and concrete materials. Studies by Hoshino et al. (2016), Indyk and Benaroya (2017), and Meurisse et al. (2017) utilise resistive radiant heating to produce regolith-based materials with favourable mechanical properties. Table 2.3 presents key mechanical properties obtained by Indyk and Benaroya (2017) which will be used to define constitutive models for 3DEC analysis in Chapter 4.

ρ (kg m ⁻³)	E (MPa)	G (MPa)	ϕ (deg)
2.60E+03	8.36E+03	3.30E+03	40

Table 2.3: Mechanical properties of sintered regolith (Indyk & Benaroya, 2017)

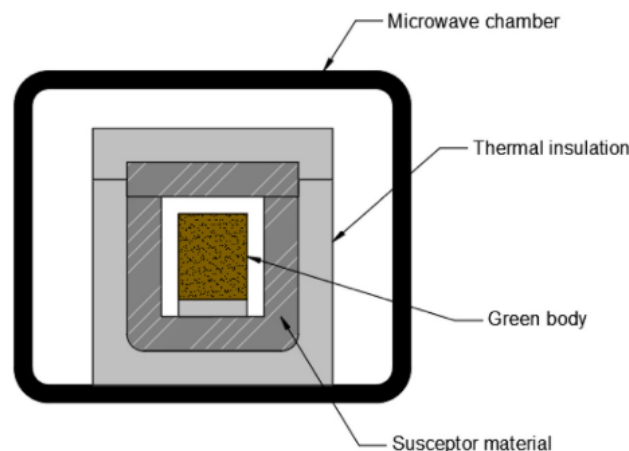


Figure 2.11: Illustration of microwave sintering apparatus Farries et al. (2021)

MODELLING FRAMEWORK

3.1 Overview

In this section, a framework for generating geometric and numerical models of pitched-brick vaults is presented. First, a methodology for geometric modelling in Rhino is described, followed by methods for converting the Rhino geometry into distinct element models for use in 3DEC. The geometric modelling approach is based on the conceptual methodology developed by Konstantatou et al. (2022), which can be applied to structures with varying complexity. Emphasis was placed on modelling vault structures due to their clear utility as potential habitat shields and their elevated degree of complexity. As explained in Chapter 2, pitched-brick vaults offer distinct advantages over other masonry vaults and are therefore used as the basis for choosing a geometric definition in this project.

A visual representation of the tools used for this project is shown in Figure 3.1. Modelling takes place in the Rhino environment, where Grasshopper is used to create a parametric definition of the vault. This geometric data is used as an input into a series of Kangaroo2 simulations, which reconfigure the model to simultaneously satisfy several constraints. Once the geometric constraint solving process produces a compliant model, it must be exported to 3DEC for analysis. A Python script was written to assemble the geometric data in a way that is compatible with requirements in 3DEC.

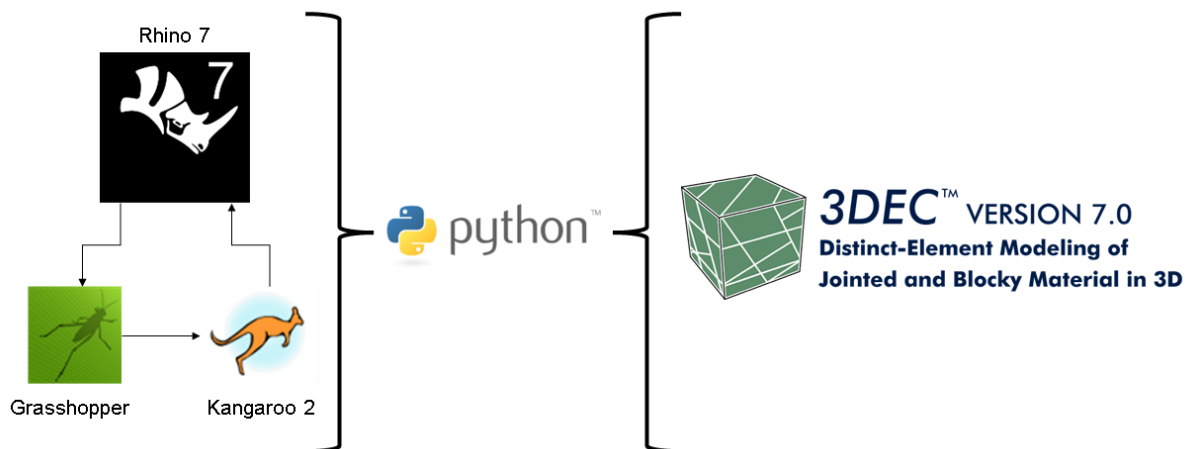


Figure 3.1: Modelling tools

3.2 Geometric definitions

Relating to the left side of Figure 3.1, this section describes the generation of geometric data using explicit Grasshopper definitions, which are later modified using geometric constraint solving to make them physically viable.

3.2.1 Component geometry

The initial definition of component geometry was based on research by Konstantatou et al. (2022), which proposes a 3-groove component with an in-plane aspect ratio of 2:1, as shown in Figure 2.3. Accordingly, preliminary analyses assumed in-plane dimensions of 0.5 m x 0.25 m, with a height of 0.1 m, which corresponds to Figure 2.3b. Such a component is not directly compatible with 3DEC because the software can only import convex solids. As a result, the unit was idealised and divided into several constituent components, which individually conform to the topological requirements of 3DEC. Figure 3.2 illustrates how the component is initially subdivided and subsequently joined into one rigid block. The component geometry is defined by a parametric model where the dimensions of all parts of the block can be varied, as well as the number of grooves. Several permutations of the component geometry are pictured in Figure 3.3. The variation of geometric parameters for the unit is studied in Analysis Phase I, but the fundamental approach to modelling each component as a group of individual elements does not change—for every component geometry used in this project, the component is broken down into a base, two end blocks, a series of groove walls, and two pins, as shown in Figure 3.2. It is important to note that throughout all the analyses, the component height was assumed to be 0.1 m in order to reduce parametric variation. Compared to Figure 2.3, which shows the conceptual component geometry, the idealised version removes the rounded ends of each groove and replaces the conical pins with polygonal prisms in order to avoid concavity. The Grasshopper script developed for modelling the components allows for variation of the shape, dimensions, and location of these pins. Hexagonal prisms were chosen because they are believed to sufficiently approximate the original while maintaining a minimum edge length that is not excessively small. The use of elements with very small edge lengths can introduce issues with tolerances and increases the number of contact points, which increases computational demand. Once the desired parameters are defined, the group of subcomponents can be imported into 3DEC and joined together to form a rigidly linked collection of blocks that approximates the desired unit component geometry. For any given global geometry composed of these components, a script is used to iteratively assemble each group of elements into a single rigid brick.

3.2.2 Global geometry

For a given component geometry defined according to Chapter 3.2.1, an initial model is created which approximates how a collection of these units can be assembled into a Nubian-type vault. This initial configuration of components serves as an input for geometric constraint solving, where mechanical interlocking and other constraints will be imposed.

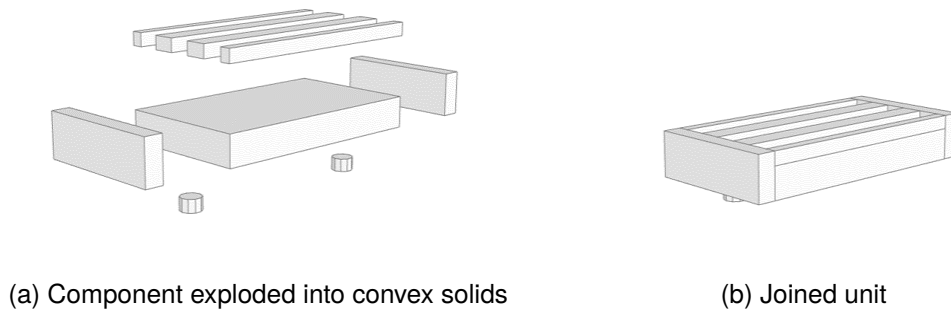


Figure 3.2: Illustration of 3DEC-compatible component

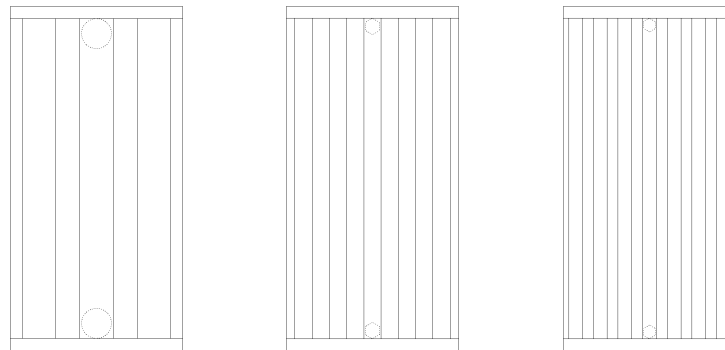


Figure 3.3: Parametric variation of component geometry

In this project, the choice of global geometric parameters such as rise and span of the vault are informed by Konstantatou et al. (2022), which proposes shielding structure dimensions that can accommodate an existing habitat module design concept. As such, the span of the vault was chosen to be 12 m, with a rise of 6 m and a length of 24 m, referring to the geometry in Figure 2.4. The influence of inclination and component dimensions are not well understood due to the novelty of this type of structure, so these variables will be the focus of parametric studies in Analysis Phase I.

As shown in Figure 3.4, a thrust surface is first defined, which is accomplished by extruding a catenary curve that satisfies the desired rise and span of the vault. Other curves can be used, but a catenary was expected to most efficiently resist self-weight and seismic loading based on research by Málaga-Chuquitaype et al. (2022). This surface is then intersected with a series of inclined planes, each of which represents the base plane of one course of components. The curves resulting from the surface-plane intersection are then tessellated according to the desired component geometry. The initial tessellation represents a component assembly that is ideally fitted to the course paths, and thus is intersected by the global thrust surface. In theory, this should ensure that the structure experiences only compressive forces. Additionally, the tessellation is accomplished in such a way as to minimise overlap between neighbouring components and to ensure that joints of consecutive courses are staggered, as illustrated in Figure 3.5. As shown in this figure, the blocks are arranged in such a way as to recreate the fundamental shape of the vault, but do not yet satisfy mechanical interlocking requirements. At this stage, the model definition can be input into a geometric constraint solving algorithm to find an arrangement of the components that allows for mechanical interlocking to take

place. The steps shown in Figure 3.4 are fully parameterised, so any combination of geometric parameters can be used to generate an initial model.

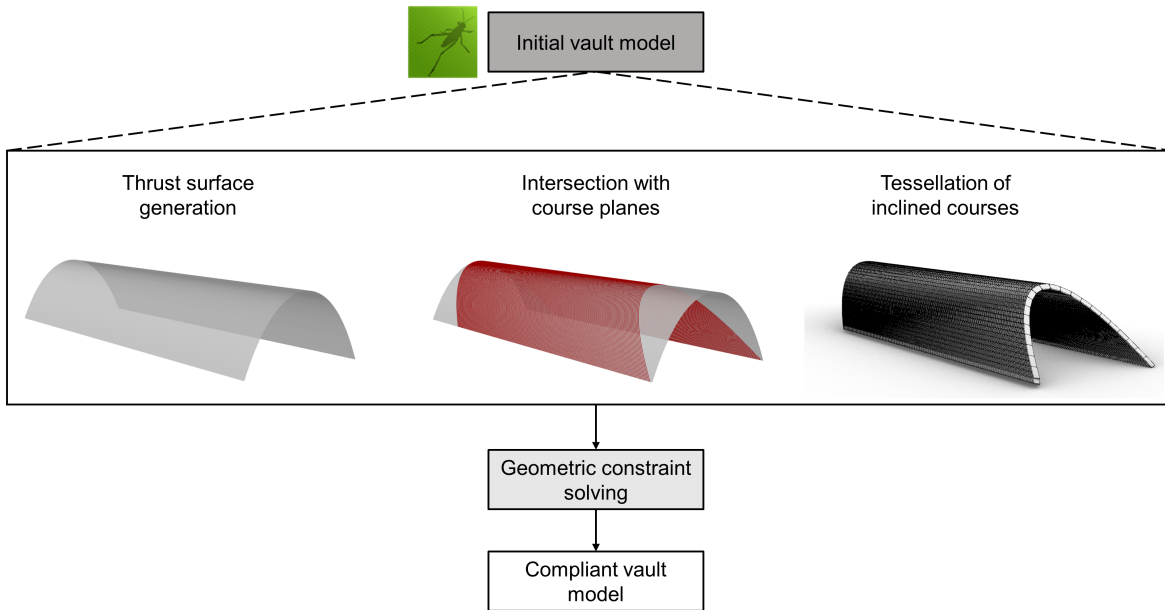


Figure 3.4: Generation of input geometry

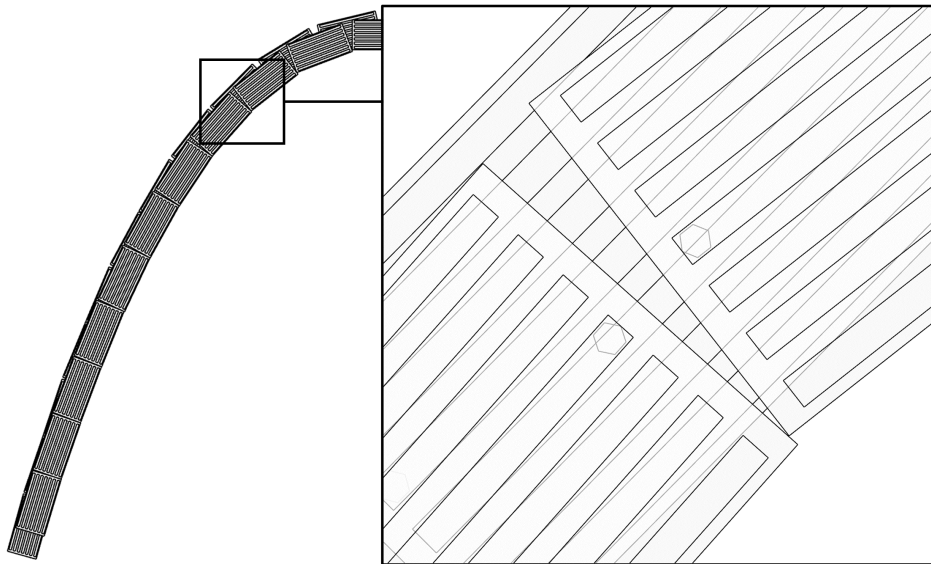


Figure 3.5: Tessellation detail for initial vault model

3.3 Geometric constraint solving

3.3.1 Implementation

Geometric constraint solving is implemented with Kangaroo2, which takes the initial model generated according to Figure 3.4, and rearranges the components so that they are connected between consecutive courses through mechanical interlocking. As explained in Chapter 2, this mechanical interlocking is necessary to recreate the self-supporting effect normally achieved in a Nubian vault with mortar. A Nubian-type vault assembled from mechanically interlocking components cannot be defined using standard geometric logic in Grasshopper because the position of each component in one course depends on the positioning of components in the previous course in order to satisfy interlocking requirements, resulting in an irregular, recursive definition of block positions throughout the model. As mentioned in Chapter 3.2.2, the purpose of applying geometric constraint solving is to reconfigure the initial model to satisfy mechanical interlocking, while ensuring that other physically-necessary constraints are met.

The implementation of geometric constraint solving revolves around three main constraints required to ensure structural viability of the models, which are presented in Figure 3.6. These constraints are block collision, mechanical interlocking, and in-plane confinement. Block collision ensures that components do not intersect each other; mechanical interlocking requires that any given component's pins interlock with the grooves of a component in the previous course; planar confinement prevents out-of-plane rotations or movements of the blocks during solving to ensure that each course is a planar configuration of components. These constraints are solved recursively for each course in the model using the Kangaroo Zombie Solver in combination with the Octopus Loop component. To ensure that the geometry output from the simulation still results in a compression-only vault, simple Grasshopper logic is used to check that each component is intersected by an in-plane thrust line at both of its ends.

3.3.2 Challenges

Several challenges arose during development of the modelling framework and warrant brief reflection. The main challenge was to define an initial model that could readily be solved by the Kangaroo solver without contradictory constraints. The initial tessellation method for the vault did not minimise overlapping between components because it was believed that this would be corrected during simulation using the "Block collision" constraint. This presented a problem, however, because the mechanical interlocking constraint is defined by assigning a pin to "snap" to the nearest groove based on the initial configuration of the model; contradictory logic arose because solving the "Block collision" constraint resulted in significant displacement of each component from its initial position, which meant that the original pin-groove assignment was no longer valid. This challenge was addressed by using a tessellation method that minimised the overlap between components in the initial model.

Sensitivities to geometric tolerances arose as well. The tolerance for the Kangaroo solver needs to be set to a very small value ($1e-15$) to prevent the corners of neighbouring components from being joined together.

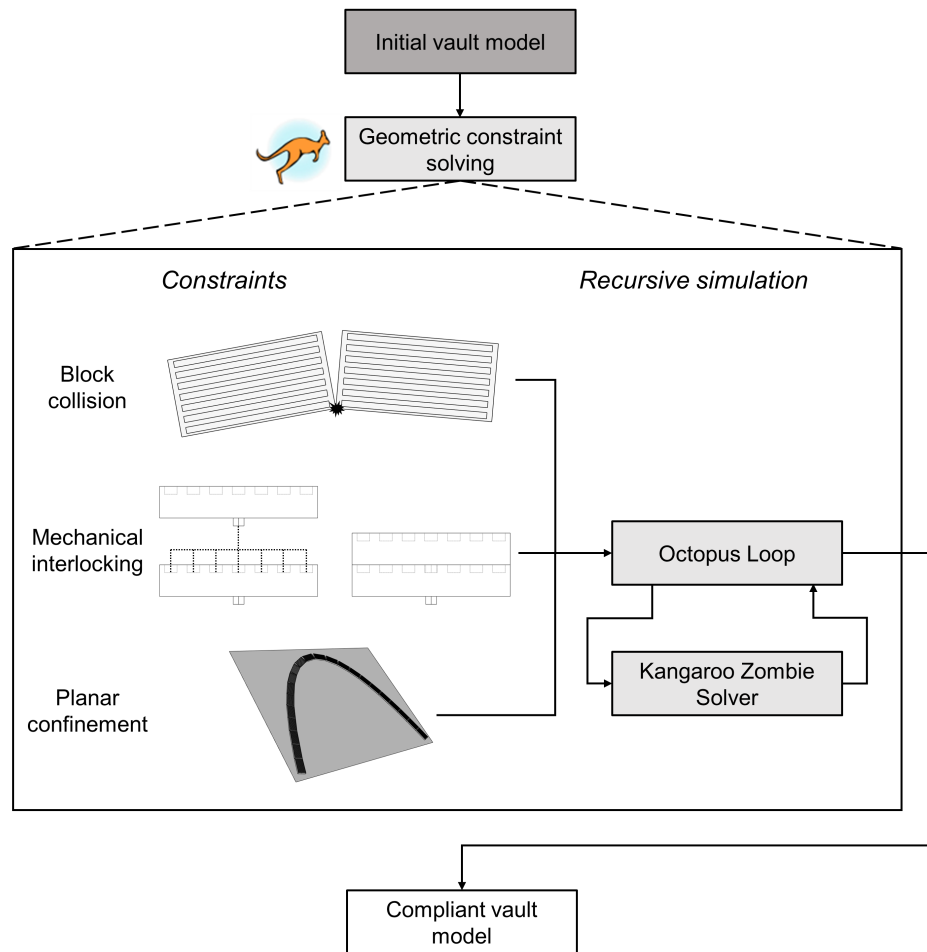


Figure 3.6: Flowchart of logic for Kangaroo simulation

The tessellation method used results in these corner points being close together, as shown in Figure 3.5, and for the default tolerance value in Kangaroo, they tend to be merged into one point.

3.4 Resulting vault model

After all courses in the global vault geometry are simulated, the result is a physically viable assembly of mechanically interlocking components. An example of the resulting vault geometry is shown in Figure 3.7. Such a model is subsequently imported into 3DEC for analysis using the approach mentioned earlier.

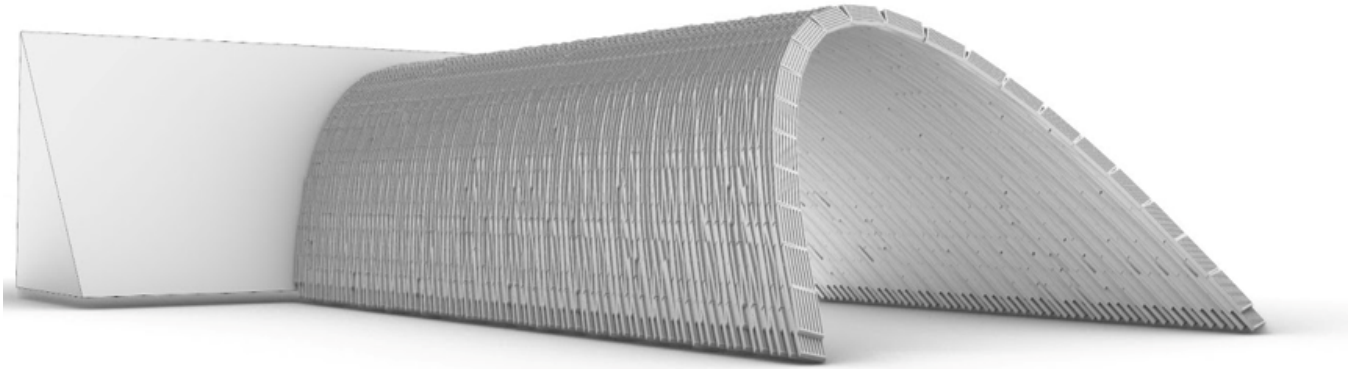


Figure 3.7: Resulting geometry

3.4.1 Continuity enforcement

One final step is necessary to ensure that the vault models are sufficiently stable, which is to add wedge-like blocks between components in each course. These wedges fill gaps that exist due to relative rotations between blocks in any given course. Closing these gaps establishes continuous in-plane load paths and prevents excessive rotation of the blocks during loading. In reality, continuity may be enforced by filling gaps between components with loose rocks or packed regolith, but it may also be possible to create close-fitting wedges from sintered regolith.

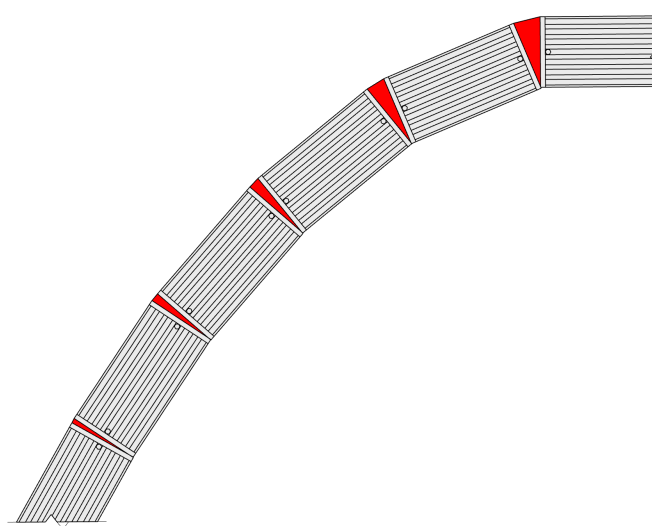


Figure 3.8: Continuity enforcement

3.5 Distinct element modelling

After a viable geometric definition of the vault is obtained in Rhino, the model must be translated into a 3DEC model for analysis. This step is reflected in the right side of Figure 3.1, which relies on iterative methods employed in Python to import models into 3DEC. For distinct element analysis in 3DEC, two model types are possible: rigid and deformable. As described in Chapter 2, the use of rigid blocks is common in masonry analysis, but deformable blocks are needed in certain cases. Methods for generating both types of DE models are presented in this section, although most analyses in this project focus on the use of rigid blocks.

3.5.1 Generating 3DEC models with rigid blocks



Figure 3.9: Rigid block model generation

Figure 3.9 summarises the main steps of rigid block model generation. Once a compliant model is obtained through geometric constraint solving, the geometry must be exported as a VRML file. As explained in Chapter 3.2.1, each unit in a given vault model is represented by a group of constituent elements, as shown in Figure 3.2. In the VRML representation of the vault geometry, the order of the elements is consistent with the group-based definition for each component. This allows for the geometry to be imported into 3DEC in one step as a collection of individual rigid blocks, which a Python script iterates through and joins into rigid assemblies corresponding to each unit. Additional model geometry such as the wedges described in Chapter 3.4.1 and boundary supports can be exported from Rhino and directly imported into 3DEC as VRML files. The definition of boundary supports is described in Chapter 4.

3.5.2 Generating 3DEC models with deformable blocks

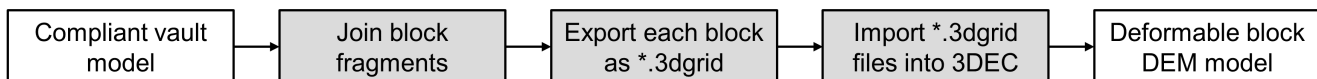


Figure 3.10: Deformable block model generation

Figure 3.10 summarises the main steps of generating 3DEC models with deformable blocks. As mentioned in Chapter 2.4.2, deformable blocks allow for the representation of continuous displacement fields, which is needed for the analyses carried out in Chapter 8. With a deformable block modelling approach, the component geometry does not need to be discretised into constitutive pieces. Rather than creating a new definition of the component geometry which produces a single element, the fragments defined in the initial approach are joined together into a closed polysurface in Rhino. This new block definition can easily be placed into the simulated positions of components in the compliant vault model to create a global model compatible with

a deformable block approach. With this new model, the Griddle component by Itasca Consulting Group Inc. (2019) is used to export each block in the model as a *.3dgrid file. These files are then imported into 3DEC to generate deformable blocks. In this project, deformable block modelling is used for studying the influence of covering the vault with loose regolith. When modelling approximately continuous media such as soil, deformations cannot be assumed to occur at joints as in rigid blocks, so the loose regolith must be modelled using deformable blocks.

Chapter 4

NUMERICAL ANALYSIS FRAMEWORK

4.1 Overview

As depicted in Figure 1.1, several Analysis Phases were carried out in this project in order to design a vaulted shielding structure that may safely resist moonquake loading. The analysis methods in each Analysis Phase share fundamental similarities that are summarised in this chapter as a framework in order to avoid redundancy in the following chapters. Analysis Phases I, II, and III applied similar quasi-static pushover-type analyses to several variations of the vault geometry. Dynamic time-history analysis was carried out for the final vault model in Analysis Phase II. Out of the additional analyses that were investigated, the methods for studying the influence of regolith overburden and gravity variation share the same basic characteristics as the main Analysis Phases. The analysis of the equivalent monolithic vault geometry is based on a different methodology, however, which is described in Chapter 8.

4.2 Boundary conditions

The various analyses carried out in the three Analysis Phases share a common set of assumptions about boundary conditions. As explained in Chapter 2, the Nubian-type vault geometry studied in this project must be supported by an inclined surface in addition to the ground surface. The inclined support is modelled as a rigid block composed of a triangular prism. Boundary conditions are defined by assigning interface properties to the contacts shared between the base course and the inclined support block. In the interest of following a conservative approach for the quasi-static analyses, the interface properties set at this boundary are the same as those defined for the interfaces between components, which allow for some degree of sliding in the plane of the support. Preliminary analyses indicated that assigning fixity to the base course would result in an overly-stiff, unconservative response in the quasi-static analysis due to the interlocking of rigid blocks. Furthermore, rigidly attaching the base course to the inclined support was expected to produce an undesirable response in dynamic time history analysis, where the ground motions would be directly applied to the base course. In seismic design, base isolation can significantly improve structural performance, so there would be limited justification for rigidly anchoring the base course in practice. There is no apparent reason why a predominantly friction-based interface may be infeasible in practice, so it is reasonable to assume that the boundary condition at the inclined support is defined by such an interface. In the interest of simplifying the problem, it is justifiable to assume uniform interface properties at this stage of development of the vault design. Future studies should be carried out to study the influence of varying properties at this boundary, but it is considered to be out of the scope of this project.

The remaining set of boundary conditions to be defined are those that define the interaction between the ground and the vault. The details of a suitable foundation design are out of the scope of this project, but it

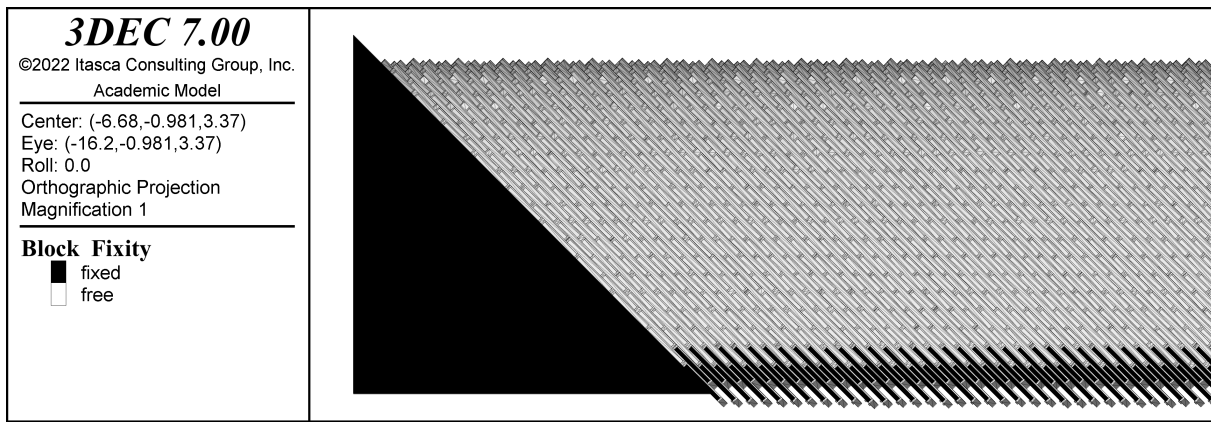
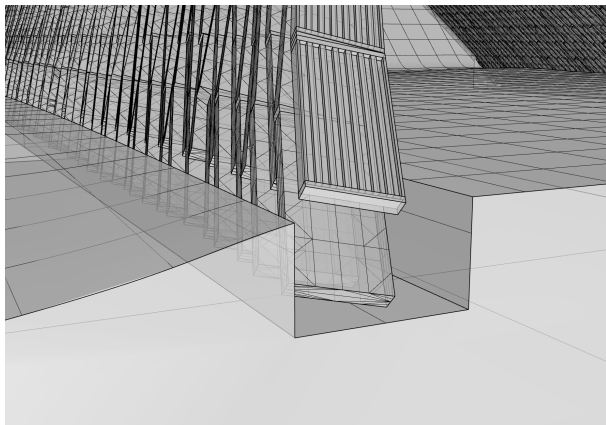
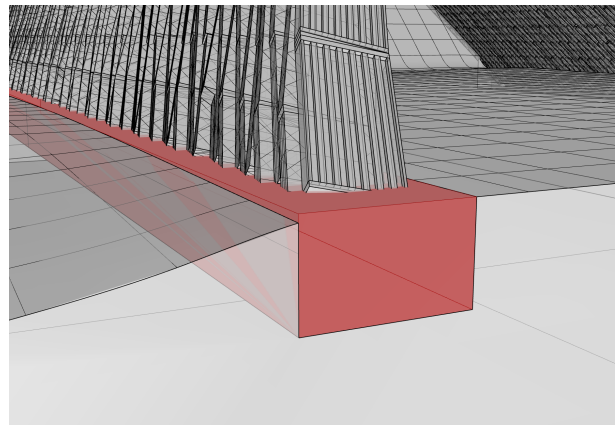


Figure 4.1: Illustration of boundary conditions

is reasonable to assume that the components at the ground level will be anchored to the ground in some way. To simplify the problem at hand, the ground-level components are assumed to be fixed in place. The assumed fixity of blocks nearest to the ground is reflected in Figure 4.1, with fixed blocks marked in black. This could be accomplished by partial embedment into the Lunar surface, followed by backfilling, as illustrated in Figure 4.2.



(a) Embedment of vault into Lunar surface



(b) Anchoring developed through infill

Figure 4.2: Illustration of potential foundation system leading to fixed condition of ground blocks

4.3 Block type

In Chapter 2, the use of rigid blocks was identified to be a common assumption for DEM analysis of masonry structures, including dry-stone masonry. This is because inter-block movements typically govern structural behaviour in these cases, and because of their advantage in computational efficiency (Lemos, 2019). Therefore, rigid block models were used for all the main analyses undertaken in this project. Initial attempts were made to implement deformable blocks using the approach presented in Chapter 3.5.2, but creating full-sized deformable models was deemed to be infeasible due to prohibitively large file sizes. Deformable blocks were implemented on a small scale, however, using simplified components when studying the influence of regolith overburden in Chapter 9.

4.4 Material definition

As described in Chapter 2, there are several potential ways to produce structural materials out of regolith. The materials produced using different methods vary significantly in terms of their reported mechanical properties, but results are relatively consistent between studies that use similar processes. In this project, it is assumed that the structures modelled according to Chapter 3 can be fabricated using conventional sintering or melting methods. These methods have produced consistent results within the context of regolith-based manufacturing, demonstrating that Lunar soil is compatible with current technology based on radiant resistive and microwave heat sources. Reference was made in Chapter 2 to two studies which sufficiently document the mechanical properties of conventionally sintered regolith: Hoshino et al. (2016) and Indyk and Benaroya (2017). The results from Indyk and Benaroya (2017) are used to define the fundamental material properties of blocks in each 3DEC model, which are summarised in Table 2.3. Neither of the referenced studies obtained values for the friction angle, so a value of 40° is assumed based on typical values for dry-stone masonry according to Marino et al. (2014).

For rigid block models, stiffness is lumped at the joints, and thus appropriate values for stiffness of contacts can be approximated by dividing the elastic stiffness parameters, E and G , by the spacing between block centroids, s in the normal direction (Gonen et al., 2021; Lemos, 2007). The interface stiffness properties are calculated as follows:

$$k_n = \frac{E}{s}; k_s = \frac{G}{s} \quad (4.1)$$

The exact mechanisms of force transfer in this type of vault have not been studied in previous literature, so the definition of joint spacing is not immediately evident. In an essentially 2-dimensional assembly of components such as a wall, the joint spacing is clearly defined as the vertical distance between component centroids because the only forces acting normal to the block's faces are aligned vertically. The flow of forces in the vault is expected to be defined by a combination of in-plane and out-of-plane stiffness properties due to the existence of force components in both of these directions. The upper-bound stiffness will be defined by the out-of-plane distance between component centroids, while the lower bound stiffness will be defined by in-plane distance between centroids. These alternatives are pictured in Figure 4.3

All vault models studied in this project use the same component height of 0.1 m, so the upper-bound stiffness is based on a joint spacing equal to this height. Defining the in-plane, lower bound stiffness value is more nuanced. In the real vault model assembled from interlocking components, wedge-like blocks are used to fill gaps between components. The presence of these wedges confounds the definition of in-plane interface stiffness due to variations in their dimensions. As shown on the right side of Figure 4.4, wedges are absent in some parts of the vault model, which results in an interface spacing defined as the distance between component centroids. Since this case results in the lowest possible value for in-plane interface stiffness, a simplified, conservative approach can be taken where the lower-bound stiffness definition for all joints is based on the distance between block centroids, which is 1.0 m.

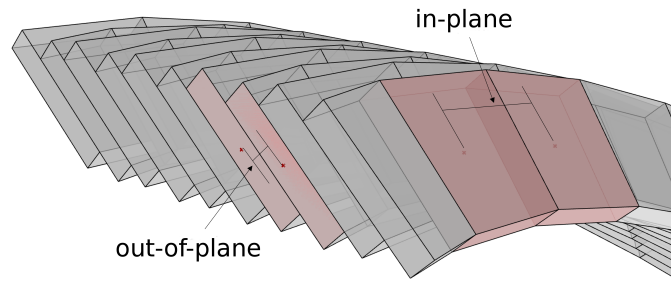


Figure 4.3: Illustration of in-plane and out-of-plane interface spacing

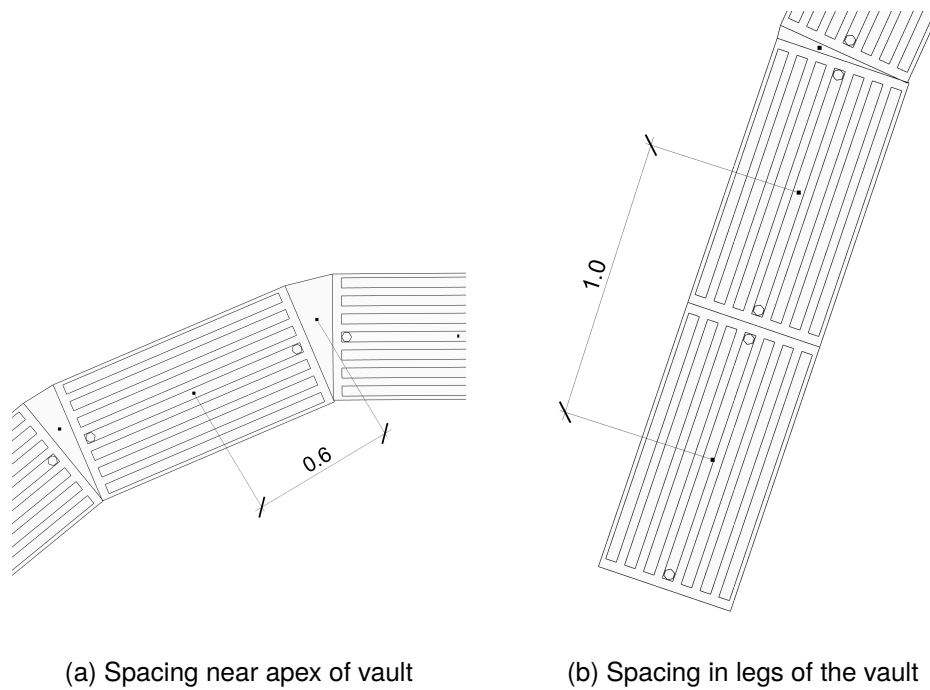


Figure 4.4: Illustration of irregularities with in-plane interface spacing for simulated courses

Based on the above considerations, two different spacing assumptions are used for defining interface stiffness in the Analysis Phases, which result in the set of interface properties presented in Table 4.1. These are considered to be lower and upper bound stiffness values, respectively.

Spacing (m)	k_n (MPa/m)	k_s (MPa/m)	ϕ (deg)
1.0	8.36E+03	3.30E+03	40
0.1	8.36E+04	3.30E+04	40

Table 4.1: Assumed interface properties

4.5 Configuration of quasi-static analyses

Quasi-static pushover type analyses are conducted in each of the Analysis Phases as the main method of assessing the seismic performance of any given model. The theoretical basis for using quasi-static pushover-type or tilt table analyses was covered in Chapter 2, where these methods were shown to be a standard way of assessing the seismic performance of masonry structures. Boundary conditions, block type, and material properties are defined according to the steps described in the previous sections. As explained in Chapter 2.4.2, local damping must be defined for static problems. The default value of 0.8 is used for local damping values throughout this project. As explained in Chapter 3, The analyses were carried out in 3DEC using a Python script whose logic is shown in Figure 4.5.

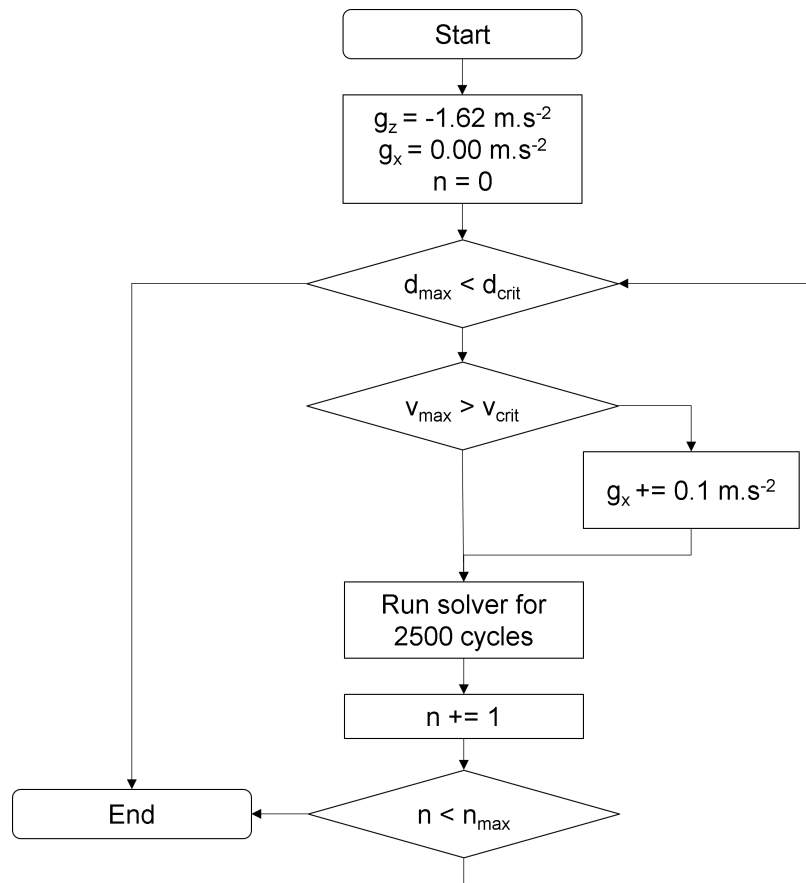


Figure 4.5: Pushover script flowchart

In the analysis, a given model is first allowed to settle under the vertical component of gravity, 1.62 m s^{-2} , after which it is subjected to a uniform lateral acceleration which increases in increments of 0.1 m s^{-2} . After the application of each load step, the solver in 3DEC is cycled until either equilibrium or cutoff criteria are reached, after which the next load step is applied. The model is assumed to be in equilibrium when v_{max} is less than or equal to 0.001 m s^{-1} (v_{crit}). The first cutoff criterion is based on the maximum number of solve cycles (n_{max}); if the model does not reach equilibrium by the time that it has gone through a given multiple of 2500 cycles (typically between 50 and 200), the next load step is applied. This is done in the interest of increasing computational efficiency - initial trials showed that if a maximum loop count was not set, the

final load steps took an excessively long time to converge without significantly changing the state of the model. Although this approach may lead to a slight degree of artificial stiffening in later loading stages due to incomplete convergence, deformations did not increase significantly if these later steps were allowed to reach the equilibrium condition. The second cutoff criterion is based on the maximum displacement (d_{max}) in the model, which defines the point at which the entire analysis is terminated. If any block is displaced in the direction of loading by more than a critical value (d_{crit}), the analysis is interrupted and the model is deemed to be in a "failed" state. It is important to clarify that due to a lack of precedent for the structural design of this type of vault, a precise failure criterion is difficult to define; the chosen maximum displacement value is somewhat arbitrary and does not correspond to what can be considered true structural failure. In this case, a maximum displacement was chosen based on the displacement where significant permanent deformation was observed. The vault was still stable at this point and could be subjected to further loading. The specific cutoff value for maximum displacement may vary between analyses, but will be clearly stated in each of the Analysis Phase chapters.

4.6 Configuration of dynamic analyses

For dynamic analysis, 3DEC models were reconfigured with the *model configure dynamic* and *model dynamic active on* commands. Rayleigh damping was specified, but both the mass and stiffness parameters were set to 0.0 in order to achieve an undamped analysis. This approach was taken due to the prohibitively long computation time caused by the inclusion of damping. The undamped results obtained are considered to be a preliminary, conservative approximation of the dynamic behaviour of the vault. To represent seismic actions on a given model, the velocity time history for a moonquake is applied to the fixed blocks in the model, which were defined in Figure 4.1. At this stage, dynamic loading is only considered in the in-plane direction of the vault, as shown in Figure 4.6.

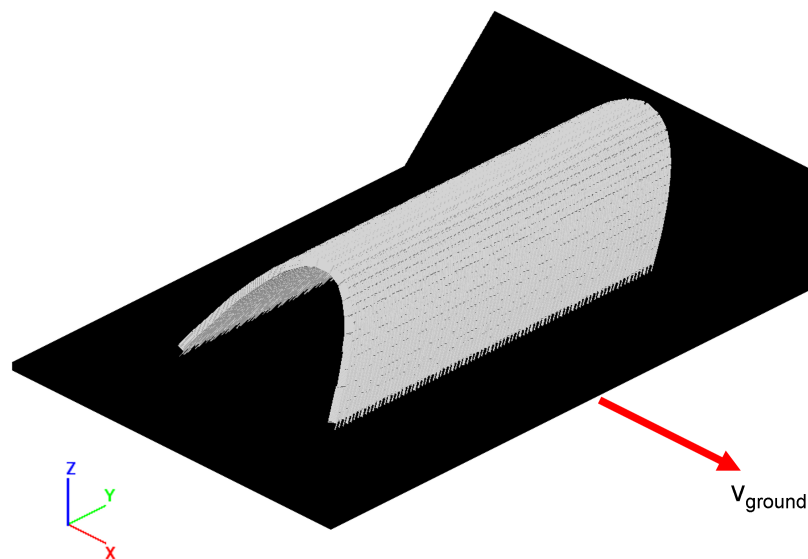


Figure 4.6: Application of ground motion data in 3DEC

Ground motion time histories are obtained using the methods outlined in Chapter 2.3.3. As mentioned in Chapter 2.3, moonquake data is scarce due to a number of factors, so directly usable ground motion records do not exist. Luckily, the preliminary probabilistic seismic hazard analysis carried out by Ruiz et al. (2022) resulted in a uniform hazard spectrum which can be used to obtain representative moonquake time histories. This spectrum is shown in Figure 2.7. In this project, two methods of generating ground motion data from the design spectrum were considered based on common practices in earthquake engineering: matching natural earthquake data to the hazard spectrum through a database such as PEER, or generating artificial ground motion data with software such as SimQKE. Given that artificial ground motion data typically matches a desired hazard spectrum more accurately, this approach was considered to be more appropriate. As a result, SimQKE was used to generate an artificial acceleration time history according to the configuration illustrated in Figure 4.7. As shown in Figure 4.7a, the design value for spectral acceleration, S_d is established by inputting the governing natural period of the vault, which was obtained through eigenvalue analysis in Chapter 6. For the parameters shown in Figure 4.7b, default values were used due to uncertainties regarding reasonable moonquake time-history characteristics.

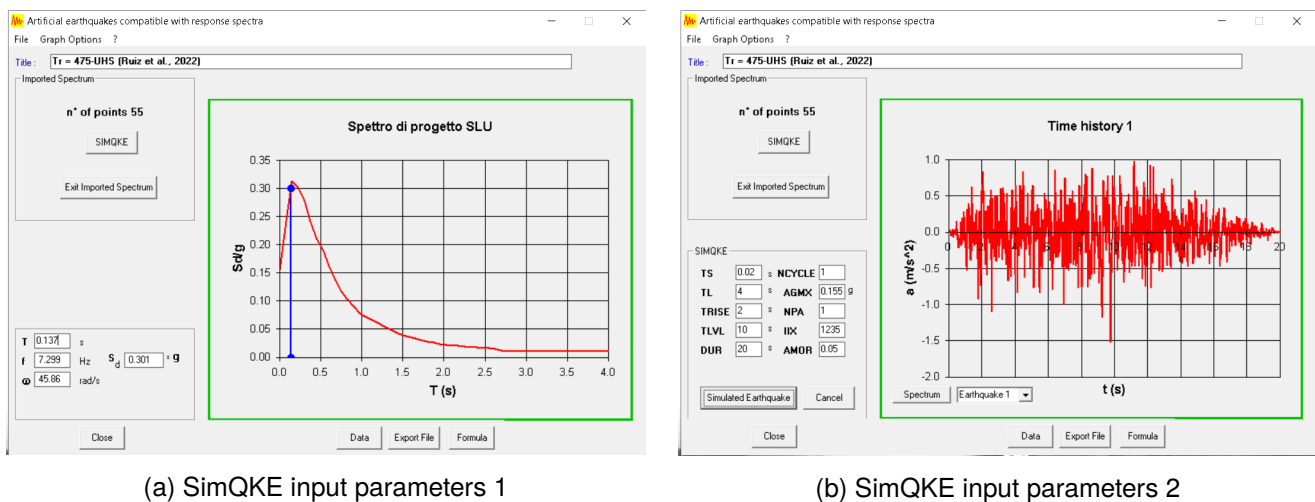
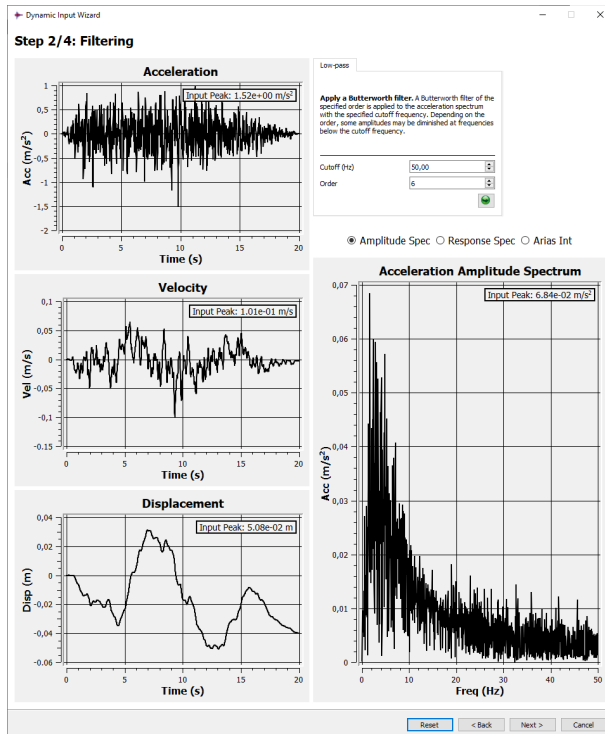
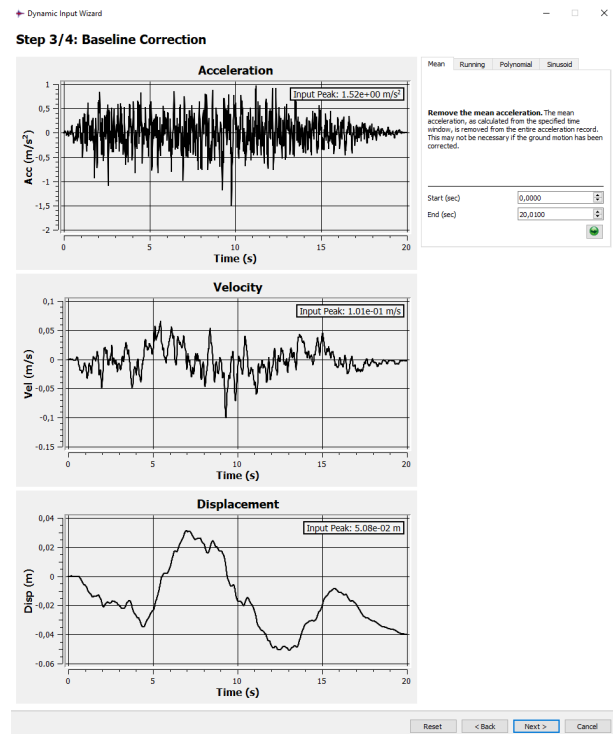


Figure 4.7: SimQKE configuration

Once an acceleration time history is obtained which represents the seismic loading for a 475-year moonquake, it must be processed into a velocity record to be compatible with the solving scheme in 3DEC. This is accomplished using the "Dynamic input wizard" tool in 3DEC. As shown in Figure 4.8, the dynamic input can be filtered and corrected to increase the quality of the time history data. No filtering was applied in this case because the record was artificially generated, so no noise was expected in the signal. A small degree of baseline correction was applied according to Figure 4.7b. The output from this process is a text file containing a table of velocity values for timesteps of 0.01 seconds. A Python script was written which makes 3DEC iterate through the table during the solving algorithm, applying the given velocity value at each timestep to the base block shown in black in Figure 4.6. In the interest of computational efficiency, the velocity history was truncated such that the most destructive ten seconds of the record are used. This period corresponds to the interval between 5-15 seconds in the velocity history shown in Figure 4.8.



(a) 3DEC dynamic input - filtering



(b) 3DEC dynamic input - baseline correction

Figure 4.8: Dynamic input configuration

ANALYSIS PHASE I - PARAMETRIC STUDIES OF IDEALISED VAULT GEOMETRY

5.1 Overview

Given the novelty of the chosen vault geometry, there is limited precedent in literature to determine which configuration of geometric parameters may lead to optimal seismic performance. Preliminary analysis determined that in combination with microgravity, the lateral loading caused by moonquakes could pose significant issues with stability for Nubian-type vaults. Therefore, further investigation into increasing the seismic capacity through parametric geometry variation was warranted. The basic parameters of rise and span defined in Chapter 4 are based on a top-down approach that must satisfy existing requirements such as habitat module size, but several parameters can be varied while achieving those overall dimensions. As such, the first Analysis Phase sets out to determine how the variation of key geometric parameters influences the seismic capacity of inclined Nubian-type vaults, and what configuration may result in adequate performance for the moonquake loading defined by Ruiz et al. (2022). OpenArch (McLean et al., 2021) was explored at an early stage of the project to determine the minimum thickness of kinematically-stable arches under moonquake loading, but this approach could not be reliably adapted to a study of inclined arches.

5.2 Methodology

In order to understand the influence of key global geometric parameters on dry-stone Nubian-type vault performance, idealised models without mechanical interlocking are first studied. This is done because imposing the mechanical interlocking constraint results in irregular tessellation, as shown in Figure 3.7. These irregularities may confound the influence of other parameters due to unpredictable local variations in geometry. Furthermore, as explained in Chapter 2.2.2 and Chapter 3.2.1, the purpose of mechanical interlocking is primarily to maintain structural integrity during the assembly of each course, with kinematic equilibrium governing the stability of the completed vault. By studying models with perfect tessellation and no interlocking, this Analysis Phase can more confidently investigate the fundamental parameters which govern the structural behaviour of inclined vaults. The workflow diagram in Figure 5.1 provides an overview of the structure of Analysis Phase I.

First, idealised inclined arches with varying geometric parameters are modelled. Specifically, component width and course inclination are varied. For each set of parameters, the arch geometries are duplicated and stacked together to create analogous partial vault models with ten courses, whose performance is analysed. The results from these analyses provide insight into what parameters yield maximum capacity for seismic loading. These optimal parameters are used to define larger scale models at different construction stages with 50, 100, and 200 courses. The final stage was chosen to have 200 courses in order to approximate the full-scale vault used as reference in Figure 2.4. For this final vault geometry, 170 courses are needed,

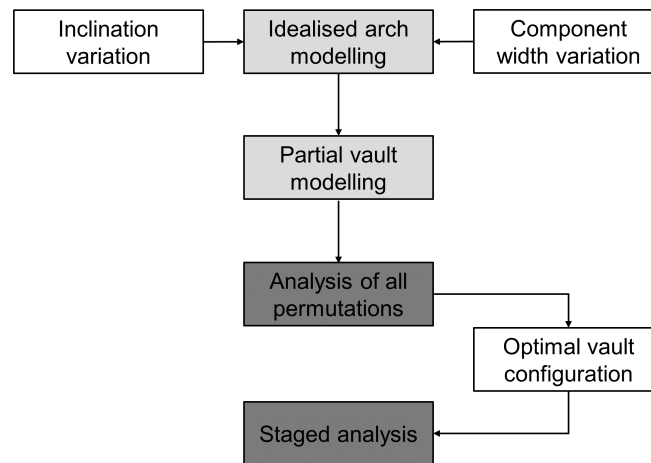


Figure 5.1: Analysis Phase I workflow

assuming a component height of 0.1 m and an inclination of 45° . By comparing the performance of a given vault geometry with an increasing numbers of courses, the evolution of stability at different stages of construction can be understood. The results of this Analysis Phase are used to inform the design of a final vault geometry with mechanically interlocking components, which is thoroughly analysed in Analysis Phase II.

5.2.1 Modelling approach for idealised vaults

Idealised arches were initially modelled according to the steps shown in Figure 5.2. For any given combination of the global parameters, an envelope of the arch was defined based on the component width. This boundary was then intersected by a series of radial planes to generate voussoirs, which are the components which constitute an arch. The arch geometry was then duplicated into a series of courses with an alternating offset joint pattern, pictured in Figure 5.3. This process was used to create the idealised vault models shown in Figure 5.8.

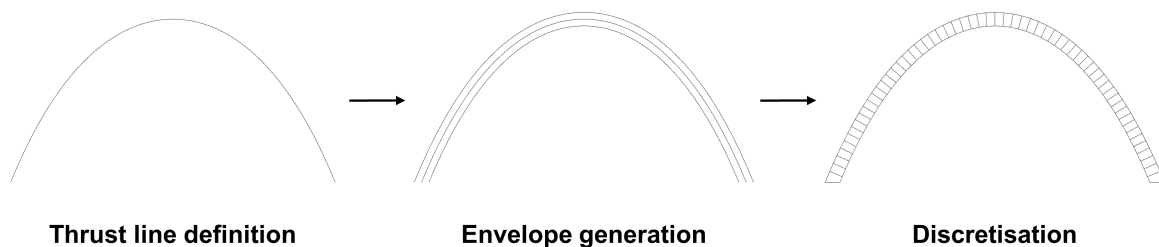


Figure 5.2: Idealised arch modelling procedure

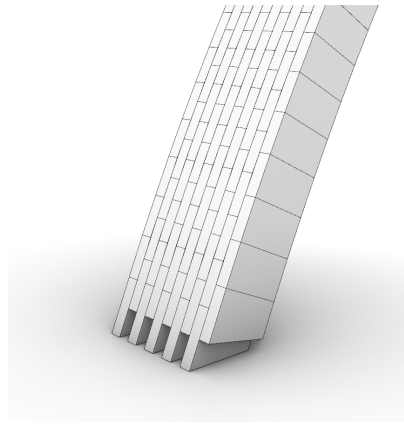


Figure 5.3: Illustration of offset joint pattern employed for idealised vault modelling

5.2.2 Primary parameter definition

The main global parameters which can be varied while maintaining a predefined rise and span are component width and inclination, depicted in Figure 5.4 and Figure 5.5 respectively. These primary parameters result in idealised arch models, whose geometry is duplicated to create vaults with varying numbers of courses. These vaults are further embellished based on several secondary parameters defined in the following section.

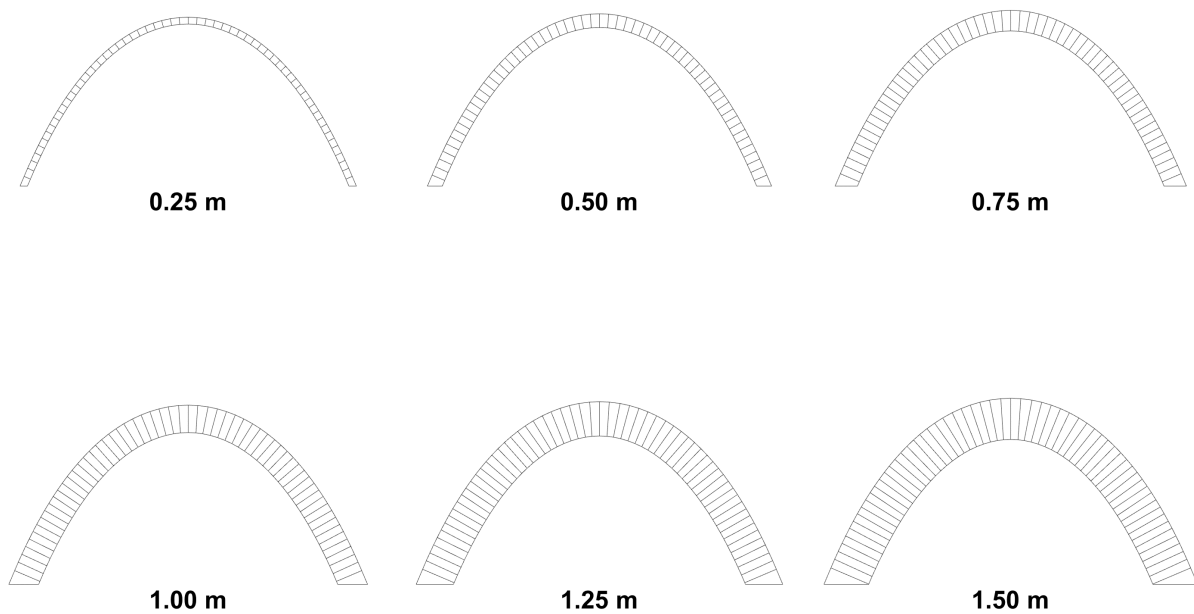


Figure 5.4: Variation of component width

The smallest component width was chosen to be 0.25 m because components with this width were studied in initial trials and were shown to lead to insufficient seismic capacity, which indicated that including narrower components in the parametric study was unlikely to yield useful results. Despite this component width resulting in poor seismic capacity, it was used as the lower bound width in the parametric study because of the possibility that varying inclination could significantly improve its performance. The upper bound was

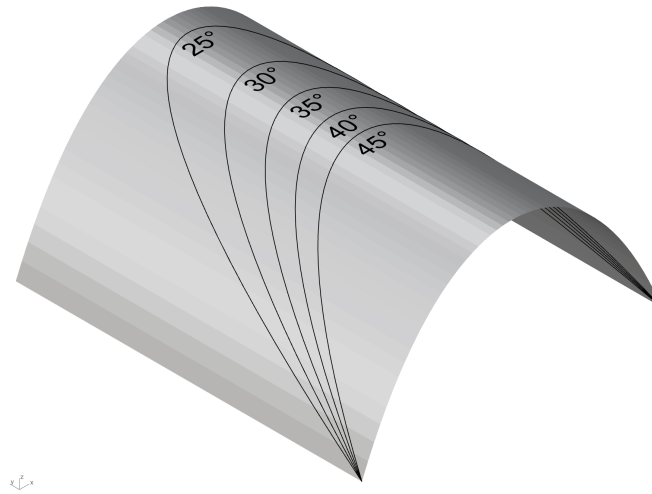


Figure 5.5: Variation of inclination

chosen to be 1.5 m based on the judgement that wider components may be too large in proportion to the overall geometry and could result in problematic stereotomy.

Inclination angles are defined relative to the ground plane, the smallest of which is chosen to be 25°. Any angle smaller than this would result in the 0.25 m wide components experiencing an overhang larger than the component width, which is not physically possible. Figure 5.6 shows how for an inclination of 25°, the components in one course are barely supported by the preceding course. The upper bound of inclination values was set as 45° based on preliminary analyses, which showed that larger angles exhibited diminished performance.

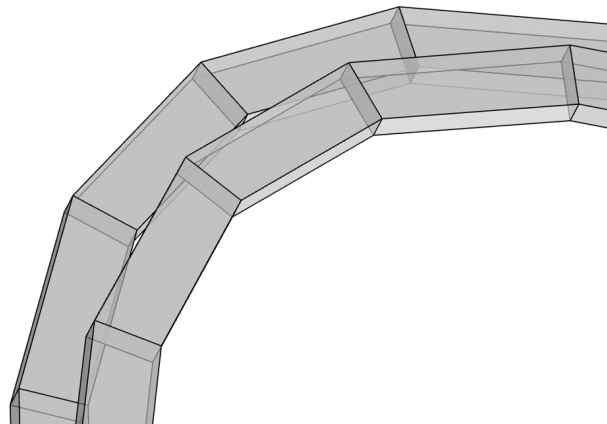


Figure 5.6: Overhang for 0.25 m wide components with a 25° inclination

5.2.3 Secondary parameter definition

Thrust surface shape was identified as potentially important to study in order to understand how to define the final model studied in Analysis Phase II. It is initially assumed that the global form of the vault governs the flow of forces within. In other words, as long as the components are arranged into a global funicular

shape, the structure is assumed to have compression-only load paths. The nature of dry-jointed structures makes it unclear whether this is an appropriate assumption in this case, however, since it is possible that in-plane, rather than global kinematic relations will have a dominant influence on the overall stability due to the sliding that can occur at component interfaces. In other words, it is unclear if the global form of the structure will be activated as one thrust network, or if kinematic equilibrium will be defined by stability considerations in the individual courses. This is important because if in-plane effects dominate the structural behaviour of dry-stone inclined vaults, the courses should not be defined based on an intersection with a funicular thrust surface—the curves that result from such an intersection are not funicular, as shown in Figure 5.7. It may be more appropriate to define the global form of the structure based on the extrusion of a curve that is funicular in the inclined course plane, although Figure 5.7 does suggest that the difference between what is considered the "real" thrust line and the "ideal" thrust line becomes negligible for increasing inclination angle. Therefore, results for the "real" thrust line are emphasised to be consistent with the modelling framework in Chapter 3.

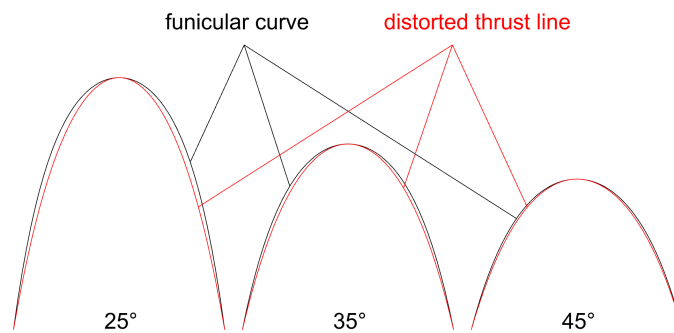


Figure 5.7: Deviation of thrust line shape from funicular curve

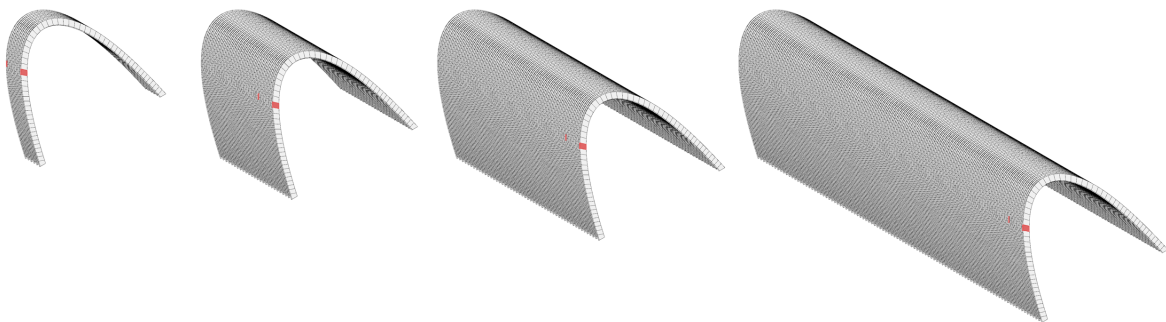


Figure 5.8: Vault model at different construction stages

5.2.4 Analysis setup

All analyses in this Analysis Phase follow the assumptions defined by the analysis framework in Chapter 4. The only point that requires clarification is that the upper bound for interface stiffness was used. This

choice was made because emphasis was placed on studying inclination angles smaller than 45° - for these inclinations, it was believed that out-of-plane stiffness lumping governs the behaviour because a significant proportion of self-weight is resisted by a reaction in the out-of-plane direction. Please refer to Figure 4.3 in Chapter 4 for information about how stiffness is lumped together into the zero-thickness interfaces. This assumption may lead to an overestimation of interface stiffness for inclination angles as they approach 90° because the out-of-plane reaction decreases to zero as the inclination becomes vertical, and thus the in-plane dimensions of the blocks will likely define how their stiffness should be lumped together. The assumptions for boundary conditions follow the assumptions outlined in Chapter 4, namely that the first course is supported by an inclined support and that the components closest to the ground are assumed to be fixed, as in Figure 4.1. Material assumptions also consistent with those defined in Chapter 4.

Quasi-static pushover-type tests were conducted according to the configuration outlined in Chapter 4. Two main blocks common to each of the models were tracked for the displacement results used to define pushover curves, as shown in Figure 5.8. These blocks are defined based on the location where maximum displacements are expected based on hinge formation mechanisms described in Chapter 2.4.1. All analyses in this chapter report results for the gridpoint closest to the centroid of the outermost tracking block. As mentioned in the analysis framework in Chapter 4, a maximum displacement must be set at which the pushover test will be terminated. For the analyses in this Analysis Phase, this cutoff displacement was chosen to be 0.02 m because this limit was shown to conservatively capture the essential characteristics of instability evolution in the vaults. As will be shown in the results, the onset of instability actually occurs for much smaller deformations. Still, it was deemed useful to collect data for later stages of loading in the event that it might lead to additional insight about post-stability behaviour of the vaults.

5.3 Results

5.3.1 Partial vault models

5.3.1.1 Primary parameter variation

The main parameters varied in this part of the Analysis Phase were inclination and component width. Figure 5.9 shows the resulting pushover curves for a series of quasi-static analyses. The curves are grouped into separate subplots based on component width, which illustrates how the pushover behaviour of the vaults is related to inclination. The subplots share the same axis definitions and limits, where the Y-ordinate represents the applied lateral acceleration, and the X-ordinate represents the lateral displacement of the gridpoint in the outer course, as defined in Figure 5.8. It is important to note that the displacement labels are scaled by a factor of $1e-4$. For a component width of 0.25 m and an inclination of 25° , the plot is not visible because the model experienced significant displacement under self-weight. Generally, the acceleration at which each model loses stability tends to increase as inclination increases, although there are some irregularities which obscure this trend. Notably, for component widths larger than 0.5 m, the positive correlation between component width and resistance to lateral acceleration becomes convoluted as the pushover plots exhibit

significant overlapping.

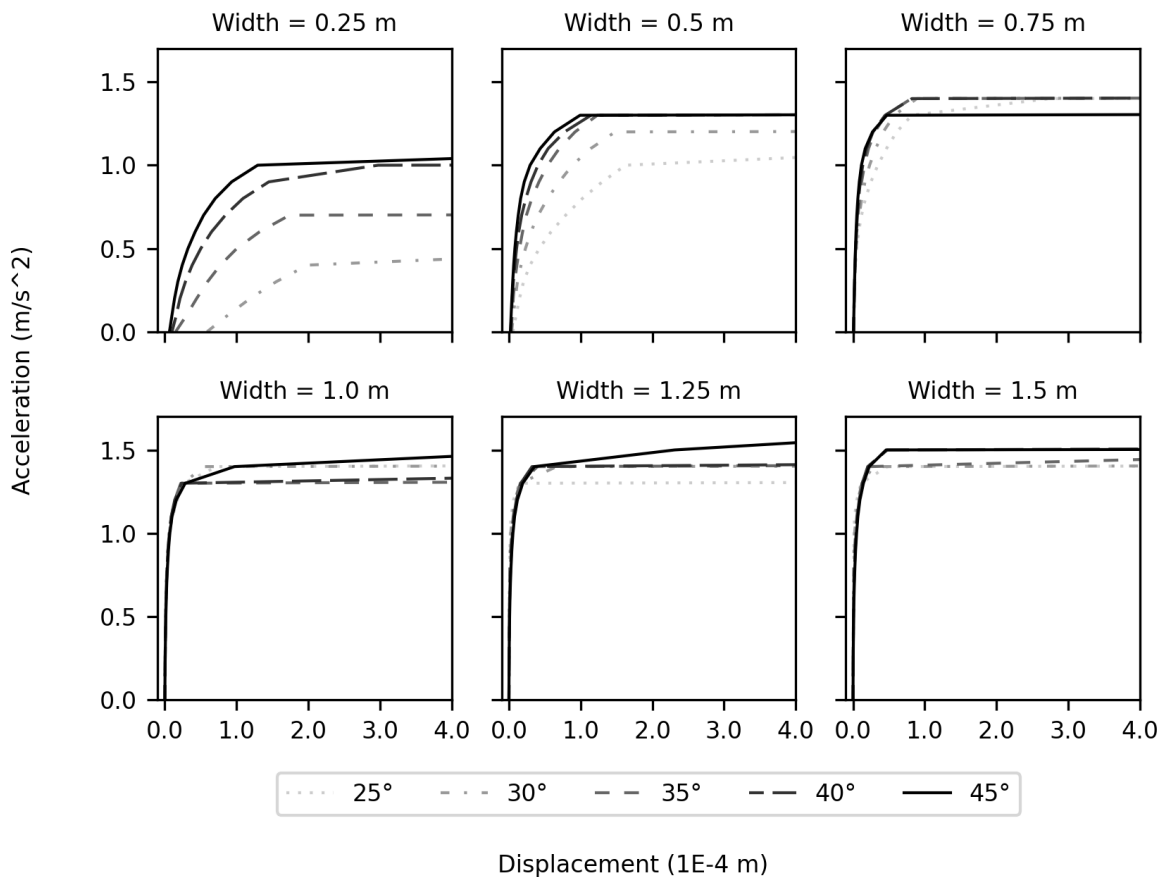


Figure 5.9: Variation of inclination for various component widths (realTL)

Figure 5.10 presents the same pushover curve data as Figure 5.9, except that subplots are grouped based on the inclination rather than the component width. This figure clearly illustrates the influence of component width variation for each value of inclination, with the capacity for lateral acceleration increasing as component width increases. As with Figure 5.9, there are some irregularities in the results, leading to overlaps between peak acceleration values.

Based on the results of the parametric modelling and subsequent studies of component width variation, the optimal vault configuration should have a component width of 0.5 m. Several issues with using components wider than 0.5 m were identified: such large components may be problematic for tile or brick-based design given that their size is large with respect to the global geometry, so there is limited confidence that the components can be accurately modelled as rigid blocks; additionally, these components are likely infeasible from a manufacturing perspective; finally, preliminary attempts to simulate vaults with interlocking components of width 0.75 m and above show that tessellation with such components results in a problematic discretisation. Figure 5.11 illustrates how such large component sizes appear to be unreasonably large with respect to the overall vault dimensions. Additionally, such large widths lead to excessive openings between

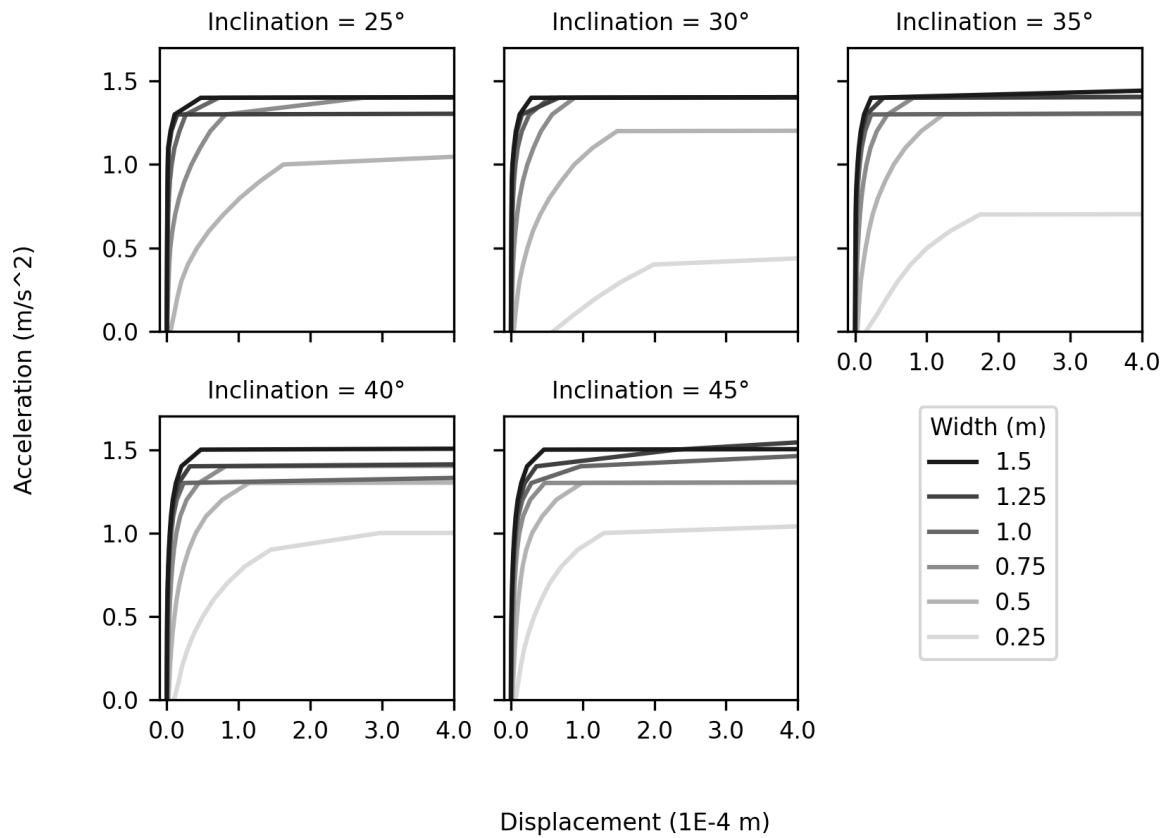


Figure 5.10: Variation of width for various inclinations (realTL)

components due to sharp curvature at the apex of the vault. These gaps present difficulties in relation to the concept of continuity enforcement described in Chapter 3.4.1.

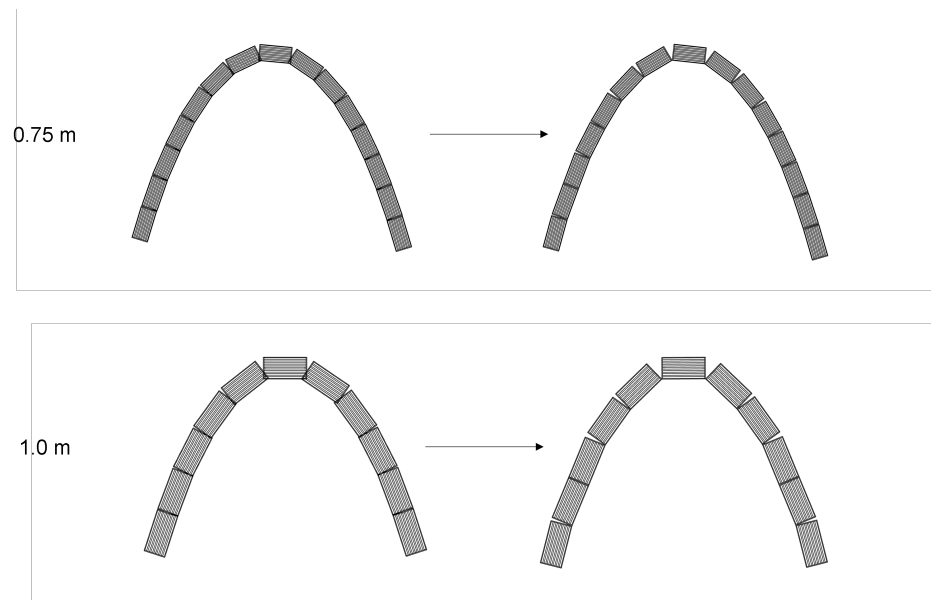


Figure 5.11: Problematic tessellation

The results shown in Figure 5.9 suggest that an inclination of 45° maximised the seismic performance of the vault, but further analysis was warranted to discount the viability of larger inclination angles. As such, additional angles of 50 , 55 , and 60° were studied, and the results were plotted together with previous pushover plots in Figure 5.12. Angles larger than 60° were shown to present issues with local component stability, so they were not considered. Figure 5.12 shows the expanded set of pushover curves for the optimal component width of 0.5 m, where angles from 25° - 45° are represented by a solid linetype that becomes darker for growing values of inclination. Angles from 50° - 60° are represented by dotted linetypes which become lighter for growing values of inclination. In this way, the gradient in line colour illustrates trends in stability evolution — an increasing trend is reflected by the plots becoming darker. The variations in linestyle were chosen to illustrate that a variation of inclination from 25° - 45° results in increasing stability performance, with a peak at 45° . For larger angles, stability tends to diminish with larger angles, so this decreasing trend is distinguished from the previous increasing trend by marking the corresponding plots with a dotted linestyle.

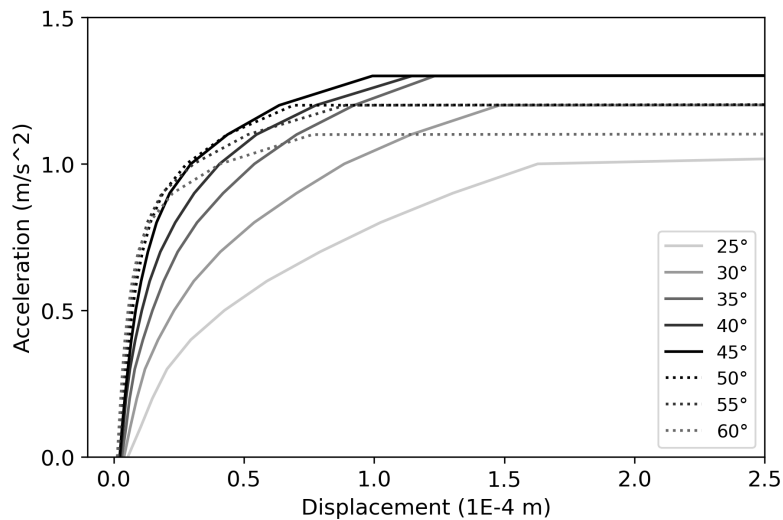


Figure 5.12: Variation of inclination for 0.5 m component width

5.3.1.2 Influence of thrust line shape

Assumptions for the thrust line shape were shown in Chapter 5.2.3 to have a potential influence on the pushover behaviour of the vaults being studied. Figure 5.13 presents a comparison of pushover curves for vault models with "real" and "ideal" thrust lines. In this figure, solid linetypes represent results for models defined by the "real" thrustlines, while dotted linetypes represent models corresponding to the "ideal" thrustlines. As shown in earlier results, the basic trend of positive correlation between stability and inclination is observed for both thrustline shapes. The increase in stability for increasing inclination is more pronounced in the results for the "real" thrustline models, however. This is observable in the larger difference between the maximum acceleration resisted for "real" thrustline models with inclinations of 25° and 30° versus the

"ideal" thrustline models for the same inclinations. Furthermore, the difference between "real" and "ideal" thrustline results for the same inclination decreases as the angle increases.

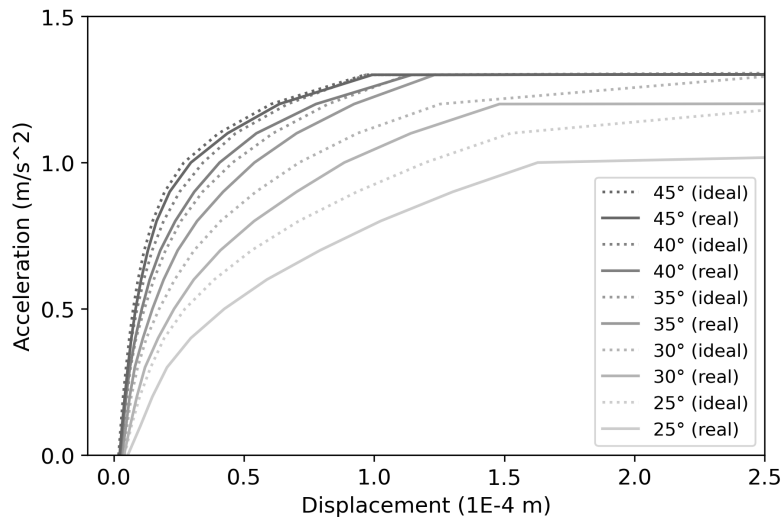


Figure 5.13: Comparison between thrust line shapes for a component width of 0.5 m and varying inclination

5.3.2 Staged analysis

The results of the staged analysis provide insight into how the vault's stability may evolve throughout the fabrication process. Figure 5.14 contains pushover plots for vaults composed of 1, 10, 50, 100, and 200 courses. As with previous pushover plots, the x-displacement of the outer gridpoint marked in Figure 5.8 is tracked for each model. Displacement and acceleration are plotted on the X and Y axes, respectively. Figure 5.14 demonstrates that stiffness and stability decrease as the number of courses increases. The 10 course model resists a maximum acceleration value of 1.3 m s^{-2} , which rapidly diminishes for the 50 course model. Afterwards, the change in stiffness and stability is more gradual between different numbers of courses.

5.4 Discussion

By comparing the pushover plots for each component width under different inclination angles, Figure 5.10 illustrates that stability tends to regularly increase as the inclination increases from 25° to 45° . This trend is clear for component widths of 0.25 m and 0.5 m but becomes obscured for larger widths. The pushover plots for these larger widths show limited consistency between results for different angles, which was hypothesised to be caused by issues with sliding between components in a given course. It was believed that for large widths, the stereotomy of voussoirs was problematic in some way that prevents their full kinematic stability mechanism from being engaged and results in premature failure. This explanation was discounted when considering the final model state of a vault with a component width of 0.5 m, as pictured in Figure 5.15, which is a contour plot of displacement in the X-direction with a deformation factor of 100. The model im

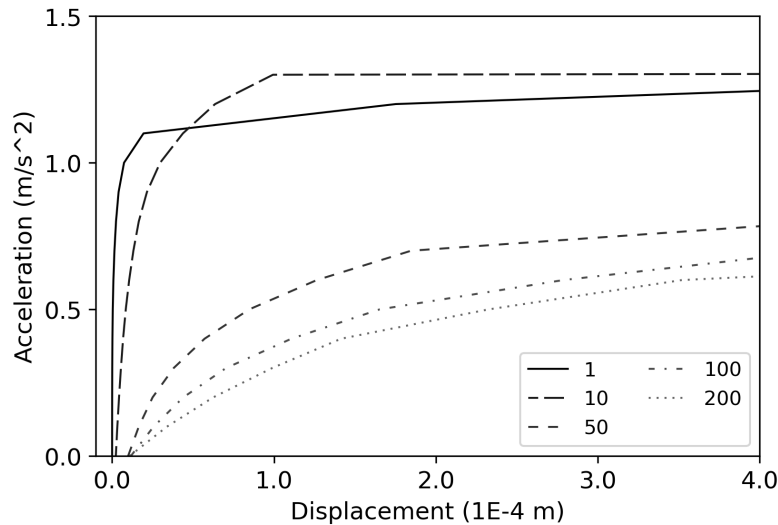


Figure 5.14: Variation of course number (realTL)

signs of in-plane sliding in this figure. Instead, it fails through a hinged mechanism in line with thrust line analysis theory, suggesting that some other mechanism was resulting in an unexpected onset of instability.

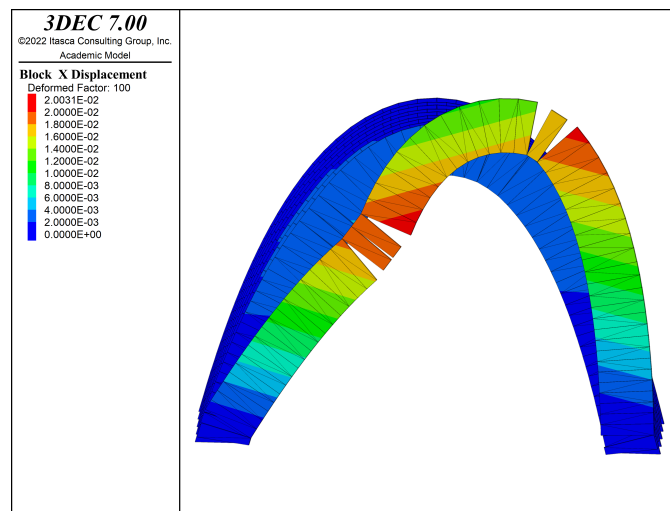


Figure 5.15: 1.5 m width, 45° inclination model; X-displacement contour plot

Furthermore, the hypothesis that premature instability was caused by joint sliding isolated exclusively in wide components would not explain why the peak acceleration for 35°, 40°, and 45° is approximately the same for 0.5 m, as in Figure 5.12. A closer look is taken into the model state for a component width of 0.5 m and 45° inclination in Figure 5.16. These two contour plots of displacement in the X-direction are defined with deformation factors of 50. The subfigure on the right shows a cross-section of the vault indicated in the left subfigure. Based on this cross-section, it is clear that a novel out-of-plane instability mechanism exists in this type of vault structure. This is evidenced by the slight out-of-plane overturning visible in the figure. This mechanism has a small influence compared to the in-plane stability mechanism based on the small out-of-plane displacements, but this mechanism still offers a compelling explanation for why many of the

pushover curves appear to exhibit a premature loss of stability.

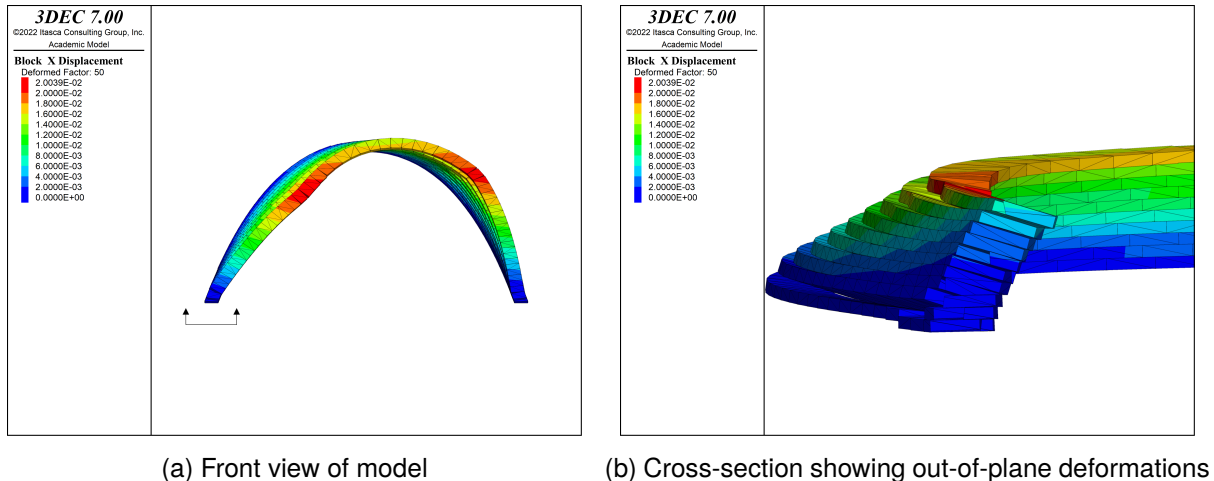


Figure 5.16: Final model state for 0.5 m component width and 45° inclination

Figure 5.10 illustrates how stability evolves based on variation of component width for any given value of inclination. Based on in-plane equilibrium considerations defined by thrust line analysis, one would expect a consistent increase in maximum acceleration with increasing component width. Although the results show a distinct and consistent increase in stiffness during early loading of each model, there are overlaps in the maximum acceleration resisted by several of the models. This is particularly evident in the results for inclinations of 25°, 30°, and 35°, where the widest components tends to reach the same maximum acceleration. These discrepancies can be explained by the out-of-plane instability mechanism, which was addressed previously. For inclinations of 40° and 45°, the premature loss of stability seems to be diminished based on the lesser degree of overlap between maximum acceleration levels for different component widths, but these results still support the justification to not consider components with a width of 0.75 m or larger for the design of the vault. Based on these results, stereotomy considerations illustrated in Figure 5.11, and expected manufacturing limitations, a component width of 0.5 m is chosen.

The parametric studies suggest that aside from a component width of 0.5 m, the most favourable vault configuration will have an inclination of 45°. In order to discount the use of larger values of inclination, angles of 50°, 55°, and 60° are studied for a vault with a component width of 0.5 m. Figure 5.12 illustrates that despite a slightly larger initial stiffness exhibited for the larger angles, an inclination of 45° shows the most desirable pushover behaviour. This figure does suggest that even for the 0.5 m wide components, there may be some degree of out-of-plane overturning which leads to a premature loss of stability. The plot corresponding to an inclination of 45° shares the same maximum acceleration as the 35° and 40° plots, despite exhibiting higher stiffness. As before, it is useful to refer to the model state to better understand the failure mechanism, which is shown in Figure 5.16.

Aside from studying the influence of primary geometric parameters such as inclination and component width, assumptions about the thrust line shape needed to be verified. As shown in Figure 5.7, the intersection of a plane with a funicular surface does not result in a catenary-shaped thrustline. Based on the theories of thrust

line analysis described in Chapter 2 and on the results of the parametric studies, it appears likely that the true flow of forces may not be defined by a funicular surface aligned with global coordinates. The difference between the "real" thrust line (defined by the plane intersection) and the "ideal" equivalent catenary shape becomes negligible as the inclination of the vault becomes vertical, but this difference could be significant for low angles of inclination. Therefore, the influence of this assumption was studied in order to determine whether adjustments to the modelling approach were needed. Figure 5.13 illustrates a trend that is expected based on the deviation between the two formulations of the thrust line shown in Figure 5.7. For an inclination of 25° , the thrust line formed by intersecting a globally-aligned funicular thrust surface shows significantly lower stiffness and stability than its equivalent catenary-shaped counterpart. This difference in performance diminishes with growing inclination, with the ideal thrust line exhibiting only slightly higher stiffness and negligible difference in maximum acceleration for an inclination of 45° .

The final set of analyses in this Analysis Phase correspond to a series of models that represent various construction stages in the construction of this type of vault. The decreasing stiffness and stability shown in Figure 5.14 is expected because the global stiffness of any structure with respect to lateral loading should decrease as its length increases. Figure 5.14 also shows that the proportionality of stiffness degradation to the number of courses diminishes at a certain point, with very little change in stiffness or stability between two models with 50 and 100 courses compared to 100 and 200 courses. What this indicates is in line with the loose-fit, discontinuous nature of the vault—the larger the vault is, the more the structural behaviour is governed by localised displacements rather than a global, elastic response.

By analysing a series of partial vault models with varying geometric parameters, this Analysis Phase has provided insight into the fundamental structural behaviour of dry-stone Nubian-type vaults. Aside from demonstrating how course inclination and component width influence stability, results from this Analysis Phase suggest that an interaction between kinematic stability within each course and friction between courses defines the overall stability of the structure. Significant research can still be done to more comprehensively understand the force-flow mechanisms which take place in this novel structure, but the analyses carried out thus far provide valuable preliminary insight into the structural behaviour of the dry-stone Nubian-type vault.

ANALYSIS PHASE II – ASSESSMENT OF SIMULATED VAULT GEOMETRY

6.1 Overview

The results of Analysis Phase I indicate what geometric parameters are appropriate for the final configuration of a Lunar habitat shielding vault in order to achieve optimal seismic performance. As such, the simulated vault models were designed to have an inclination of 45° and a component width of 0.5 m. Detailed considerations behind this choice of parameters is described in Chapter 5. A series of staged analyses are first carried out, which are analogous to those conducted in Chapter 5.3.2 of Analysis Phase I. A comparison of staged analyses between the first two Analysis Phases provides insight into how irregular tessellation and mechanical interlocking affect pushover behaviour of dry-stone inclined vaults. Afterwards, a final model is prepared based on the overall dimensions of the vault proposed by Konstantatou et al. (2022). This model is subjected to several quasi-static analyses, as well as dynamic time-history analysis. The main steps of this Analysis Phase are presented in Figure 6.1.

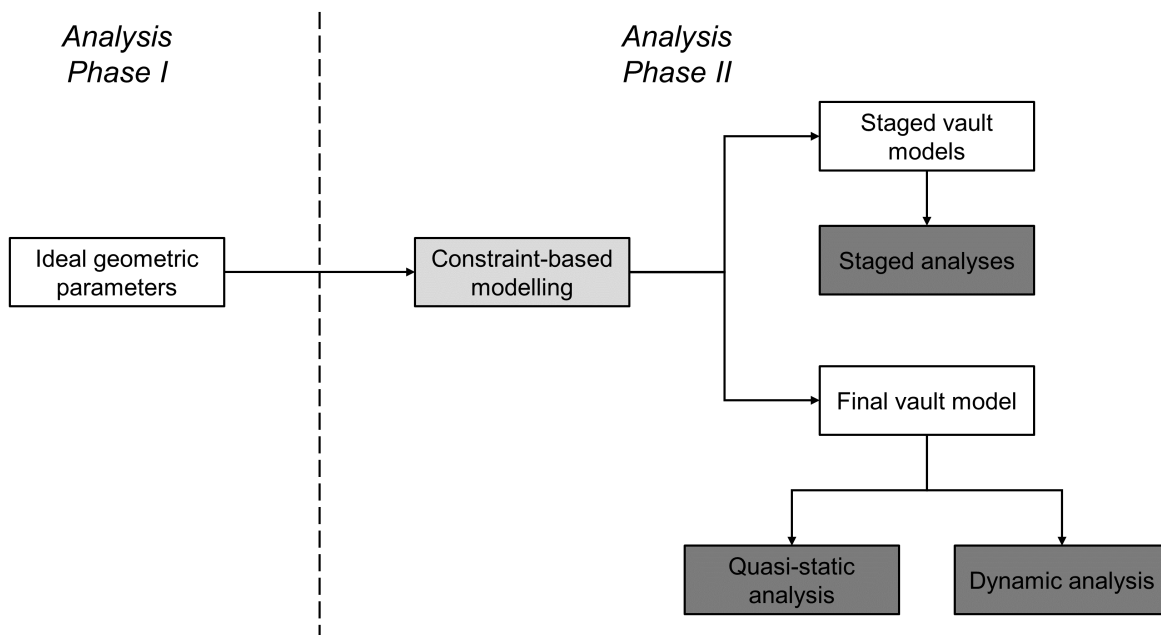


Figure 6.1: Analysis Phase II workflow

6.2 Methodology

6.2.1 Modelling

All models used in this Analysis Phase are composed of mechanically interlocking components. Clarification on how geometric constraint solving is used to simulate appropriate component placement in such models can be found in Chapter 3.

6.2.1.1 Staged models

For the staged quasi-static analyses, vaults with 10, 50, 100, and 200 courses were first modelled according to the parameters obtained in Analysis Phase I. These different model sizes represent several fabrication stages and are consistent with the stages examined in Analysis Phase I. The equivalence between these two sets of analyses allows for comparison between results for idealised and simulated component positions. The positioning of blocks in these models satisfies the constraints that are required to make such a vault viable, namely mechanical interlocking. Aside from varying the number of courses, it was considered useful to create analogous models where simplified components are used in place of the interlocking blocks in order to study the influence of irregular tessellation in isolation from mechanical interlocking effects. A comparison between the two component types is pictured in Figure 6.2. This figure demonstrates that the overall dimensions are the same between the two components, with the only difference being that the simple component does not have grooves or pins.

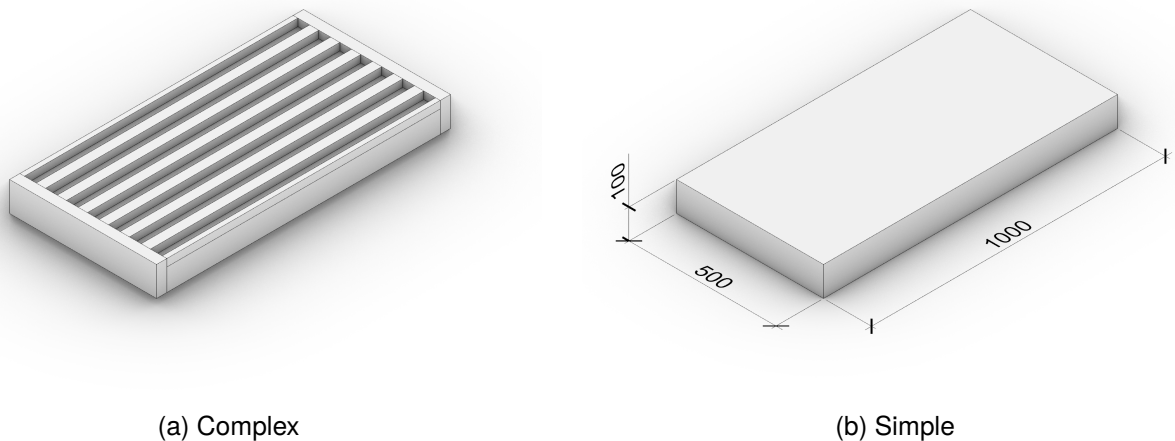


Figure 6.2: Component comparison (dimensions in mm)

The models with interlocking blocks are pictured in Figure 6.3, which also indicates which blocks are used to track displacements in the models. All analyses in this chapter report results for the gridpoint closest to the centroid of the outermost tracking block. Four models with interlocking blocks are created which correspond to different fabrication stages, as well as four duplicate models with simplified components. The positioning of blocks and the overall dimensions in the "simple" block models are identical to those in the interlocking block, or "complex," counterparts, but the use of simplified components results in models with far lower

computational demand. Aside from being useful for studying the influence of irregular tessellation without interlocking effects, simple component models were generated to lay the groundwork for Analysis Phase III, where numerous parametric material studies were to be carried out. It was not feasible to use models with complex blocks for these parametric studies due to prohibitively long solve times, so the simple component models served to serve as surrogates for the real vault with mechanical interlocking.

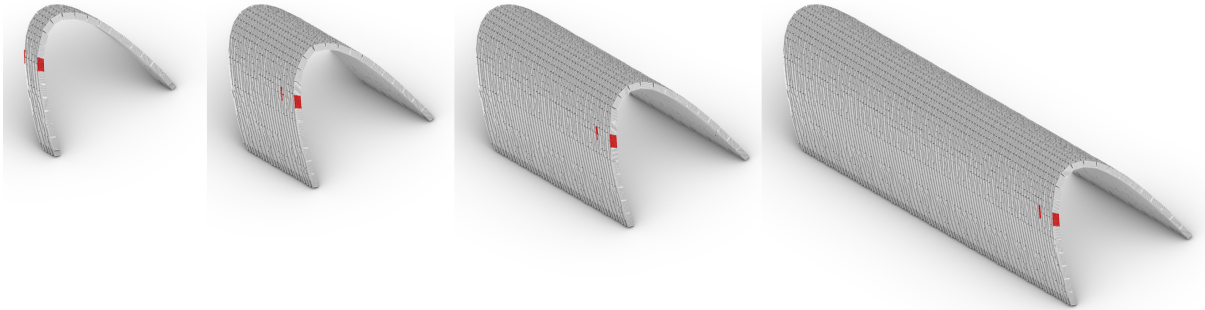


Figure 6.3: Gridpoint tracking for staged vault models

6.2.1.2 Final vault model

The final vault model was defined to have a total length of 24 m in order to match the dimensions of the vault proposed by Konstantatou et al. (2022). To reach this length, 170 courses were needed. The modelling approach does not differ from the fundamental modelling framework defined in Chapter 3, so no further commentary is warranted on details regarding model generation. An illustration of the final 3DEC model prior to analysis is provided in Figure 6.4. In this figure, the fixed support blocks are indicated in black, wedges are shown in red, and components have a white colour.

6.2.2 Staged quasi-static analysis

Quasi-static pushover-type analysis is first conducted on two sets of models: those assembled with interlocking, "complex" components and those with "simple" components used in place of the interlocking components. Each of these sets contains models with 10, 50, 100, and 200 courses. The pushover analyses for these models are set up in a manner consistent with the assumptions defined in the analysis framework in Chapter 4, so the details are not repeated here. One point that should be clarified is that the cutoff displacement definition is set to 0.02 m for the analyses where course count is varied based on the results of Analysis Phase I; previous results indicate that at this level of displacement, the vault is expected to have surpassed its initial equilibrium state and accrued permanent deformations. Additionally, the upper bound interface stiffness values are used in order to be consistent with the material definitions in Analysis Phase I. Research by Dell'Endice et al. (2021) also encounters uncertainties in joint spacing definition, but the matter is addressed by using the average between upper and lower bound stiffness.

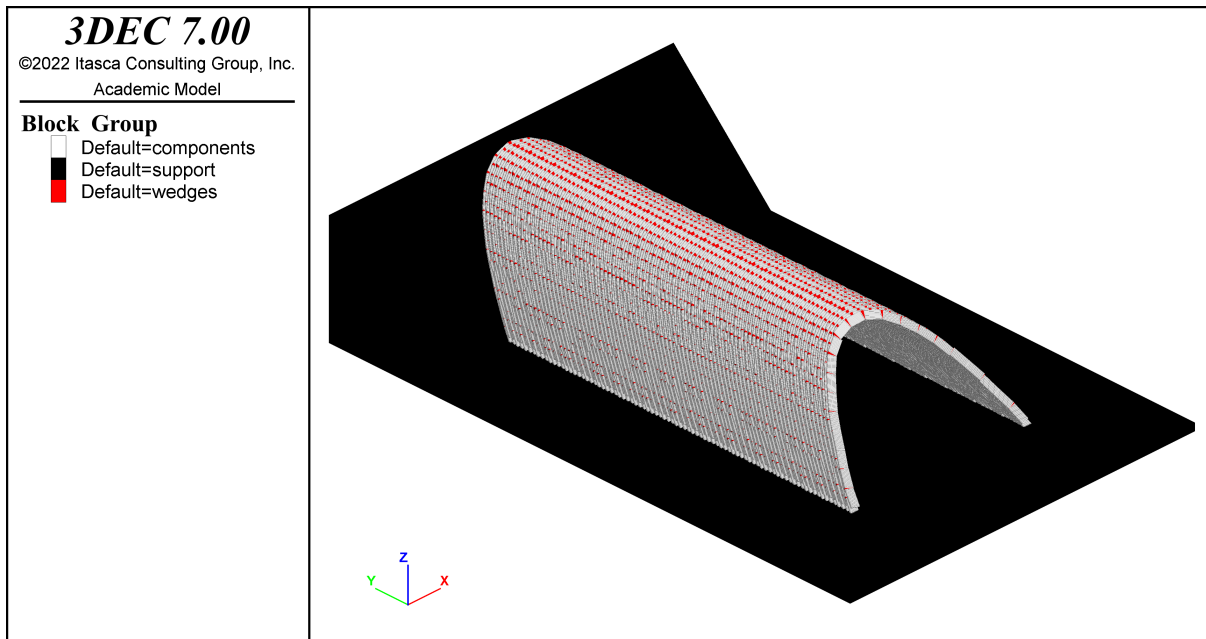


Figure 6.4: Final vault model in 3DEC

As in Analysis Phase I, the gridpoints used for tracking displacements in each of the models corresponded to points within blocks in the last course and tenth-to-last course. The blocks used for tracking displacement in this Analysis Phase were chosen to be approximately in the same position as those in Analysis Phase I in order to allow for comparison between the results. These blocks are highlighted in Figure 6.3.

Aside from studying the global evolution of stability, it may be important to consider the local stability of components in each course as it is being assembled. For an inclination of forty-five°, local instabilities during assembly are not a significant concern because the courses are not very steep. It is expected that the mechanical interlocking mechanism will prevent individual components from disconnecting from their modelled positions unless the inclination is so steep as to produce a large overturning moment from a given block's self-weight. Still, a simplified block-by-block analysis was conducted, which is shared in Appendix A. A more thorough analysis of the stability evolution after the addition of each block in a given course is out of the scope of this project due to the modelling complexity associated with this task, but may be important for future research.

6.2.3 Final quasi-static analyses

After the staged analyses were complete, the final vault model was subjected to several quasi-static pushover-type tests. In the interest of computational efficiency and to provide conservative results, the lower-bound interface stiffness was used from Table 4.1. This assumption was later varied in Analysis Phase III to illustrate how material parameters influence the performance of the final vault model. Other than the use of a lower bound stiffness value, the analysis approach was the same as the previous analyses, except a cutoff displacement of 0.03 m was used to study if there were any notable changes in behaviour for larger deformations. An unloading analysis was then conducted, where the lateral acceleration was incrementally

reduced from its maximum value to zero. Based on these initial analyses, it appeared that the vault had residual capacity for further lateral loading. Therefore, an extended pushover test was conducted where the design acceleration was rounded up to the nearest increment of 0.1 m s^{-2} and was applied to the vault to determine if it could satisfy the assumed seismic loading. It is important to mention that for the continued analysis, the final lateral acceleration of 1.6 m s^{-2} corresponding to the 475-year PGA was applied in one load step. This approach reduces the resolution of results because it doesn't provide data for intermediate load steps, but it is desirable because of increased computational efficiency. The main aim of this analysis was to study the state of the model when subjected to an acceleration that represents the design load case. Therefore, it is justifiable to forego the incremental pushover analysis in favour of the more efficient approach described. It is important to clarify that the actual design value for PGA based on Ruiz et al. (2022) is 1.52 m s^{-2} , which was rounded up to 1.6 m s^{-2} because the pushover script defined in Chapter 4 applies lateral acceleration in steps of 0.1 m s^{-2} .

6.2.4 Dynamic analyses

The extent of dynamic analysis in this project is limited in scope due to its prohibitive computational demand, but preliminary investigations of dynamic loading provide useful insight into the seismic performance of the final vault model. First, an eigenvalue analysis was carried out to determine the first six natural modes of vibration for the vault. Afterwards, dynamic time-history analysis was implemented. The application of time-history analysis to the final vault model is directly based on the methods outlined in Chapter 4, so no commentary about the configuration of these analyses is presented here. After the undamped time-history analysis is carried out for a ground motion in the direction of the vault span, the deformed model geometry is saved and allowed to settle under its self-weight. This settlement is studied in order to assess the stability of the vault after sustaining moonquake damage. In the interest of computational efficiency, it was deemed appropriate to use a static analysis for studying the post-moonquake stability of the vault. This choice is further justified by the fact that a truncated ground motion was used; if the applied velocity was abruptly fixed at the end of the truncated history, this could apply an unrealistic acceleration to the vault and confound the results.

6.3 Results

6.3.1 Staged analyses

The pushover behaviour of the vault assembled from simple components is shown in Figure 6.5. Results are presented for four representative stages of construction, corresponding to 10, 50, 100, and 200 courses. The plots are formatted in the same way as for Analysis Phase I, with the applied lateral acceleration and displacement plotted on the Y-axis and X-axis, respectively. The results illustrate that the stiffness decreases as the number of courses increases. Additionally, the maximum lateral acceleration reached before the onset of instability tends to be negatively correlated with the number of courses, although the differences in maximum acceleration are relatively small between the various models.

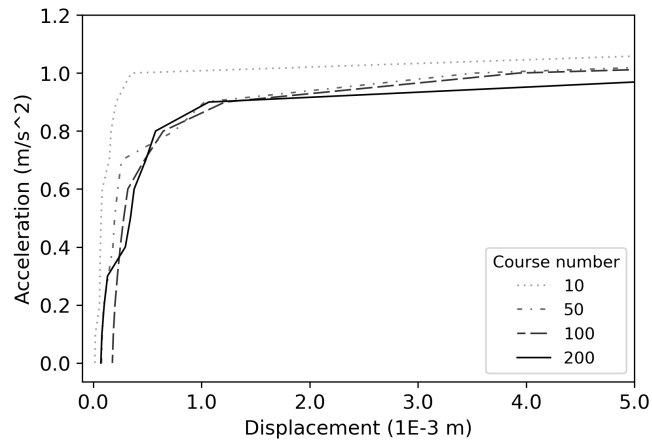


Figure 6.5: Course number variation for simple components

Similar to the staged analysis with simple components, pushover plots for complex component models with 10, 50, 100, and 200 courses are presented in Figure 6.6. As with the plots in Figure 6.5, there is a negative correlation between the number of courses and structural performance. The diminishing performance is evidenced by a reduction in stiffness and critical acceleration for growing course count. In this case, the onset of instability is not clearly defined by discontinuities in the pushover behaviour. Instead, a gradual degradation of stiffness is observed.

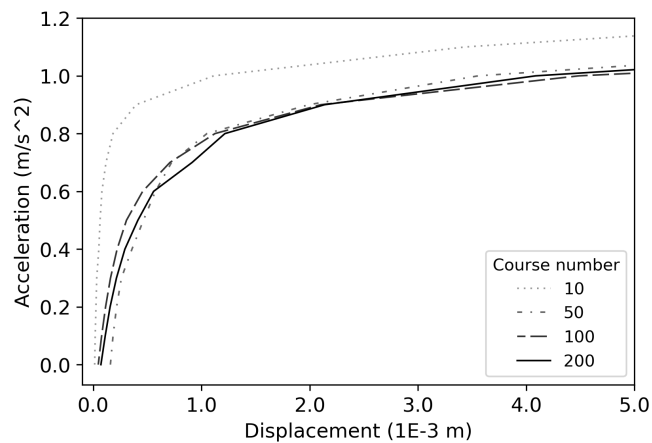


Figure 6.6: Course number variation for complex components

Figure 6.7 compares the pushover behaviour of the complex and simple models with the idealised models from Analysis Phase I. Each subplot in this figure represents a different construction stage. During each stage, the idealised model tends to demonstrate a slightly higher overall stiffness during initial loading. This is evidenced by the lower deformation observed at a given acceleration step. During later loading, however, the complex models tend to exhibit higher stiffness for all construction phases. Each model for the 10-course stage experiences a drastic decrease in stiffness at a critical value of acceleration. As the number of courses grows, the stiffness degradation generally becomes more gradual.

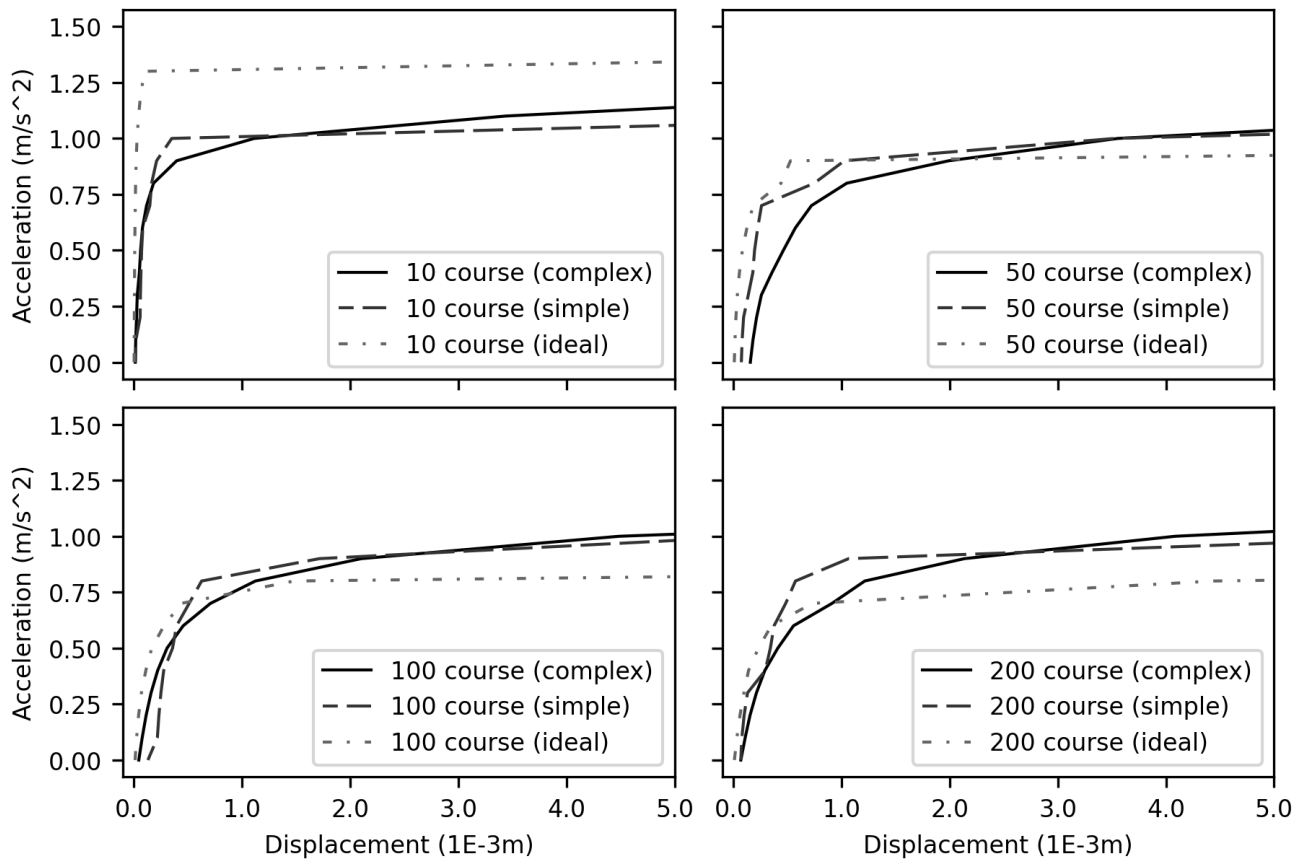


Figure 6.7: Comparison of complex, simple, and ideal component results

6.3.2 Analysis of final vault geometry

The final, full-scale vault model shown in Figure 6.4 was subjected to a pushover test, followed by an incremental removal of the lateral acceleration. As with the previous analyses, acceleration and displacement were plotted on the Y and X-axes, respectively. Once maximum displacement in the model reached 0.03 m, the loading scheme was reversed and the lateral acceleration was incrementally decreased to zero. This loading and unloading are reflected in the plot shown in Figure 6.8.

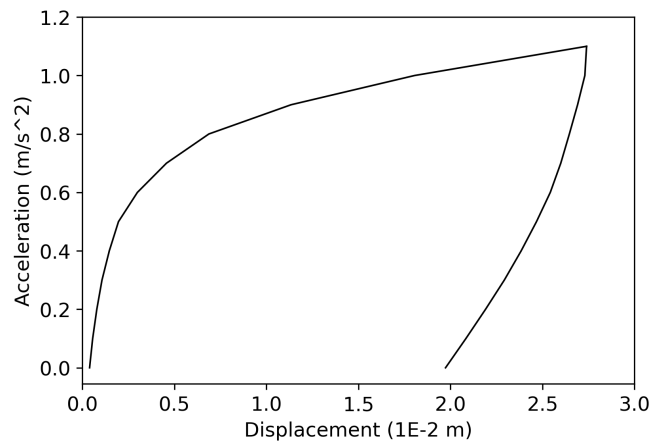


Figure 6.8: Demonstration of residual deformation present after unloading

Despite the large residual deformations present in the vault after unloading, the analysis reached equilibrium, proving that the vault was still stable under its new configuration. This motivated analysis under larger loading, suggesting that the vault may resist acceleration values larger than the 1.1 m s^{-2} reached during the first pushover analysis. The extended pushover analysis results are shown in Figure 6.9. As with the first analysis, the vault was unloaded after reaching equilibrium under the design acceleration. This unloading curve in Figure 6.9 shows the residual deformation in the vault after the design load was applied.

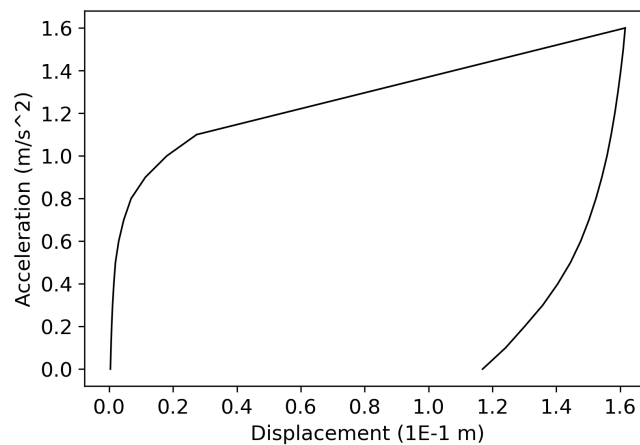


Figure 6.9: Extended loading and unloading

Figure 6.10 shows the velocity vectors of all blocks in the model after it reached equilibrium under an acceleration of 1.6 m s^{-2} . This figure provides evidence that the model satisfies the equilibrium condition defined in Chapter 4, which requires that the velocity components in X, Y, and Z are less than 0.001 m s^{-1} for all blocks in the model. The magnitude of the largest velocity vector is 0.0012 m s^{-1} , which indicates that the different components of velocity individually satisfy the equilibrium condition, but sum up to reach a slightly larger magnitude. This is not considered to be a concern because the magnitude is only slightly larger than 0.001 m s^{-1} .

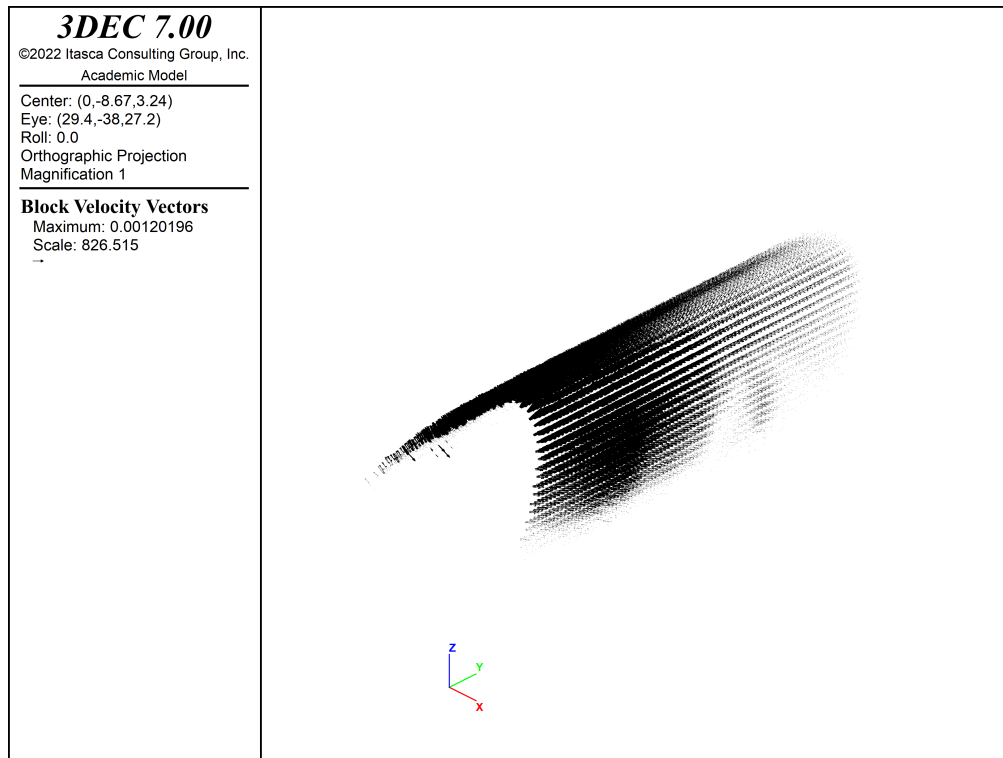


Figure 6.10: Velocity vectors showing convergence under design acceleration

6.3.3 Dynamic analysis

The first dynamic analysis carried out was an investigation of the natural modes of vibration of the full-scale vault model. The first six modes correspond to frequencies of 7.29 Hz, 8.73 Hz, 10.36 Hz, 10.88 Hz, 13.37 Hz, and 13.46 Hz, as shown in Table 6.1. The corresponding shape of each mode is illustrated in Figure 6.11. Most of the modes appear to be dominated by some type of lateral motion in the plane of the span, as shown in the figures for modes 1, 2, 4, 5, and 6. Modes 2, 3, and 5 also exhibit conspicuous out-of-plane, vertical deformations.

Mode (Hz)					
1	2	3	4	5	6
7.29	8.73	10.36	10.88	13.37	13.46

Table 6.1: Natural modes of final vault model

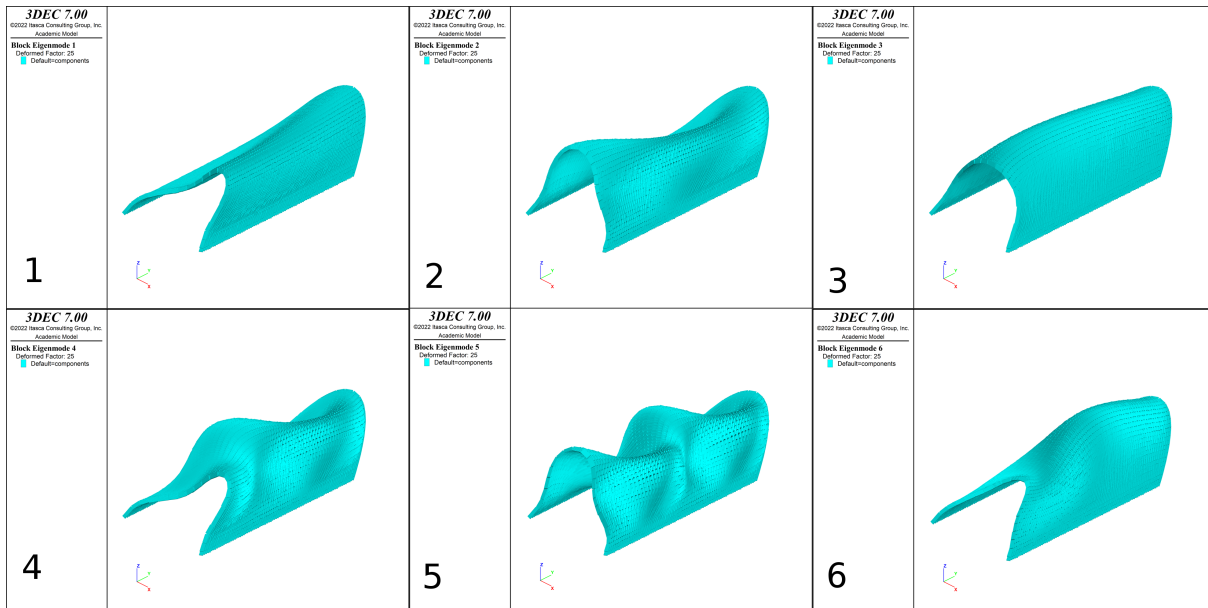


Figure 6.11: Natural modes of final vault model

The results of the time history analysis are presented in Figure 6.12, which shows how displacement in the X-direction evolves over time as a moonquake ground motion is applied. Two gridpoints are tracked, which correspond to the two blocks used for previous analyses. These tracking blocks are highlighted in Figure 6.3, which illustrates that for any given model, the tracking blocks are located in the outer course and the tenth course relative to the end of the vault. The response in Figure 6.12 is obtained by subtracting the displacement of the base block, which is being shaken, from the absolute displacement of the tracking points in order to get the relative displacement. As mentioned in Chapter 4, the input ground motion is truncated to produce a signal from 5-15 seconds which corresponds to the interval with the largest acceleration. Figure 6.12 shows that the displacement of the outer tracking block experiences a drastic increase soon after the 10-second mark. This corresponds to the outer courses of the vault exhibiting partial collapse, which is illustrated in Figure 6.13. In this figure, a semi-transparent overlay shows the original, undamaged vault

state. The displacement of the second gridpoint does not exhibit any irregular patterns and appears to follow the base motion with no significant dynamic amplification. This is consistent with Figure 6.13, which shows that only the first six courses collapse.

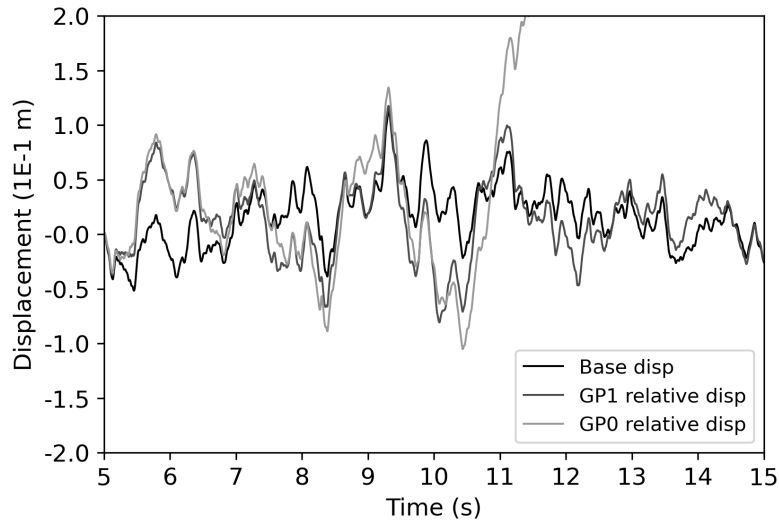


Figure 6.12: Time history of relative displacement

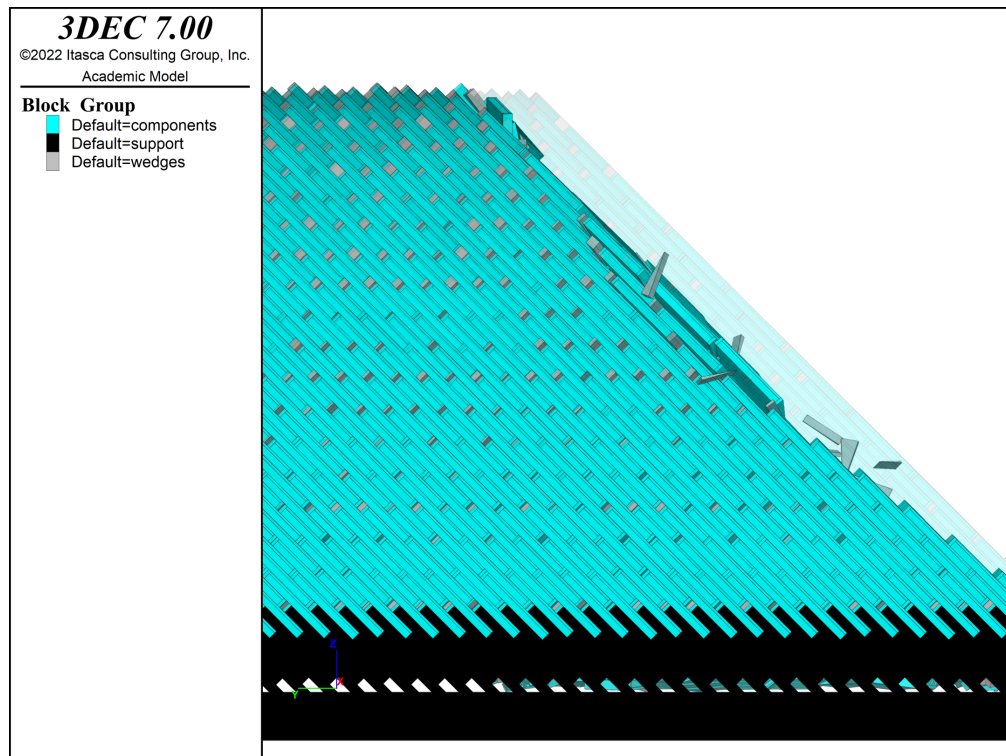


Figure 6.13: Damage due to moonquake

Figure 6.14 illustrates the equilibrium state of the vault after settling from moonquake-imposed deformations. In this figure, red colouring indicates blocks with a velocity larger than 0.0001 m s^{-1} , which is one-tenth the magnitude of the equilibrium criterion. This smaller value was used in order to exaggerate the point that the

vault is in equilibrium. It is evident that although some blocks from the collapsed outer courses are in motion as they travel towards the ground, the remaining parts of the vault are stable.

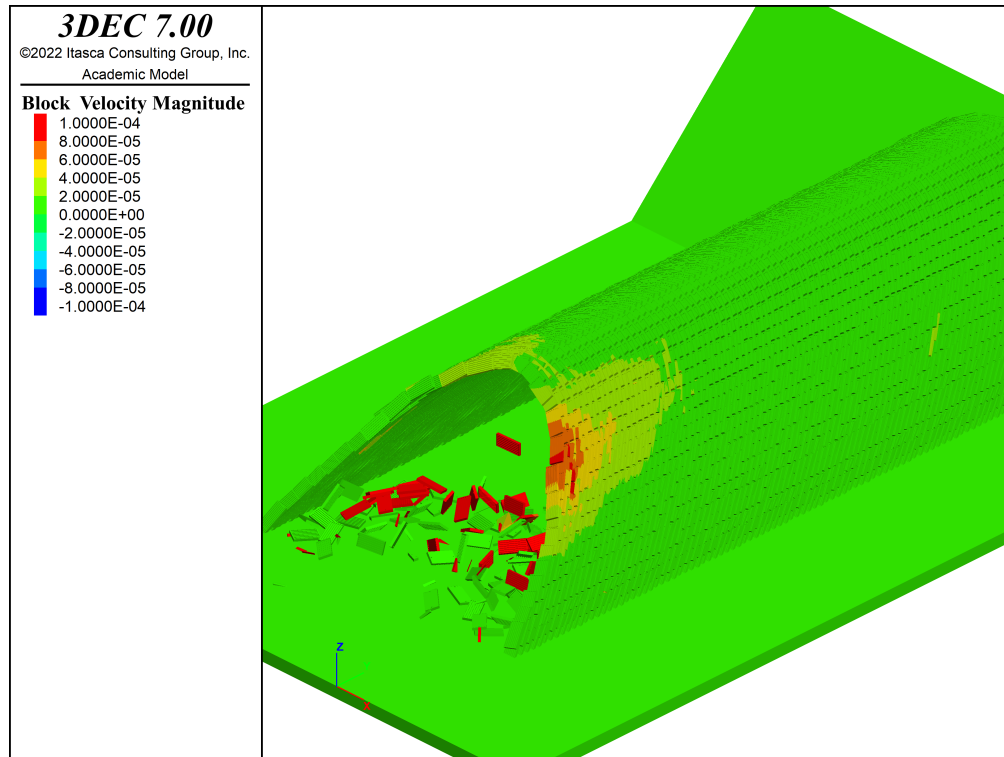


Figure 6.14: Post-moonquake stability

6.4 Discussion

Based on the results of Analysis Phase I, parameters were chosen to define the final vault geometry, which was used to define models assembled through geometric constraint solving. Analyses were first conducted on simulated models assembled from simple components at four construction stages, as shown in Figure 6.5. As was the case for staged analyses in Analysis Phase I, these vaults exhibit diminishing stiffness and stability with a growing number of courses. It is interesting to note that the pushover behaviour does not appear to vary as much between different model sizes for the simulated vault geometry compared to the results for idealised models in Figure 5.14.

Analogous models with interlocking components were subsequently analysed, the results of which are shown in Figure 6.6. This figure also shows a tendency for the models to decrease in stability with a growing number of courses, although the degradation of stiffness is more significant. These two sets of results were compared with the staged analysis results from Analysis Phase I to provide insight into the influence of irregular tessellation and mechanical interlocking in dry-stone Nubian-type vaults. The resulting comparison is shown in Figure 6.7, which indicates that the vaults are expected to exhibit relatively similar pushover behaviour. The irregular tessellation is not shown to significantly decrease stability. Mechanical interlocking is shown to reduce the abruptness of stiffness degradation, which can be explained by the efficient redis-

tribution of shear stresses brought about by force transfer through the pins. In this way, the interlocking behaviour causes the vault to behave more like a singular system rather than as disparate components.

Aside from the staged analyses, the second set of investigations conducted in this Analysis Phase relate to analysing the final vault model, which is consistent with the 24 m length defined in research by Konstantatou et al. (2022). These investigations consist of several quasi-static and dynamic analyses. The results of the first quasi-static analysis carried out with this final model are presented in Figure 6.8. This pushover plot shows the same gradual degradation of stiffness observed in the staged analysis of vaults with complex components. Again, unlike conventional instability mechanisms in masonry, there is no apparent critical onset of instability observed in the pushover plot of the final vault model. There appears to be an approximately elastic domain of loading up until an acceleration of 0.5 m s^{-2} , after which the stiffness degrades slightly with each load step, but there is no sudden decrease in stiffness otherwise seen in the pushover behaviour of arches, for example.

In order to better understand the state of the model after the loading shown in Figure 6.8, a quasi-static unloading was performed. This unloading analysis indicated that the vault was, in fact, stable after being loaded, despite also exhibiting a significant residual lateral deformation of nearly 0.02 m. These results indicated that the vault could be loaded with a larger lateral acceleration before experiencing instability. Therefore, an extended pushover analysis was conducted using an acceleration representative of the design acceleration. The resulting pushover plot from the extended analysis and subsequent unloading is shown in Figure 6.9. It is important to note that this acceleration was applied to the previously loaded model in one step rather than in increments of 0.1 m s^{-2} , as explained in Chapter 4. This explains the linear nature of the pushover curve between g_x , which in reality would exhibit gradual degradation of stiffness between each load step. In order to ensure that the model is indeed at equilibrium under the design acceleration, a plot of velocity vectors is shown in Figure 6.10. The maximum magnitude of velocity is 0.0012, which satisfies the convergence criteria described in the analysis framework in Chapter 4. These results provide an indication that the vault can resist the design PGA for a 475-year moonquake defined by Ruiz et al. (2022). Applying the PGA as an equivalent static lateral acceleration is likely to be conservative, but dynamic analysis is still necessary to better understand the true seismic performance of this structure.

The first six modes of vibration of the final vault structure are summarised in Table 6.1 and the corresponding model states are depicted in Figure 6.11. By comparing the eigenmode analysis results with the UHS by Ruiz et al. (2022) shown in Figure 2.7, one might expect significant dynamic amplification since the highest amplitude in the response spectrum is correlated with a frequency close to the first natural mode of the discrete vault, which is 7.29 Hz. Such amplification is not seen in the time-history response shown in Figure 6.12, where the amplitude of displacement for both gridpoints is not significantly larger than the base displacement throughout the application of ground motion. There is a clear exception for GP0 just after the ten-second mark, however. This lack of amplification can be explained by the fact that the eigenmodes are calculated for an elastic system, so the influence of joint sliding is not accounted for. In reality, the system only behaves elastically for low levels of loading. This means that in the dynamic analysis, inelastic

deformations occur throughout the vault whenever cohesive frictional forces are overcome. The effect of joint sliding in the time-history analysis allows for energy dissipation, which prevents dynamic amplification.

The time history response in Figure 6.12, shows a rapid change in displacement for GP0, but this is not attributed to dynamic amplification. Rather, what appears to have occurred is that the shaking of the blocks allowed for wedges in the unconfined outer course, which is the location of GP0, to fall out and compromise the structural integrity of this course. Without continuity within the course due to the absence of the wedges, any given component in the course is only held in place by friction and loose mechanical interlocking, which gradually leads to complete separation of the components from the larger vault. This process results in new courses becoming unconfined and thus less stable due to the lower friction, which again causes these outer blocks to fall away from the vault. It is important to note that the use of zero damping for this analysis is a conservative approach, so it is not clear whether the evolution of damage due to separation of outer courses can be expected for a real structure. It is possible that damping may prevent the mechanism that allows for blocks in the outer courses to become disengaged from the rest of the vault. The absence of damping may result in unrealistic block vibrations, where the block's pins may bounce back and forth within the grooves of the component below. In any case, the model state after the moonquake exhibits partial collapse in the outer six courses, as evidenced by Figure 6.13. Despite the collapse of the outermost courses corresponding to less than 4% of the vault, Figure 6.14 illustrates that the remaining parts of the vault are still stable, with blocks satisfying convergence criteria for equilibrium under gravity loading. These results are significant because they show that despite the tendency for the outer, unconfined courses to collapse, the vault performs quite well in response to the design moonquake. The local collapse that takes place may readily be mitigated by some type of external intervention, such as composite reinforcement, which has precedent in strengthening masonry structures (Gaetani et al., 2017; Michiels et al., 2019). Additionally, it is possible to conceptualise some type of adhesive bonding or welding between components in the outer courses to join them together.

ANALYSIS PHASE III - MATERIAL SENSITIVITY STUDIES

7.1 Overview

Several sources reviewed in Chapter 2 illustrate the value of conducting material sensitivity studies for masonry structures, especially in cases where material properties show significant uncertainty or variation (Gonen et al., 2021; Lemos, 2019). Therefore, this Analysis Phase was considered necessary in order to develop an understanding of possible variations in the structural behaviour of the vault. Key material properties for the bricks were varied, and the models were subjected to a series of quasi-static pushover-type analyses. Additionally, a separate set of analyses was conducted which studies the effect of varying material properties for the wedges, while maintaining a uniform material definition for the components. The progression of different design steps leading to this Analysis Phase, as well as the general structure of the sensitivity studies, is illustrated in Figure 7.1.

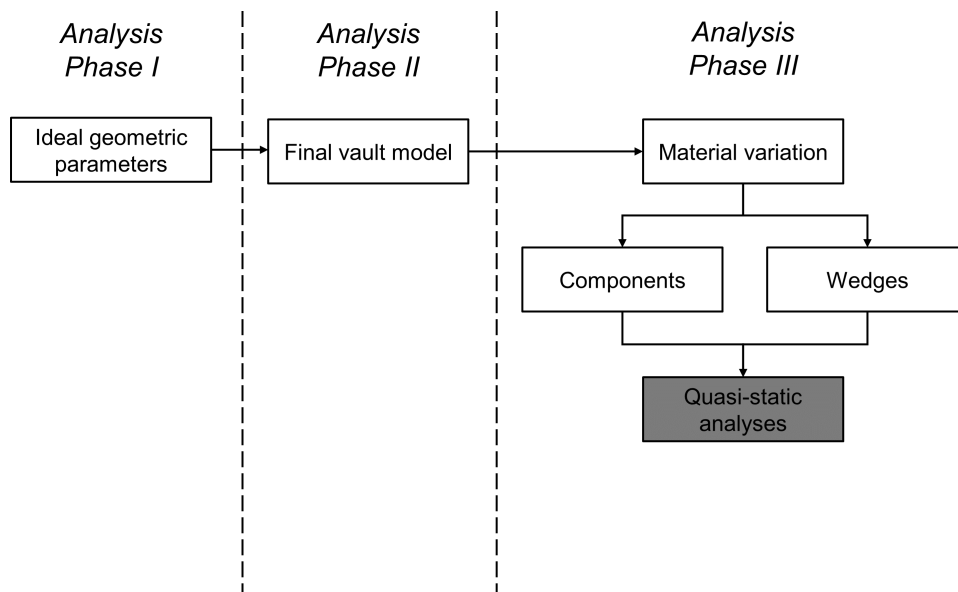


Figure 7.1: Analysis Phase III workflow diagram

7.2 Methodology

7.2.1 Establishing equivalence between simple and complex component vaults

As mentioned in the previous section, conducting repeated analyses on the full-scale vault geometry with "complex" components was deemed to be too computationally-demanding for this project. It was hypothesised, however, that the material definition of the "simple" component models could be adjusted in a way that results in similar early pushover behaviour compared to the real vault. This was considered possible because for early loading of the "complex" component models, the structural behaviour appeared to be governed by friction, with limited engagement of the interlocking mechanism. This is evidenced by the comparison between simple and complex component results in the Discussion section of Chapter 6, where it was shown that there exists an approximately-elastic region of the pushover plots where both vault model variants are primarily held together by friction. As discussed previously, the pushover behaviour of the simple and complex models should be nearly identical in this region, but varies due to differences in subcontact generation.

As such, initial attempts at matching the pushover behaviour of the models with different components were based on variation of the number of subcontacts through changes in the definition of minimum edge length. This approach proved to be too computationally expensive for use in the sensitivity studies despite achieving a favourable match in the pushover behaviour of the two vault variants. The results of matching pushover behaviour through variation of subcontact generation are included in Appendix A. Since the effect of changing the number of subcontacts essentially changes the overall stiffness of a given block, it appeared that varying the interface stiffness definition could result in an appropriate match between global pushover behaviour of the two vault variants. This approach was studied by conducting several quasi-static analyses with varying reductions in interface stiffness, as shown in Figure 7.2.

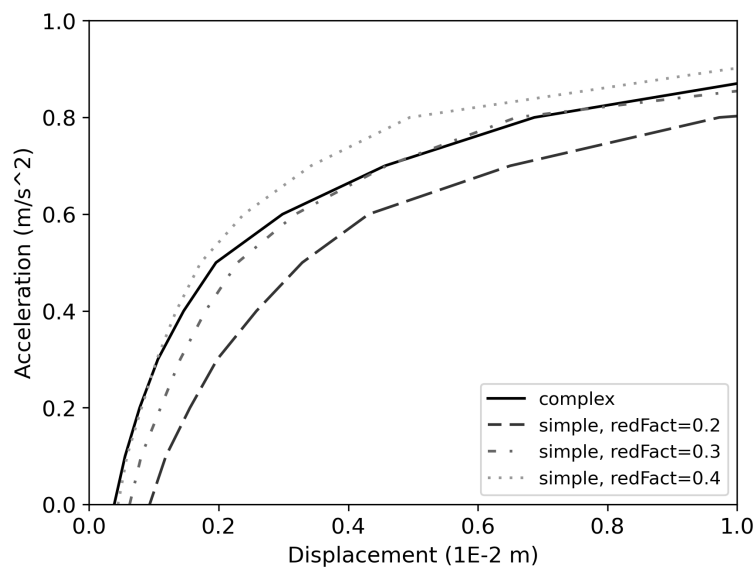
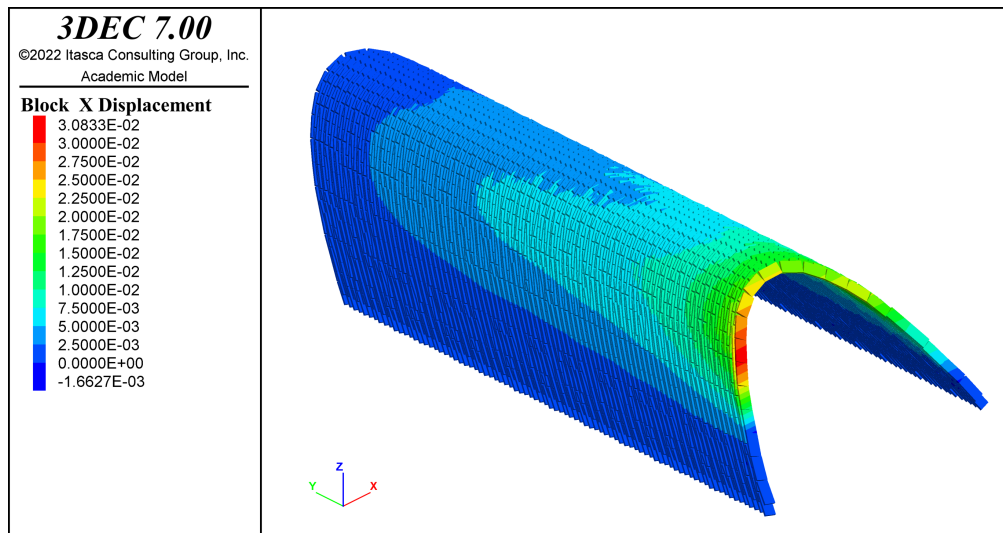
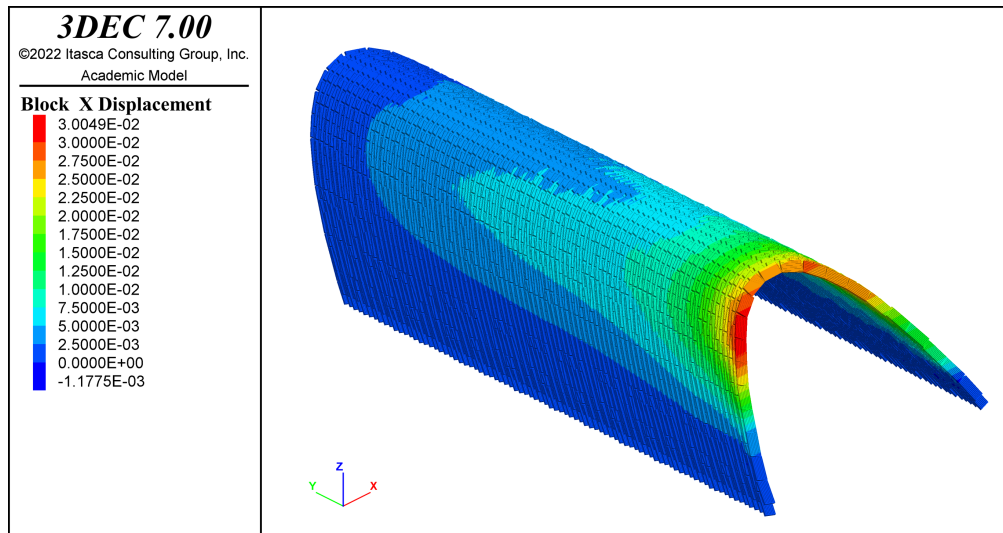


Figure 7.2: Matching pushover curves

The reduction factors indicated in this plot are multiplied by the normal and shear interface stiffness values to obtain softened interface properties. According to Figure 7.2, an appropriate reduction in stiffness can be achieved through multiplication of the original stiffness parameters by a factor of 0.3. Figure 7.3 shows X-displacement contour plots for simple component vaults with softened interface properties and for the complex component model. This figure shows how the distribution of displacements is similar between the two component assumptions, providing further evidence that the simple component model with these "tuned" interface parameters can be used to approximate early-stage loading of the real vault model.



(a) "Tuned" simple component model



(b) Complex component model

Figure 7.3: Contour plots of displacement in X-direction

From these results, it can be seen that the simple component vault behaves similarly to the real vault for a stiffness reduction factor of 0.3, which results in interface stiffness values of $k_n = 2.51\text{E}+03$ and $k_s = 9.90\text{E}+02$. As such, it is assumed that simple components with these interface parameters behave approximately like complex components during early loading. This assumption is taken as the starting point for the

sensitivity studies carried out in this section, as it is assumed that the modified simple component model provides a suitable approximation of the real vault model. Table 7.1 provides a summary of the interface properties that are used with simple components to approximate the behaviour of complex components

Component type	k_n (MPa/m)	k_s (MPa/m)	ϕ (deg)
Complex	8.36E+03	3.30E+03	40
Simple	2.51E+03	9.90E+02	40

Table 7.1: Comparison between properties of equivalent simple components and complex components

7.2.2 Material property variation

In the first set of material sensitivity studies, interfaces between all blocks are assumed to have the same properties, which is consistent with assumptions outlined in Chapter 4. The interfaces are not expected to exhibit significant cohesion or tensile strength due to the mortarless nature of the vault, which leads to an investigation of the influence of interface stiffness and friction angle.

As mentioned in Chapter 3, it was assumed that gaps between components can be filled with raw, in-situ materials, whose properties are difficult to confidently predict. Therefore, material variation for these elements should be studied in isolation from assumed component properties. The most likely material used for these wedges would be a fill of loose rocks, bulk regolith, or a combination of the two. These materials would have low cohesion and near-zero tensile strength, so the only remaining material properties that are reasonable to defined in the Mohr-Coulomb joint model are stiffness and friction angle. Therefore, these are the material properties varied for the wedge definition in this Analysis Phase.

Friction angles of 20°, 30°, 40°, and 50° are studied based on possible variations expected in dry-stone masonry and loose regolith (Heiken et al., 1992; Marino et al., 2014). Interface normal and shear stiffnesses are defined based on the sintered regolith's elastic and shear moduli divided by some factor. In the case of the components, the factor in the denominator is meant to represent the distance between block centroids, as explained in Chapter 4. For wedges, this factor has less of a physical significance and is only meant to illustrate different orders of magnitude for the stiffness definition.

7.3 Results

Figure 7.4 illustrates the pushover behaviour of the final vault model for several analyses where the friction angle of all the interfaces is varied. Each plot exhibits an approximately constant slope during early loading, after which a critical value of lateral acceleration results in a sudden decrease in stiffness. The initial stiffness of each plot is similar, but the acceleration at which the stiffness begins to degrade significantly is positively correlated with friction angle. The shape of each pushover plot is relatively smooth, indicating regular decreases in stiffness with each load step after the initial elasticity is overcome. There are some exceptions for a friction angle of 50°, however, which exhibits increases in stiffness between acceleration

values of 0.7 and 0.9 m s^{-2} and between 1.0 and 1.1 m s^{-2} . Additionally, the displacement under self-weight is negatively correlated with friction angle. The displacement at a lateral acceleration of 0.0 m s^{-2} changes slightly between a friction angle of 50° and 40° , but grows significantly for lower friction angles.

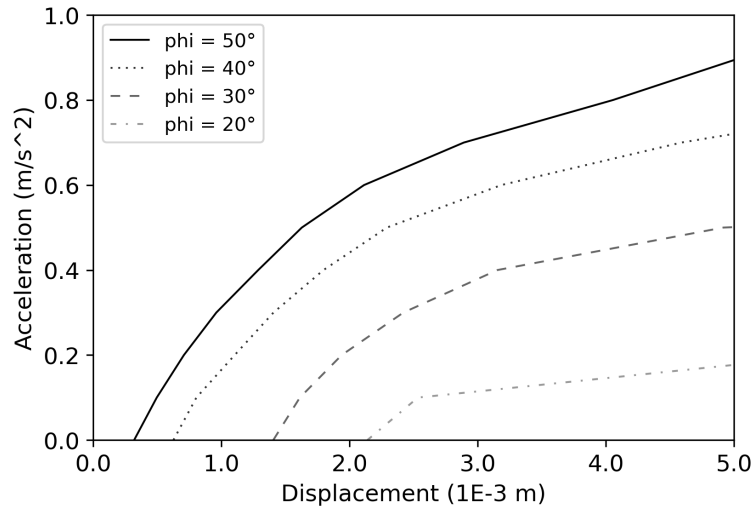


Figure 7.4: Component friction angle variation

Figure 7.5 shows the results of the interface stiffness sensitivity study, where pushover plots are shown for the upper and lower bound interface stiffness values defined in Chapter 4, as well as an intermediate value. The initial slope of each plot is relatively constant until a critical value of lateral acceleration is reached, after which point the stiffness rapidly degrades with increasing acceleration. As interface stiffness decreases, the initial slope decreases. For later stages of loading, the slope of each plot becomes similar, though the peak acceleration is positively correlated with interface stiffness. This effect is evident for $k_n = \frac{E}{1.0}$, which shows a significantly lower peak acceleration, but is not so clear for the other stiffness values due to some degree of overlap between their plots.

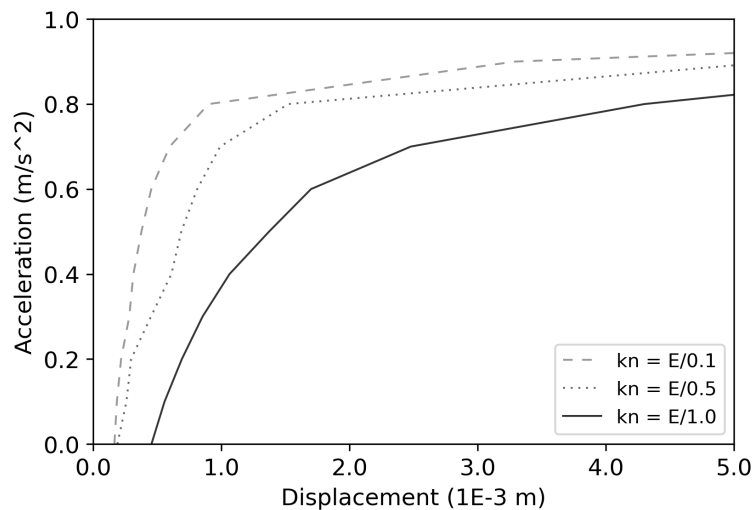


Figure 7.5: Component interface stiffness variation

Figure 7.6 shows the results of the sensitivity study of friction angle for wedge interfaces. There is remarkably little variation in the pushover behaviour for different friction angles. At the end of the displacement domain, the acceleration for a friction angle of 20° appears to be slightly lower than the other results, which are hardly distinguishable from each other.

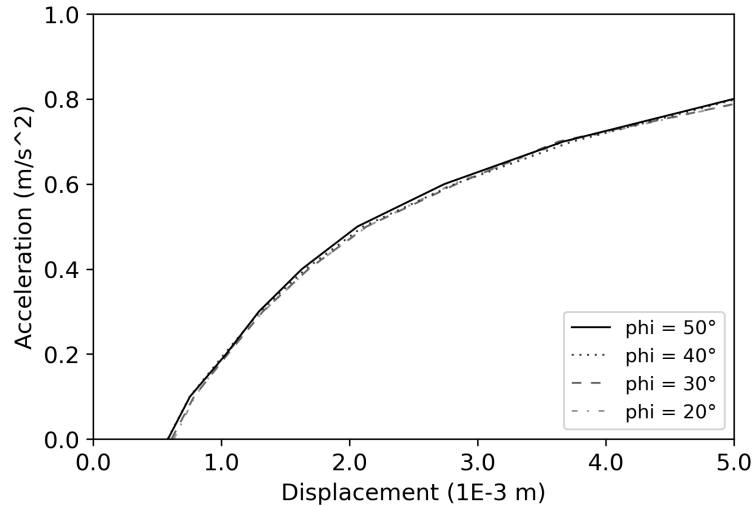


Figure 7.6: Wedge friction angle variation

Figure 7.7 shows the results of the sensitivity study of normal and shear stiffness for wedge interfaces. This plot illustrates that the overall stiffness of the vault is positively correlated with the interface stiffness. Results for zero stiffness were simulated by removing the wedges from the model entirely. It is important to note that the results for zero stiffness do not fit the trend, as the stiffness initially appears to be higher for this case than for $k_n = \frac{E}{1000}$. At an acceleration value of 0.5 m s^{-2} , there is a discontinuity in the pushover plot for $k_n = 0$ which results in a sharp decline in stiffness.

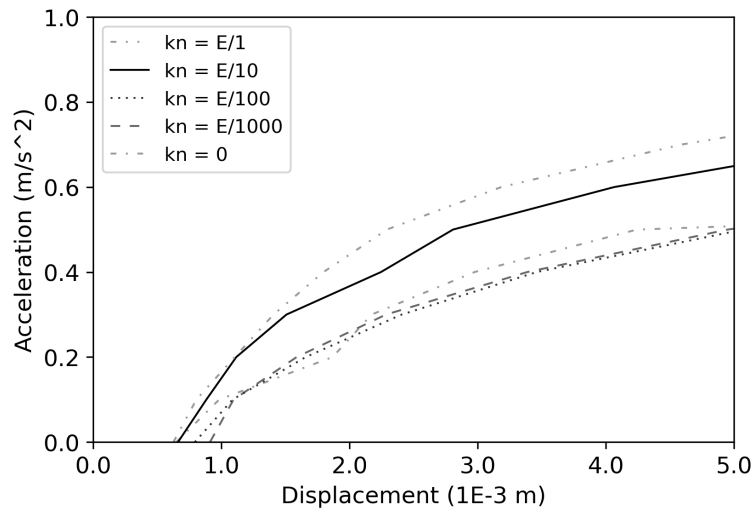


Figure 7.7: Wedge interface stiffness variation

7.4 Discussion

Friction angle of the component interfaces was shown to have a significant influence on the stability of the final vault geometry. Interestingly, Figure 7.4 shows that the pushover curves for each friction angle have remarkably similar slopes during the first few acceleration steps after initial settlement under gravity, where the response is approximately elastic. After this elastic region, each pushover curve exhibits a gradual degradation of stiffness with each load step. The critical acceleration increases with increasing friction angle. The observation of similar stiffness during early loading for each of the friction angles is expected. The interface stiffness is the same for each of the models in this case and since the models are geometrically identical, the global stiffness of each vault is the same. Therefore, the friction angle should only affect the shear stress at which joints begin to slip, with larger friction angles resulting in a larger resistance, as shown in Figure 7.8. Although precise determination of the friction angle of sintered regolith components requires laboratory testing, the components can be expected to have a friction angle ranging from around 30° to 40° based on values for stone masonry according to Marino et al. (2014). Figure 7.4 shows that this range of variation results in a difference of over 30% in the maximum acceleration resisted by the vault.

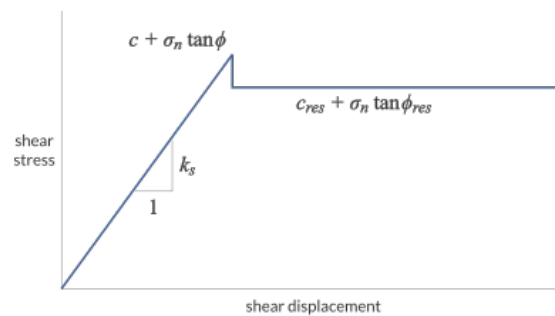


Figure 7.8: Influence of friction angle in Mohr-Coulomb joint model (Itasca Consulting Group Inc., 2019)

Regarding the influence of interface stiffness variation shown in Figure 7.5, there is a clear correlation between larger interface stiffness and larger global stiffness of the vault, as evidenced by steeper slopes during early loading in the pushover plots. The apparent onset of significant plastic deformation is about 25% lower for the lower bound interface stiffness, while the difference between peak acceleration for the lower bound stiffness and the intermediate stiffness is negligible, with both experiencing a significant kink at an acceleration of 0.8 m s^{-2} . This suggests that there may be an upper limit at which the blocks experience virtually no interpenetration between contacts and behave in a perfectly rigid manner; further increasing interface stiffness is not expected to significantly affect the stability of the vault.

Although the wedge and component interface properties were assumed to be the same during previous analyses, this assumption is unlikely to hold for the actual construction of a vault such as the one studied in this project. This is because it is expected to be infeasible to create custom-fit wedges out of sintered regolith. Although such an approach may be possible, it would be preferable to follow a more flexible approach. As mentioned in Chapter 3.4.1, it may be possible to enforce continuity of each course through the using of infill material such as packed regolith or small stones. With such an approach comes a significant amount of

uncertainty due to potential variation in the mechanical properties of the infill. The influence of friction angle of the wedge interface was shown to be negligible, with little variation in the pushover behaviour for different friction angles in Figure 7.6. This can be expected because the wedges primarily experience in-plane normal stresses through their role in maintaining continuous compressive load paths within each course. For this reason, varying interface stiffness, particularly in the normal direction, is expected to have a significant effect on stability. This is supported by the plots shown in Figure 7.7, which demonstrate significant variation in the pushover behaviour of vaults with different values for wedge interface stiffness.

COMPARATIVE ANALYSIS I - EQUIVALENT MONOLITHIC VAULT

8.1 Overview

Although the main aim of this project is to study the seismic performance of a discretely-assembled masonry vault, it is valuable to conduct a comparative analysis of an analogous structure which may be fabricated using AM. As mentioned in the literature review, AM approaches to extraterrestrial design have drawn more attention in literature compared to component-based alternatives. By comparing the pushover behaviour of the component-based and monolithic vaults, important insights can be gained about which approach may be more suitable for the construction of extraterrestrial infrastructure.

8.2 Methodology

8.2.1 Geometric modelling

The final vault geometry from Analysis Phase II was used as the basis for modelling an equivalent monolithic vault. The two models are defined to have the same rise, span, and length, but the definition of thickness requires further consideration. There are clear differences in the type of geometry that is expected to be fabricated using AM compared to discrete assembly, so there is a degree of uncertainty with regard to what can be considered an "equivalent" thickness for the monolithic vault. Given the larger degree of geometric complexity achievable with AM, it is unlikely that a monolithic vault with a constant thickness would be designed. With AM, arches or vaults with varying thickness can be fabricated in order to optimise material usage, as was proposed by (Málaga-Chuquitaype et al., 2022). In this project, however, it is considered appropriate for the equivalent thickness to be uniformly defined based on the component width defined in Chapter 6.2.3, which will result in a monolithic vault that utilises approximately the same volume of structural material as the component-based analogue. This will provide insight into the relative material efficiency between discrete assembly and AM in the construction of a vault. The overhang between consecutive courses in the component-based model is ignored and the thickness of the equivalent monolithic vault is defined as 0.5 m. To generate an equivalent monolithic vault, an idealised cross-section of the component-based vault is first modelled, as shown in Figure 8.1. This surface is obtained by symmetrically offsetting a typical course path obtained in Chapter 3 and then lofting the resulting curves. The value of offset is equal to half of the block width, which results in a surface with a uniform width equivalent to that of the governing component geometry. Next, the surface is truncated to reflect the fixed condition of blocks in Figure 4.1. This is done because the "effective" vault geometry consists of blocks that are free to move, which correspond to those above the plane illustrated in Figure 8.1. Finally, this truncated surface is extruded by the length of the vault, which is 24 m.

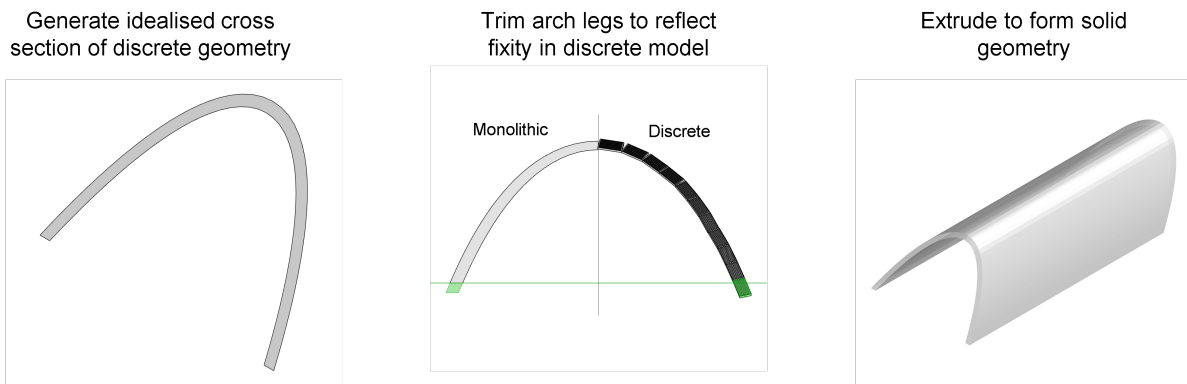


Figure 8.1: Monolithic vault modelling approach

8.2.2 Numerical modelling

Since the monolithic vault is a continuous structure, a continuum modelling and analysis approach based on the finite element method (FEM) is required. Therefore, DIANA is used to carry out numerical modelling and analysis in this chapter. The Rhino model obtained from the methodology in Figure 8.1 was imported into DIANA, where boundary conditions, mesh parameters, and material properties were defined. The resulting FE model is illustrated in Figure 8.2.

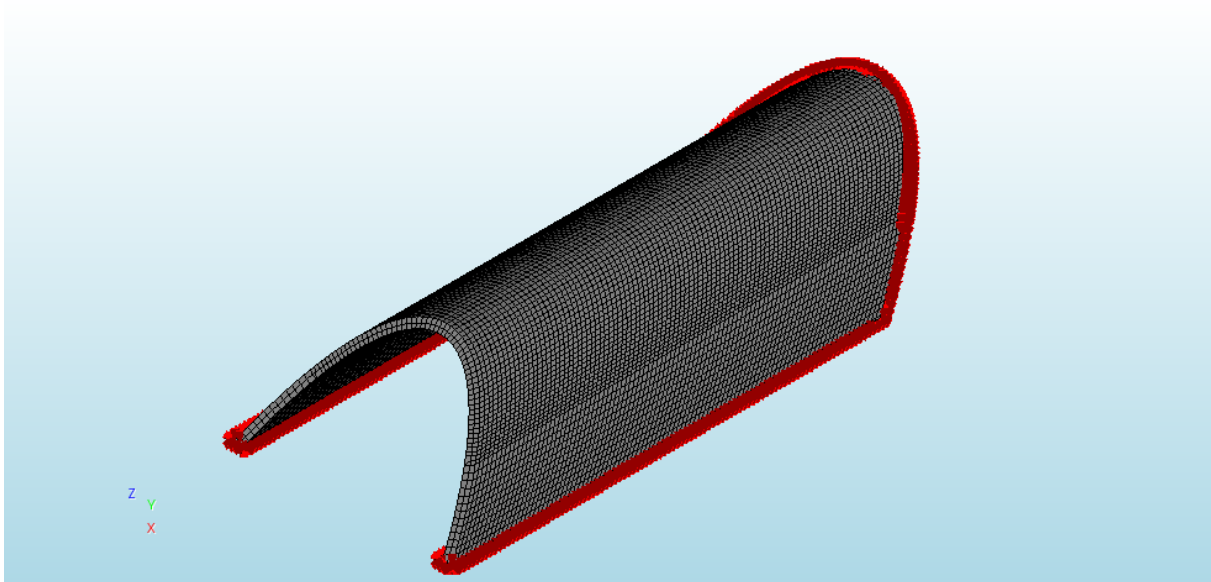
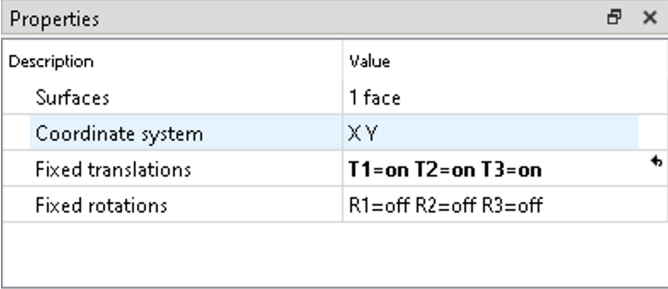


Figure 8.2: DIANA FEA model

8.2.2.1 Boundary conditions

Boundary conditions were assigned in a manner consistent with assumptions used for the brick-based vault. The location of supports is indicated by the red markers in Figure 8.2. Since the components at ground level were fixed in place in the component-based model, the monolithic vault geometry is modelled to reflect this fixity; translations were fixed in all directions, as indicated in Figure 8.3. This approach does not precisely

represent the boundary conditions at the inclined support in the discrete model, which were defined by Mohr-coulomb interfaces and allow for some degree of translation to occur. However, the results of Chapter 6.2.3 demonstrate that blocks at the inclined boundary were held in place by strong frictional confinement due to the self-weight of the vault, resulting in negligible deformations in all directions. Using fixed supports at the inclined support in the continuous model was therefore expected to most accurately reflect the boundary conditions in the discrete vault. Additionally, it was believed that allowing the monolithic vault to deform freely in the plane of this support may lead to an unreasonable decrease in its performance. In reality, the monolithic vault would likely be fixed at the inclined support, or would at the very least experience frictional confinement, as in the discrete vault.



Description	Value
Surfaces	1 face
Coordinate system	X Y
Fixed translations	T1=on T2=on T3=on
Fixed rotations	R1=off R2=off R3=off

Figure 8.3: Monolithic vault boundary condition properties

8.2.2.2 Mesh configuration

Solid elements were used because the methodology was aimed at allowing the simulation of crack localisation. Linear elements were chosen in the interest of computational efficiency. Hexahedral elements were assigned as the default mesh shape. This choice was informed by preliminary analysis with tetrahedral elements, which produced significant discontinuities in the distribution of stresses in the vault. The results of this preliminary analysis are included in Appendix B, which demonstrate that the discontinuities were resolved by using hexahedral elements.

The desired element size was initially chosen to be 0.25 m in order to have at least two elements span the thickness of the vault, which is 0.5 m. This was considered to be the lowest mesh density which could reasonably be used to calculate stresses across the cross-section of the vault. A preliminary mesh refinement study was then carried out to determine what mesh size is needed to accurately simulate the stress distribution in the vault. The results of this study are presented in Appendix B. Although the mesh refinement was limited by a computational bottleneck, the results suggested that a mesh size of 0.0750 m would produce the most accurate results. When nonlinear pushover analysis was attempted for this mesh size, however, the analysis failed due to insufficient memory. Therefore, the next smallest element size, 0.100 m was chosen for the analyses carried out in this chapter. This was done with an understanding that such a large element size may be unconservative based on the results of the mesh refinement study.

8.2.2.3 Material definition

As discussed in the literature review, sintering has not yet been applied to the AM of large-scale structures. For the purposes of this project, however, it was assumed that selective laser-sintering of regolith can be scaled up to fabricate the equivalent monolithic vault structure being studied. The elastic modulus, compressive strength, and density obtained by Goulas et al. (2019) for laser-sintered regolith are used to define the constitutive model. The elastic modulus was defined to be 287.3 MPa, and a value of 0.2 was chosen for the Poisson ratio, which was based on assumptions made by Kalapodis, Málaga-Chuquitaype, et al. (2022). The density was defined to be 2300 kg m^{-3} . The compressive strength is defined as 4.2 MPa. Tensile strength was not measured by the researchers, so it was assumed to be one-tenth of the compressive strength based on the approach taken by Kalapodis, Málaga-Chuquitaype, et al. (2022). The assumed material properties are summarised in Table 8.1. An understanding of the influence of non-linear material behaviour is desirable in order to provide a comparison to non-linearities present within the 3DEC analyses, so the analyses were set up to account for cracking through a rotating, strain-energy-based crack model. However, the tensile softening behaviour of regolith-based structural materials made with SLS is not determined by Goulas et al. (2019) and is generally not well understood in literature. Therefore, an accurate cracking model could not be confidently defined. Kalapodis, Zalachoris, et al. (2022) assume that sintered regolith properties can be defined using tension softening models for typical ceramic materials, but pursuing such a material definition is considered out of the scope of this project. Given that the investigation of a monolithic vault serves as a comparative analysis and detailed analysis is out of the scope of this project, the cracking model was simplified by assuming brittle behaviour. Although crack development was ultimately not studied for reasons explained in the following section, a brittle cracking assumption would yield a basic understanding of the failure mechanism of the vault, which could be elaborated in the future once comprehensive material models are available.

E (MPa)	ν	ρ (kg m^{-3})	σ_c (MPa)	σ_t (MPa)
287.3	0.2	2300	4.2	0.42

Table 8.1: Monolithic vault material properties

8.2.3 Pushover analysis

To conduct a pushover-type analysis which represents the equivalent static loading of a seismic event, a maximum acceleration must be specified, which is applied in fractional increments called load factors. For this acceleration, 5.0 m s^{-2} is specified, fractions of which were incrementally applied to the model. First, the model was solved under the influence of the Moon's gravity, where an acceleration of -1.62 m s^{-2} was applied in the vertical direction in one step. Next, lateral acceleration was applied in one step of 1.0 m s^{-2} , followed by steps of 0.1 m s^{-2} until failure. This series of load steps was chosen based on the mesh refinement study in Appendix B, which indicated that elastic behaviour was expected until at least an acceleration of 1.0 m s^{-2} . The smaller load step size after this point is consistent with step sizes in the analysis of the

component-based vault from Chapter 6.2.3. As mentioned earlier, the aim of simulating crack propagation until the point of global failure could not be achieved. This was due to the significant computational limitations encountered, which led to the adoption of the assumption that the vault fails abruptly once stresses exceed the tensile strength. It should be noted that this assumption is unlikely to be excessively conservative, since an unreinforced masonry structure experiencing flexure would likely fail suddenly soon after the onset of cracking. As a result, limited consideration was applied in defining detailed parameters for the equilibrium iteration scheme, which would otherwise be carefully tuned if cracking behaviour was being studied in more detail. The iteration scheme is based on the Newton-Raphson method, with a maximum number of iterations was set to 10. The force and displacement convergence criteria are set to be simultaneously satisfied. The force and displacement norms were set to have a tolerance of 0.01.

In order to produce results that can be directly compared with those obtained for the discrete vault, displacement results are recorded for the node pictured in Figure 8.4a. As shown in Figure 8.4, this node corresponds to the outermost block tracked for the discrete vault analysis.

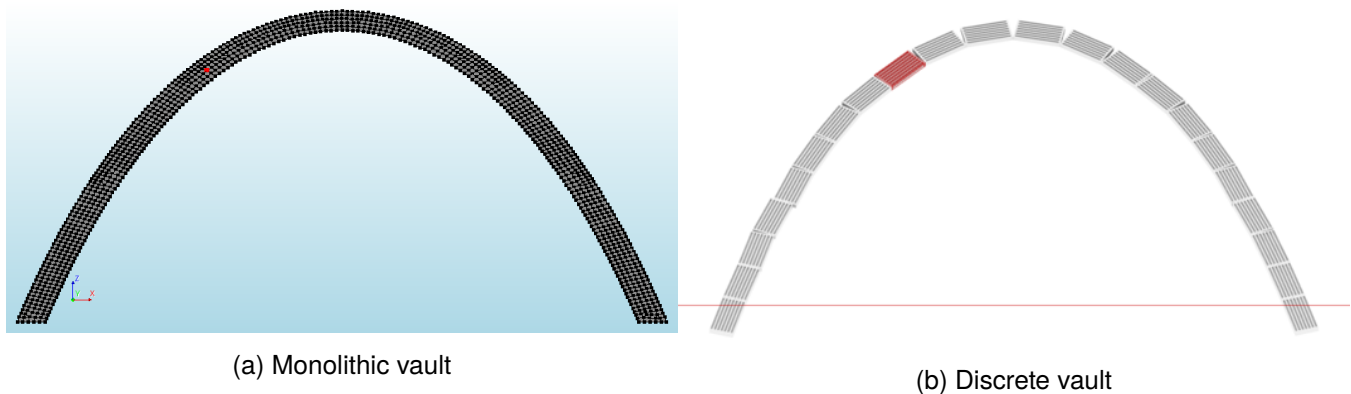


Figure 8.4: Tracking point definition

8.2.4 Eigenvalue analysis

Dynamic time-history analysis would provide valuable results for comparing the performance of brick-based versus equivalent monolithic vaults, but such an analysis is considered to be out of scope of this project due to time limitations. Instead, basic insight into the nature of the dynamic response is gained by performing an eigenvalue analysis on the vault in DIANA. As with the eigenvalue analysis carried out in Chapter 6, the first six modes of vibration are determined for the monolithic vault.

8.3 Results

8.3.1 Quasi-static analysis

The pushover behaviour of the monolithic vault is pictured in Figure 8.5. As with previous analyses that were carried out according to the DEM analysis framework presented in Chapter 4, displacement at a representative node is tracked while acceleration increases incrementally. The tracking node is indicated in

red in Figure 8.4. Figure 8.5 illustrates how the behaviour of the vault is defined by an elastic response until an acceleration of 1.4 m s^{-2} is reached. At the following load step, the maximum principal tensile stress exceeds the tensile strength, which is assumed to constitute failure.

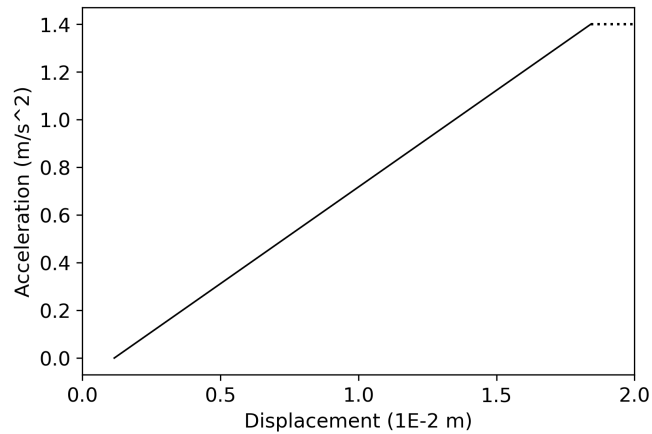


Figure 8.5: Pushover analysis of monolithic vault

The model state at the last acceleration step before failure is shown in Figure 8.6, which is a contour plot of maximum principal stress in the vault. The acceleration leading to this model state corresponds to a load factor of 0.28, which results in an acceleration of 1.4 m s^{-2} . The maximum stress is 0.400 MPa , which is slightly below the tensile strength of 0.420 MPa .

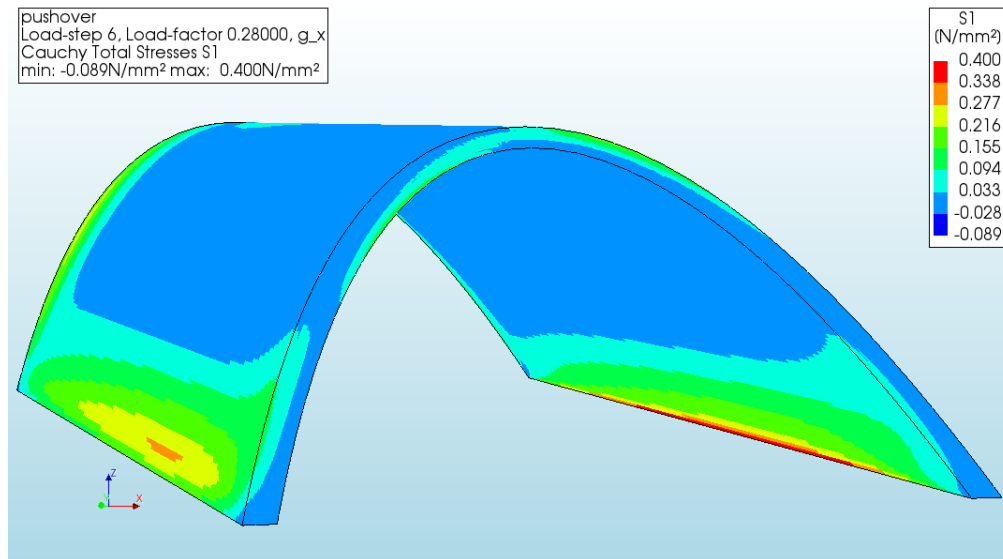
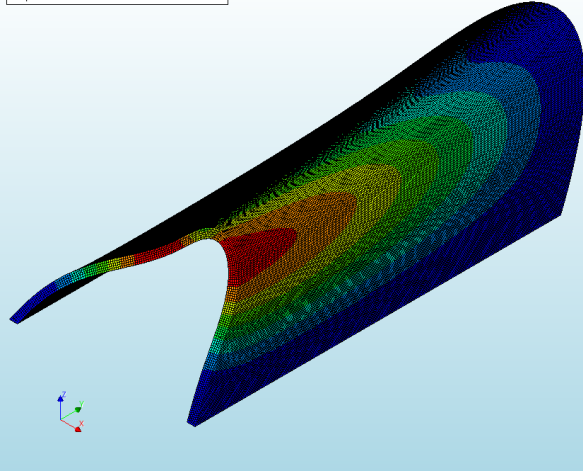


Figure 8.6: Principal stresses in monolithic vault state before failure

8.3.2 Eigenvalue analysis

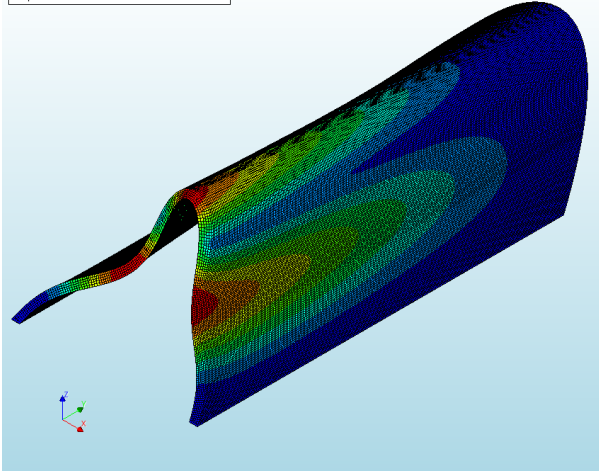
The six main modes of vibration are 1.53 Hz, 2.65 Hz, 2.95 Hz, 3.06 Hz, 3.99 Hz, and 4.24 Hz, which are depicted in Figure 8.7.

eigenvalue
Mode 1, Eigen frequency 1.5276 Hz
Displacements D1XYZ



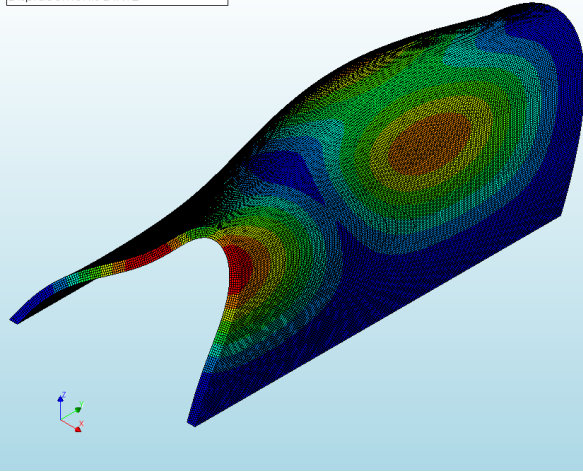
(a) Mode 1 (1.53 Hz)

eigenvalue
Mode 2, Eigen frequency 2.6527 Hz
Displacements D1XYZ



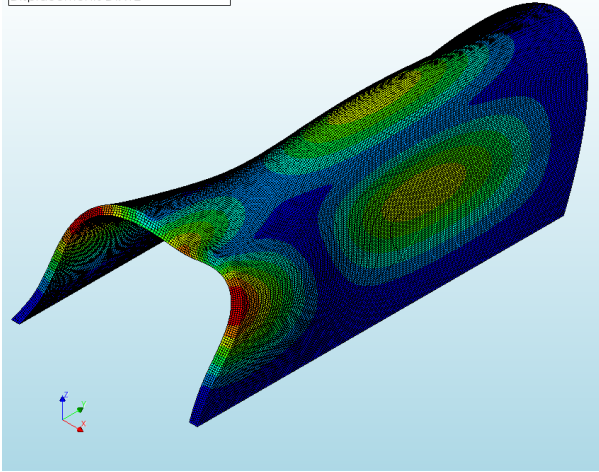
(b) Mode 2 (2.65 Hz)

eigenvalue
Mode 3, Eigen frequency 2.9518 Hz
Displacements D1XYZ



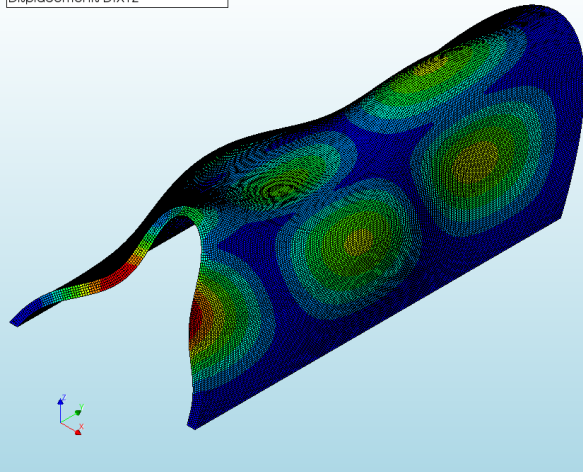
(c) Mode 3 (2.95 Hz)

eigenvalue
Mode 4, Eigen frequency 3.0589 Hz
Displacements D1XYZ



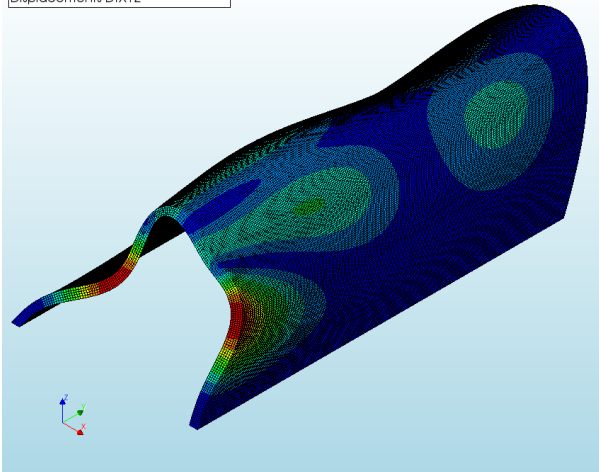
(d) Mode 4 (3.06 Hz)

eigenvalue
Mode 5, Eigen frequency 3.9920 Hz
Displacements D1XYZ



(e) Mode 5 (3.99 Hz)

eigenvalue
Mode 6, Eigen frequency 4.2359 Hz
Displacements D1XYZ



(f) Mode 6 (4.24 Hz)

Figure 8.7: Natural modes of monolithic vault

8.4 Discussion

When subjected to a pushover analysis, the monolithic vault was able to resist an acceleration of 1.4 m s^{-2} before the tensile strength was reached. This elastic pushover behaviour is shown in Figure 8.5, where the vault is considered to fail once the maximum principal tensile stress exceeds the tensile strength. Each load step until this point converged with one iteration, as would be expected for a structure behaving elastically. Studying the evolution of failure in this vault is not in the scope of this project, so further analysis into studying the cracking behaviour was not pursued. Ignoring possible inaccuracy due to a coarse mesh size, these results indicate that the monolithic vault is expected to fail slightly below the assumed 475-year PGA defined by Ruiz et al. (2022), though the actual capacity would likely be slightly higher if crack development was studied; it was assumed that the vault failure once its tensile strength is reached, but in reality, progressive cracking would likely allow for a higher acceleration to be resisted, particularly if a tension softening constitutive model is used. It is important to note, however, that the modelling approach taken is actually likely to be unconservative due to the course mesh density used. The mesh sensitivity study from Appendix B indicates that a mesh size of 0.100 m is too coarse to accurately simulate the distribution of stresses in the vault. It is not clear how much the actual capacity of the monolithic vault would be decreased by further mesh refinement, but some decrease in strength is expected. Further mesh refinement is desirable to more accurately model the stress state in the vault.

Although mesh refinement is necessary to confidently estimate the actual performance of the model, this analysis still provides valuable insight into how an additively-manufactured vault may compare to the discrete type studied in this project. Most importantly, the results indicate that the monolithic vault cannot elastically resist the required acceleration. Furthermore, as shown in Figure 8.8, the monolithic vault shows a slightly less stiff response than its component-based counterpart during early loading. Upon mesh refinement, it is possible that the monolithic vault will exhibit failure at an even lower acceleration, but the overall trend in behaviour is not expected to change significantly; regardless of refinement or tension softening, the monolithic vault would exhibit elastic deformation until the onset of cracking, after which brittle failure can be expected. The component-based vault, on the other hand, exhibits significant stiffness degradation and large displacements as it reaches the design acceleration under quasi-static loading, but it does not become unstable and hence is not considered to fail. The difference in initial stiffness can be explained by differences in assumed manufacturing processes. The material definition for the monolithic vault is consistent with AM laser sintering techniques, which results in materials with a lower stiffness than conventionally-sintered bricks.

Table 8.2 provides a comparison between the first six modes of vibration of the two types of vaults. It is noteworthy that the modes for the discrete vault are significantly higher than those of the monolithic equivalent. This is expected when considering that the structural behaviour of the vault is defined by numerous discrete blocks; the discontinuous nature of the vault prevents the formation of long-period modes associated with large-span continuous geometries.

In addition to the insufficient lateral acceleration resistance of the monolithic vault, elastic structural behaviour is typically not associated with high seismic performance. In other words, it may not be sufficient to

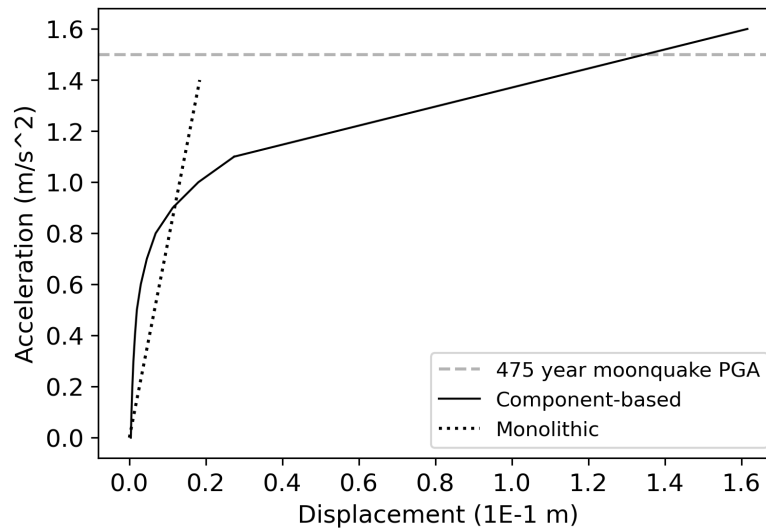


Figure 8.8: Monolithic vs. discrete pushover

Vault type	Mode (Hz)					
	1	2	3	4	5	6
Discrete	7.29	8.73	10.36	10.88	13.37	13.46
Monolithic	1.53	2.65	2.95	3.06	3.99	4.24

Table 8.2: Natural mode comparison between discrete and monolithic vaults

increase the thickness of the monolithic vault to obtain a structure that can safely resist moonquake loading. When designing structures to resist ground motions, plasticity is desirable because it allows for energy dissipation. Furthermore, structural redundancy is needed to ensure that if failure does occur, it does not result in progressive collapse. An unreinforced, monolithic vault made of a brittle material such as regolith will not dissipate energy effectively and is susceptible to progressive collapse due to a lack of redundancy. With this in mind, the large displacements and stiffness degradation observed in the component-based vault are not considered to be a significant concern because the vault was shown to settle into a stable configuration after removing the lateral acceleration in Figure 6.8. Additionally, as long as the components do not experience localised damage, they can be readily reconfigured to recreate the original state of the vault. This is a particularly appealing benefit of the structural system studied in this project, which may result in significant cost savings during the service life of the vault. It is important to understand that the maximum acceleration level resisted by the vault corresponds to an ultimate limit state, which has a low probability of occurrence. In the event that such moonquake loading does occur during the service life of the structure, the possibility to repair the structure rather than rebuilding it is highly appealing. This is especially true in extreme extraterrestrial environments where it may be challenging and expensive to rapidly mobilise the tools needed to build a new vault, as would be necessary for the monolithic type. Additionally, it is important for shielding structures to be easily repairable based on the commentary about impact protection in Chapter 2.

COMPARATIVE ANALYSIS II - REGOLITH OVERBURDEN

9.1 Overview

Literature reviewed in Chapter 2 indicates that shielding structures are necessary in off-Earth environments to provide protection against radiation and space debris impacts (Akisheva & Gourinat, 2021; Kalapodis et al., 2020; Sanders & Larson, 2013; Spedding et al., 2020). Many design concepts for ET habitats or shielding structures envision the incorporation of a loose regolith covering over the primary structure in order to satisfy protection requirements. Several studies were reviewed in Chapter 2 which estimate the necessary thickness of bulk or sintered regolith to adequately protect humans from radiation present on the Moon (Akisheva & Gourinat, 2021; Spedding et al., 2020). According to (Akisheva & Gourinat, 2021), shielding with a minimum areal density of 1600 kg m^{-2} is needed, which translates to a vault with a uniform thickness of 0.615 m, assuming that no gaps are present and that the vault is made from the sintered regolith material tested by Indyk and Benaroya (2017). It is not in the scope of this project to examine what degree of inherent radiation protection is offered by the component-based vault, which would require an understanding of how the joints may compromise the radiation-resisting properties of the sintered regolith. Although reliable conclusions cannot be reached at this stage regarding whether a loose regolith layer is needed or how thick it should be, a conservative approach can be taken which ignores the radiation-resisting properties of the primary structure.

In this project, it is assumed that the vault offers no radiation protection and that this function is fully satisfied by a loose regolith covering. In order to provide basic insight into how loose regolith overburden may affect the stability and seismic performance of the component-based vaults studied in this project, a simplified 2D deformable arch model is created with a loose regolith covering. This model, as well as the underlying arch without regolith, are then subjected to a quasi-static pushover-type analysis. Although this approach studies a vertical arch rather than the 3D inclined vault developed in this project, trends in the results should provide an understanding of what kind of interaction can be expected between the overburden and the vault.

9.2 Methodology

9.2.1 Modelling

Given that a simplified 2D approach is chosen for this initial exploration, it is appropriate to apply the modelling methodology used in Analysis Phase I to produce an idealised arch model. As such, a vertical arch is modelled with dimensions that are equivalent to the final vault—a rise of 6 m, span of 12 m, and thickness of 0.5 m are used. The definition of length in the out of plane direction is inconsequential, so a length of 1.0 m is chosen. Afterwards, a regolith profile is defined under the assumption that loose regolith will be

gradually piled up to envelop the vault. This means that the final form of the regolith layer will be defined by slope stability. Since the friction angle of bulk regolith is between 30° and 50° according to Heiken et al. (1992), a conservative angle of 30° is assumed to define the slope in the model. The minimum thickness of regolith is modelled to be 1.0 m in order to satisfy minimum radiation requirements defined by Akisheva and Gourinat (2021). At this stage, large zone sizes is used in the definition of the regolith layer for purposes of computational efficiency, but could readily be refined for more accurate analysis. The resulting model is shown with regolith overburden in Figure 9.1.

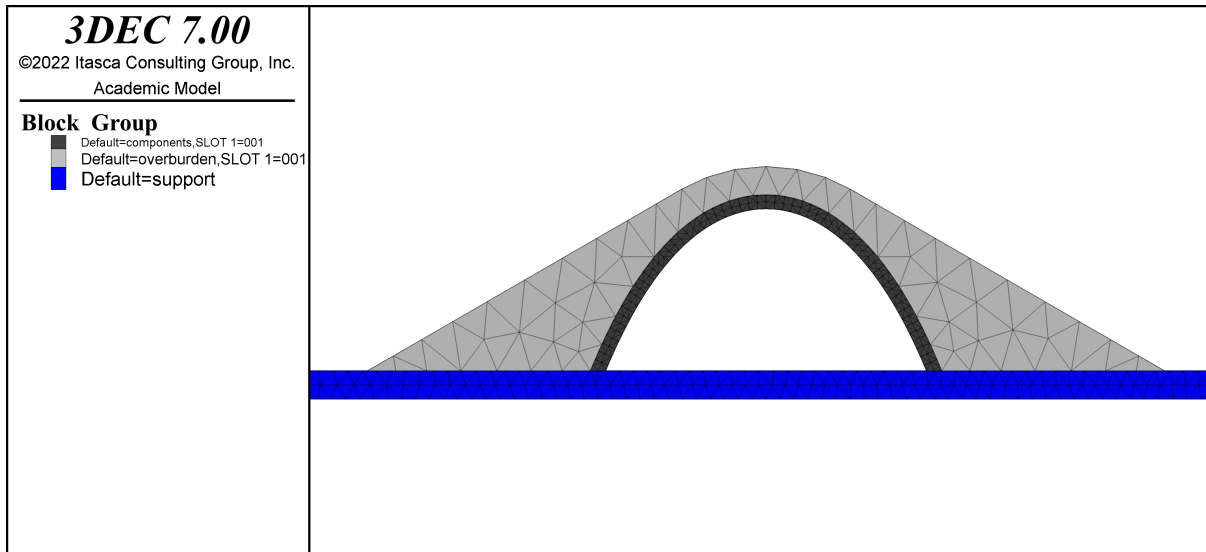


Figure 9.1: Model with regolith overburden

Deformable blocks must be used because the bulk regolith behaviour is most accurately defined by a continuous distribution of strains; it cannot be properly represented by a series of rigid blocks with strains localised at the interfaces. Therefore, the arch must also be composed out of a series of deformable blocks because 3DEC does not allow for the use of both types of block in one model. In order to import the Rhino geometry into 3DEC as a deformable block assembly, Griddle is used according to the process described in Chapter 3. The necessity of using deformable blocks creates an unmanageable computational overhead when attempting to model a 3D structure. Attempts were made to produce partial vault models with 50 courses, but importing this geometry into 3DEC utilised all of the available memory in the machine and caused it to crash. Further efforts were not made to try to increase the amount of memory allocated in 3DEC because it was clear that analysis would be infeasible due to the computational expense.

9.2.2 Analysis

The analysis in this section is carried out according to the standard quasi-static analysis framework applied throughout the project, except that modified constitutive models are used due to the application of deformable blocks. The arch components are defined using an elastic zone model, where Young's modulus and Poisson's ratio are defined based on sintered material properties defined by Indyk and Benaroya (2017). An elastic model was chosen because it was believed to most accurately recreate the approximately rigid

nature of the voussoirs in the arch. Since a deformable block model is used, nonlinear phenomena such as separation or shearing of zones can occur within a given block, which is avoided by using an elastic model. Dry joints between elastic components are modelled with a Mohr-Coulomb model, with elastic properties equivalent to those used for the components. In addition, the friction angle (ϕ) was set to 40° , dilation angle (ψ) was set to 0° , and cohesion (c) was set to 0.0 MPa, according to Table 9.1. Alternative material properties must be defined for the bulk regolith, which was modelled with a Mohr-Coulomb constitutive model due to its expected nonlinear behaviour as a loose soil. Based on available information in literature, it is assumed that the GSC-3 simulant exhibits mechanical properties that are sufficiently close to that of real Lunar regolith and can be used to define constitutive models used in this analysis (Dewoolkar et al., 2018). Table 9.1 summarises the constitutive definitions used to study the influence of a loose regolith layer on the pushover behaviour of arches.

Block group	Density (kg m^{-3})	E (MPa)	ν	c (MPa)	ψ (deg)	ϕ (deg)
Components	2.60E+03	8.36E+03	0.27	0.00	0.0	40
Regolith	1.52E+03	1.89E+01	0.42	3.10E-03	8.6	41.8

Table 9.1: Deformable block constitutive definition

9.3 Results

Figure 9.2 contains plots of lateral acceleration versus displacement for an idealised arch and the corresponding model that includes a layer of loose regolith. The domain of this figure is truncated to reflect a maximum displacement of 0.01 m to better illustrate the onset of instability. This figure illustrates how the stiffness of the arch without regolith abruptly becomes negligible at an acceleration of 0.3 m s^{-2} . The stiffness changes at several levels of acceleration before this instability occurs, but the stiffness is not significantly different just before failure compared to its value during early loading, as evidenced by similar slopes in Figure 9.2. For the model with regolith, the initial stiffness is lower, and degrades gradually throughout the analysis. There is also a sudden drop in stiffness for an acceleration of 0.3 m s^{-2} , but it is not as significant as for the arch model without regolith.

Figure 9.3 illustrates the state of both models under self-weight through the use of contour plots of displacement magnitude. A deformation factor of 50 is used. Settlement under gravity results in a maximum displacement of $1.67\text{E-}04 \text{ m}$ in the plain arch, while the addition of regolith results in a maximum displacement of $1.47\text{E-}03$. In the arch model, displacement is largest at the top, and is distributed in an approximately symmetric manner. In the model with regolith, the largest settlements are observed in the regolith at a location slightly above the midpoint of the assembly. The distribution of displacements is approximately symmetric, though the right side exhibits likely less deformation. The colour scale on the left can be used to determine the amount of displacement in the arch, which is shown to have a maximum deformation between $3.00\text{-}04$ and $4.00\text{E-}04$. This deformation corresponds to an approximately two-fold increase compared to the results for the arch alone.

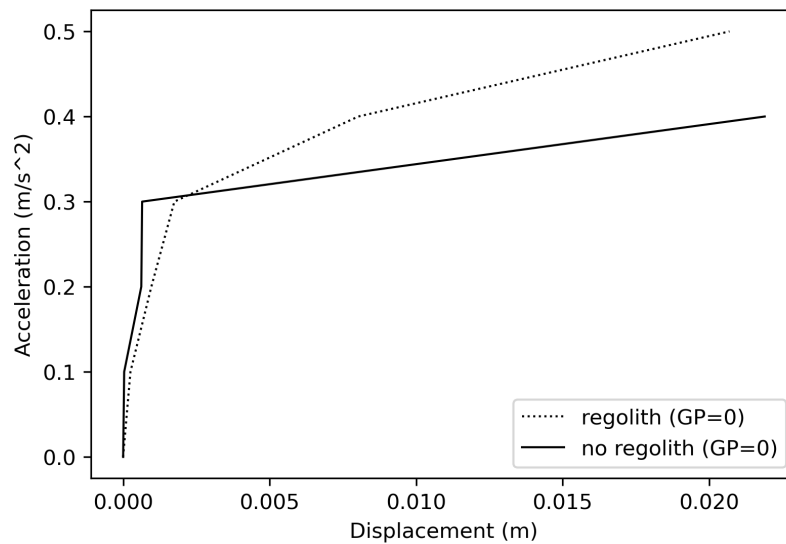


Figure 9.2: Comparison between arch pushover behaviour with and without overburden

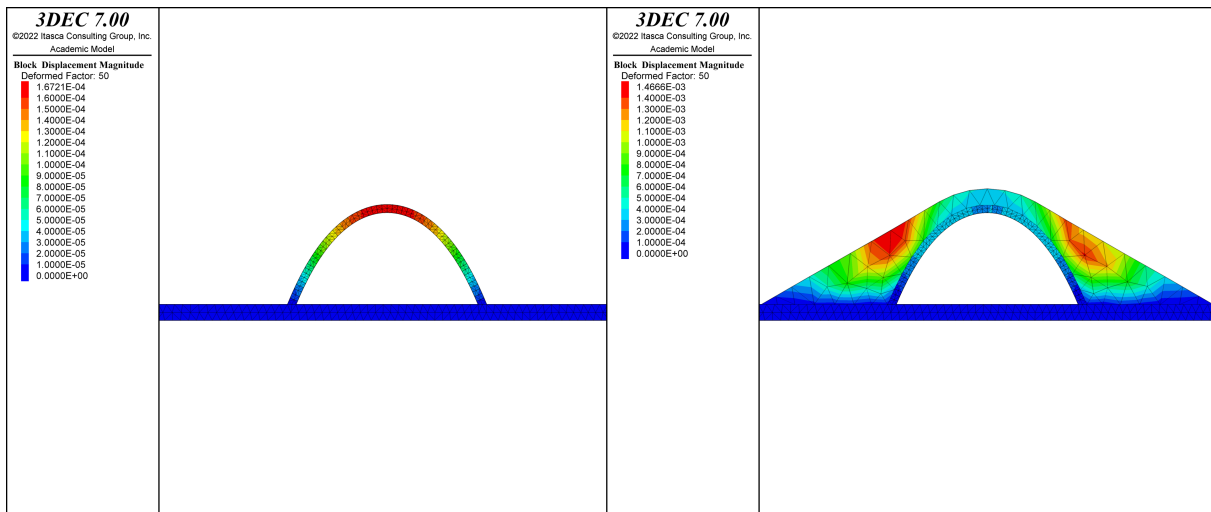


Figure 9.3: Comparison between arch displacement magnitudes under self-weight

Figure 9.4 shows the final state of each model. Again, contour plots of displacement magnitude are used, except a deformation factor of 25 is used. The arch exhibits a well-defined 4-point hinging failure, with maximum displacement occurring at the hinge located at upper right side of the arch intrados. Additional hinges are clearly observed at the intrados and extrados at the level of the support, as well as the extrados of the upper left side of the arch. The maximum displacement is shown to be $3.74\text{E-}02$ m. For the model with regolith, hinges can be observed in similar locations, but they are less clearly defined. It appears that multiple smaller hinges form near locations corresponding to the four main hinges observed in the arch alone. The maximum displacement in the model with regolith is $3.68\text{E-}02$ m.

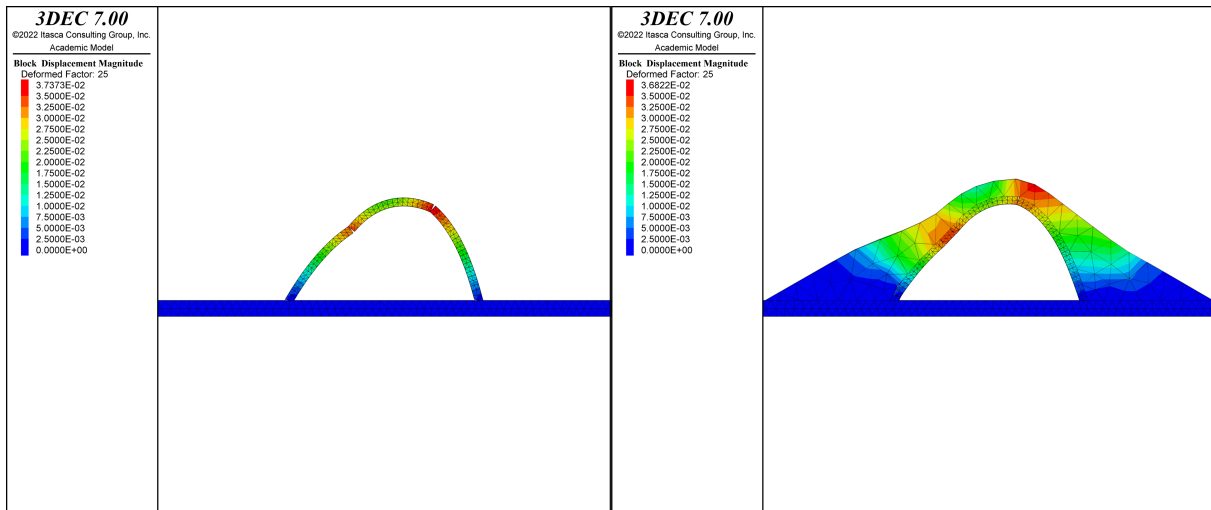


Figure 9.4: Comparison between arch displacement magnitudes at failure

9.4 Discussion

The loss of stability for the "no regolith" case is defined by a hinging mechanism typical for arches, as described in Chapter 2. This is evident from the sharp kinks in the pushover plot in Figure 9.2, each of which marks a new equilibrium configuration of the arch. Each discontinuity corresponds to the formation of a hinge in the arch and once four hinges form, rigid body motion is expected. While four kinks are not observable in this figure, it is possible that the acceleration steps are too large to capture the formation of each hinge. The pushover plot corresponding to the model with a regolith covering also contains discontinuities, but they are less pronounced. It is interesting to observe that both curves appear to form a hinge at an acceleration of 0.1 m s^{-2} and at 0.3 m s^{-2} . There is no clear kink in between these acceleration steps for the model with regolith, despite an obvious hinge forming at an acceleration of 0.2 m s^{-2} for the model without regolith. The maximum displacement of the model with regolith is smaller than for the arch alone, which is not clear from the plot in Figure 9.2, but is shown in Figure 9.4. This can be explained by the fact that the hinging mechanism exhibited by the arch results in a vertical component of displacement. Although the analysis is cut off once the maximum displacement in the X-direction is 0.03 m , the vertical displacement component results in a larger deformation magnitude. In the model with regolith, the confining weight of regolith reduces vertical deformations and results in the slightly smaller magnitude of displacement observed in Figure 9.4.

Overall, the influence of the regolith appears to be a softening of the pushover behaviour. This may be explained by the inertial coupling of the regolith with the arch; the addition of mass results in additional forces being transferred to the arch under lateral acceleration loading, leading to larger deformations under each load step. The pushover behaviour shown for the model with regolith appears to suggest that the arch is more stable due to the higher stiffness shown past an acceleration of 0.3 m s^{-2} . This result is somewhat questionable, so the final model state is examined in Figure 9.4 to better understand what may be occurring. The instability mechanism in both cases appears to be due to hinging, but the hinges appear to be artificially stabilised by the regolith, as seen in Figure 9.5. This detail provides insight into phenomena occurring at the

interface between the regolith and the arch, where the spheres represent contacts and the arrows represent shear deformation of the contacts. From this figure, it is evident that the current modelling approach does not accurately represent the interface behaviour between the regolith and the arch. The contact properties at the interface between the arch and the regolith should be defined based on the properties of the regolith, which has lower stiffness. The erroneously higher stiffness of the regolith results in an artificial improvement of stability during later stages of loading because it increases resistance to hinge openings on the extrados of the arch. Further analysis is needed to discount the possibility of such artificial increases in performance, which may be achieved through the use zones in the regolith which are substantially smaller than the component length.

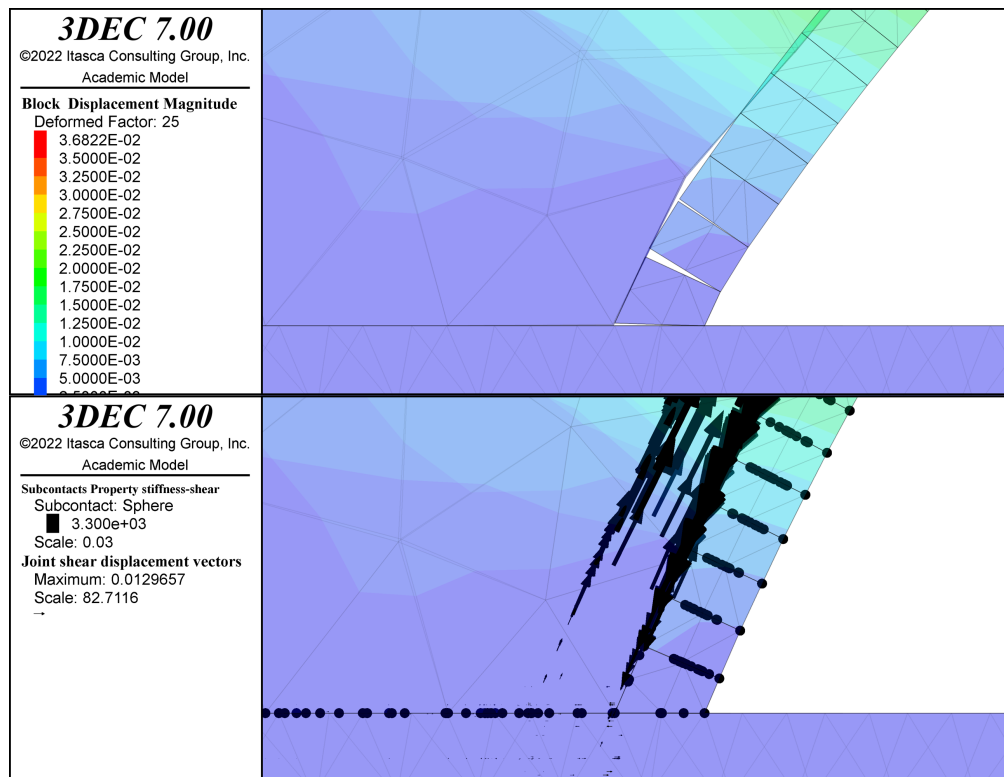


Figure 9.5: Detail of failed regolith model

COMPARATIVE ANALYSIS III - VARIATION OF GRAVITY

10.1 Overview

The final set of analyses carried out in this project investigate how the vault may resist seismic loading in different gravitational contexts, such as those found on Mars and on Earth. By varying the vertical component of gravity and conducting additional quasi-static pushover analyses, the ability of the vault to resist seismic loading in these different environments is evaluated. The results lead to valuable insight about the influence of gravity on the stability of the vault and about its feasibility for its applications outside of the Lunar context.

10.2 Methodology

The final vault model developed in Analysis Phase II is subjected to two additional quasi-static pushover-type analyses under terrestrial and Martian gravity. Information about how this model was developed can be found in Chapter 3. The analysis approach from Analysis Phase II is recreated exactly, except that the vertical component of gravity is varied. Therefore, details about the analysis configuration will not be repeated here, as they can be found in Chapter 6.2.3.

10.3 Results

Figure 10.1 compares pushover curves corresponding to the final vault geometry subjected to three different gravity load cases: $g_{\text{Earth}} = -9.81 \text{ m s}^{-2}$, $g_{\text{Mars}} = -3.72 \text{ m s}^{-2}$, and $g_{\text{Moon}} = -1.62 \text{ m s}^{-2}$. The stiffness throughout loading is positively correlated with the magnitude of gravity. The displacement under self-weight also increases with increasing gravity. It appears that the rate of degradation is negatively correlated with gravity, with the rate of change in slope decreasing as gravity increases.

Figure 10.2 presents the same data as in Figure 10.1, except that the Y-ordinate is normalised against the gravity corresponding to each case. This is what is meant by the term "locally normalised." In this figure, the normalised acceleration-displacement relationship shows the highest stiffness for the case with Lunar gravity. Stiffness is negatively correlated with the locally-normalised gravity.

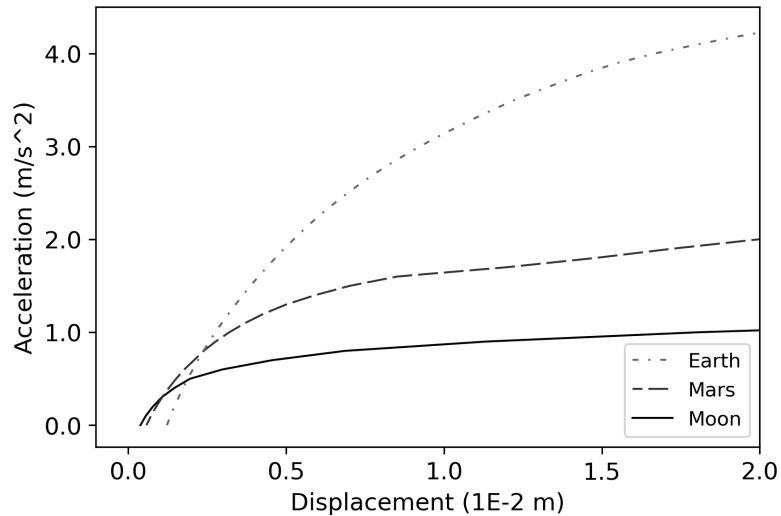


Figure 10.1: Pushover plots for Earth, Moon, and Mars

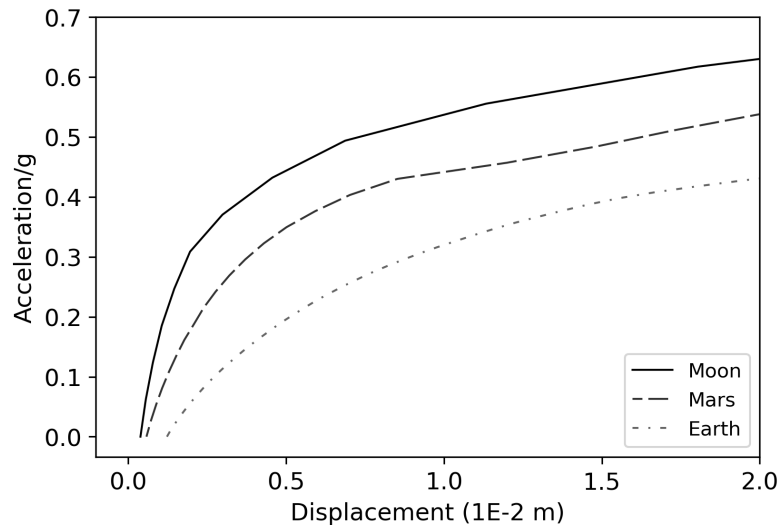


Figure 10.2: Pushover plots for Earth, Moon, and Mars (locally normalised)

The final model states for each gravity case are compared in Figure 10.3. The three contour plots shown in this figure illustrate the magnitude of displacement for the three gravitational accelerations studied. The deformation factor used is 50. The maximum displacement for the Moon, Mars, and Earth are respectively $3.32\text{E-}02$ m, $3.37\text{E-}02$ m, and $3.52\text{E-}02$ m. In each plot, this maximum displacement is concentrated in a similar region in the outermost course, which is located on the upper left side of the vault. Towards the outer parts of the vault, the deformed shape appears quite similar for each case. As gravity increases, it is notable that the distribution of displacements throughout the vault becomes more dispersed. For the Lunar case, displacements are highly concentrated towards the end of the vault, and rapidly diminish towards zero as proximity to the inclined support grows. As gravity increases, a larger proportion of the vault experiences significant deformations, evidenced by more of the vault being coloured in green and teal.

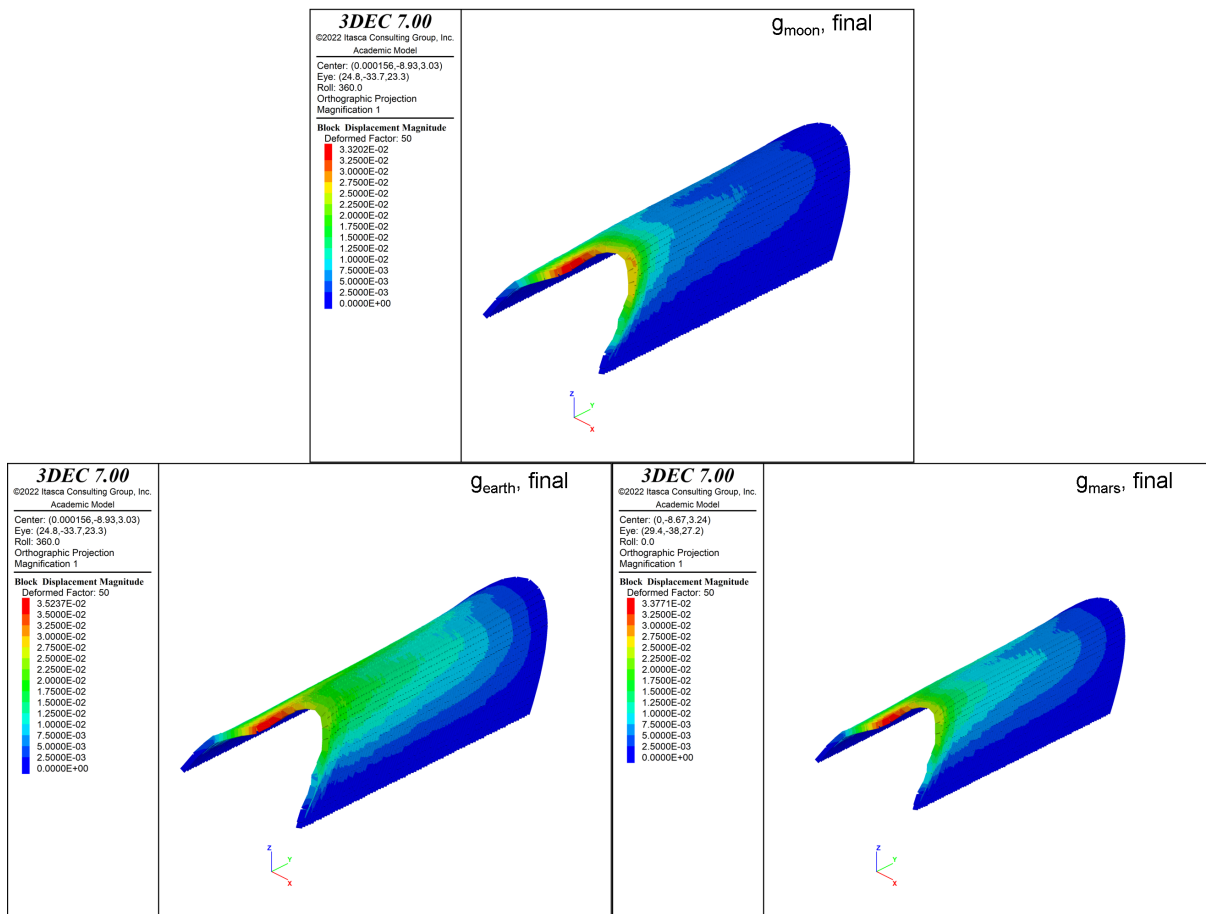


Figure 10.3: Comparison of final model states for varying gravity

10.4 Discussion

It is clear from Figure 10.1 that increasing gravitational acceleration leads to a larger capacity for lateral loading. This trend is generally consistent with thrust line analysis theory, specifically in seismic applications developed by Michiels and Adriaenssens (2018), where it is shown that the stability of a laterally loaded funicular structure is dependent on the proportion between vertical and lateral acceleration. This means that for the same lateral loading, funicular structures subjected to increasing vertical gravity will be increasingly stable, as long as Heyman's limit design principles are satisfied (Heyman, 1966). Examining Figure 10.2 in more detail, however, illustrates an inconsistency with these theoretical principles of stability. For the pushover plot corresponding to the Earth gravity case, one might expect the apparent stability behaviour to be about six times better for Earth compared to the Moon due to gravity being about six times larger. Despite lacking a clear onset of instability, the overall performance of the vault subjected to Earth's gravity is not representative of a six-time increase in stabilising vertical force. Like the results shown in Analysis Phase I, this points to some inconsistency between the dry-stone, Nubian-type vault and structures that perfectly conform to Heyman's limit design principles.

Previously, it was shown that there is an additional instability mechanism that manifests in the out-of-plane direction, which is characterised by a type of overturning shown in Figure 5.16. This out-of-plane overturning

is particularly apparent in the final vault geometry under Earth's gravity, as shown in Figure 10.4. From this figure, it is evident that a significant proportion of the vault experiences deformations in the out-of-plane direction. When comparing deformed model states in Figure 10.3, the results for Earth's gravity show a far more distributed, global deformation than the Moon and Mars, which show a comparatively localised type of deformation.

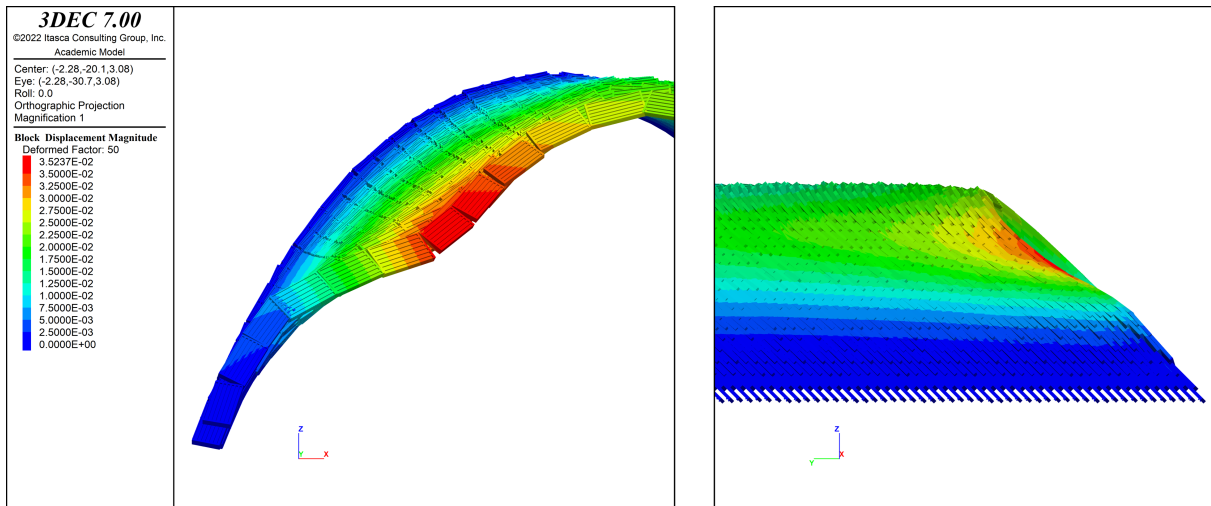


Figure 10.4: Out of plane instability in final model state (g_{Earth})

These results indicate that the influence of out-of-plane instability grows with increasing gravity, which is also supported by Figure 10.2. By normalising each plot against its respective gravitational acceleration, the results show that Lunar loading conditions result in the most favourable performance relative to its gravity. The growing influence of out-of-plane instability for larger gravity is concerning because it may lead to bending of components.

Chapter 11

CONCLUSIONS

11.1 Summary

The work presented in this thesis aims to answer the following research question:

"How do pitched-brick vaults composed of regolith-based mechanically interlocking components perform under the combined effects of microgravity and ground motion present on the Moon?"

The main contributions of this thesis stem from studying the fundamental behaviour of dry-stone, Nubian-type vaults, and whether they can safely resist possible moonquake loading. Various sub-questions are answered through the execution of a series of analyses, ultimately leading to valuable reflections regarding the performance of the Nubian-type vault. Defining performance requires an understanding of expected actions on a structure during its service life, as well as the degree to which the structure can safely resist these actions. To define actions on the structure, preliminary formulations of moonquake hazards found in literature are used, regardless of the limitations described in Chapter 2.3.2. The various investigations carried out in three Analysis Phases provide an indication of how the Nubian-type vault performs with respect to safely resisting these moonquake hazards. Prior to carrying out the Analysis Phases, frameworks are formulated to standardise modelling and analysis tasks. The modelling framework utilises Rhino and its graphical algorithmic editor known as Grasshopper to create parametric models of various vault geometries, which are then translated into equivalent distinct element models in 3DEC. This software is used to conduct structural analysis for three Analysis Phases with increasing levels of specificity. Together, these investigations lead to the development of a preliminary structural design solution for Lunar shielding structures that are resistant to moonquakes. The main findings from the Analysis Phases are presented with respect to the sub-questions they answer.

1. *"What is the influence of component width and course inclination on the performance of these structures?"*

The parametric study of vault geometry carried out in Analysis Phase I provides novel insight into the fundamental structural behaviour of dry-stone Nubian-type vaults. Particularly important is the understanding of how component width and course inclination influence the ability of these structures to resist lateral acceleration. Component width was shown to be positively correlated with lateral acceleration resistance. Larger

component widths generally achieved a higher degree of stability, as measured by the maximum acceleration which could be applied before a significant degradation of global stiffness was observed. This trend is consistent with conventional stability theories applied in masonry design, as described in Chapter 2.4.1. In practice, however, the maximum possible component width was shown to be limited based on tessellation constraints, which make it infeasible to use repeating components with a width larger than 0.5 m to construct the specified vault geometry. This does not discount the possibility that a different global form may enable the use of wider components. As mentioned in 5.3.1, the sharp curvature at the top of the vault makes it problematic to discretise the structural form using large components. This may be resolved with a smaller rise-to-span ratio or an entirely different form, such as one based on semicircular or elliptical thrust lines.

In addition to illuminating the relationship between lateral acceleration capacity and geometric variation, the analyses of Chapter 5 demonstrated important nuances about the pushover behaviour of the vaults, which appear to limit the degree to which stability can be improved through increasing component width. Out-of-plane instability mechanisms can form in this type of vault, which tend to cause premature loss of stability and can explain several inconsistencies observed in the results. The presence of out-of-plane movements also suggests that the dry-stone Nubian-type vault may not satisfy key assumptions necessary for the application of thrust limit analysis, and thus cannot be accurately analysed using conventional analytical notions of masonry stability. These observations provide justification for the choice of using DEM analysis to study this type of structure.

A comparison of results for different values of inclination indicate that maximum stability under lateral loading is reached with an angle of 45° , with diminished stability for inclinations above and below this value. The previously mentioned out-of-plane instability leads to some uncertainties in the results, but the conclusion that a 45° inclination is optimal nevertheless is supported by evidence in Chapter 5. The influence of other parameters such as thrust line shape was ultimately determined to be inconsequential for further studies of the final vault geometry.

In summary, for a global vault geometry defined by a span of 12 m and a rise of 6 m, the most feasible configuration of component width and course inclination which maximises stability under seismic loading corresponds to a component width of 0.5 m and an inclination of 45° .

2. "How does the stability of these structures evolve throughout different stages of the fabrication process?"

The results of Analysis Phases I and II both demonstrate that the global stiffness of the Nubian-type vault decreases as the course number increases, resulting in a lower seismic performance for larger, longer models. This rate of stiffness degradation diminishes as the models become larger, however, with a small difference in performance observed between 100 and 200 courses. The majority of stiffness degradation occurs between 10 and 50 courses, resulting in up to a two-fold decrease of acceleration capacity for the idealised vault models studied in Analysis Phase I. For vaults assembled with interlocking components, the degree of stiffness degradation was observed to be less severe. Analysis of the final vault model in Analysis

Phase II shows that despite the degradation of stiffness throughout construction, the full-scale Nubian vault may be able to safely resist moonquake loading. The results obtained from the staged analyses also provide insight into how the vault is expected to perform if its length were to be reduced. This understanding can be used to justify the use of partial vault models in future research, which will avoid the large computational demand associated with full-scale models.

In this project, construction phasing was defined on a global level, based on the degree of completion of the full-scale vault. To fully understand how the stability of these structures evolves during construction, however, local-level analysis of incomplete courses should also be studied in detail. Preliminary local phased analysis was carried out to study the stability of a representative course as individual components were added. These results indicated that for an inclination of 45° , the mechanical interlocking mechanism maintains the integrity of incomplete courses and prevents components from falling off of the vault. This preliminary analysis was achieved through modelling simplifications, so more thorough analysis in this direction should be addressed in future research.

3. "Can these structures safely resist moonquake loading?"

There are various uncertainties regarding safe levels of damage in the structure, moonquake loading, and material non-linearity, so an accurate answer to Sub-question 3 requires some nuance. The first qualifying factor to consider is that the scarcity of moonquake data results in a significant research gap for probabilistic design tools; the UHS used to define the design-level acceleration was the first of its kind, and is specific to a site that may not be representative of actual settlement sites. Hazard spectra based on probabilistic seismic hazard analysis for the Moon were absent from literature prior to the publishing of Ruiz et al. (2022). The site used to develop a UHS in this paper is close to a fault, which may result in uncharacteristically high seismic loading. Despite this possibility that the assumed actions are conservative, the results of the quasi-static analysis suggest that the vault will be stable when subjected to the assumed design acceleration acting in a direction aligned with the span of the vault. The time-history analysis, on the other hand, indicates that partial collapse of the vault is possible under a ground motion that is aligned with the vault span. Though concerning, it is important to acknowledge that less than 4% of the vault collapsed in this way, and the damage was localised to the outermost courses. This indicates that by strengthening the outer parts of the vault, significant improvements in performance may be possible. Furthermore, the vault was shown to be stable after the moonquake simulation—aside from the partial collapse—so this degree of damage may be acceptable for ultimate limit state design. Additionally, it is important to consider that the dynamic analysis was undamped, which means that the results are likely to be conservative. For a more realistic damped analysis, this partial collapse may not occur. The influence of out-of-plane motion in seismic loading was not studied in either the quasi-static analysis or the dynamic analysis, but is expected to be detrimental to the real dynamic performance of the vault.

In short, the vault studied in this project may be able to safely resist moonquake loading, but further analysis is needed to make a definitive conclusion. In particular, comprehensive dynamic analyses with ground

motions in various directions are needed. If these analyses demonstrate significant potential for collapse, external reinforcement may be needed.

4. *"What is the dynamic response of the structures when subjected to Lunar ground motions?"*

The configuration of the dynamic analysis presents several uncertainties. Aside from the limitations of the assumed design spectrum described earlier, the lack of damping in the analysis suggests that the observed dynamic response of the vault should be interpreted with a degree of caution. Additionally, dynamic loading was only applied in one direction, so it is not clear how the vault would respond to out-of-plane or vertical seismic loading. Despite these uncertainties, important conclusions can be drawn from the preliminary dynamic analysis results.

Although the close overlap between natural modes of the vault and the peak response in the UHS by Ruiz et al. (2022) initially suggests that significant dynamic amplification could arise, the time-history response does not indicate that significant amplification is occurring. This can be explained by the fact that the eigenvalue analysis is performed assuming that the system is elastic, when in reality, the blocks exhibit significant plastic deformation, leading to energy dissipation due to sliding. The partial collapse observed in the end of the vault can be attributed to the lack of confinement in this region, which results in low frictional forces at the interface. Since the friction angle is lower than the angle of inclination, the stability of blocks in the outermost course is primarily defined by conventional kinematic equilibrium considerations described in Chapter 2.4.1. The low shear strength at the interface allows the blocks to displace with limited frictional resistance once kinematic equilibrium is overcome, though the outer components will be held in place to some degree by mechanical interlocking. This may lead to growing displacements with various cycles of load reversal, particularly if the wedge components separate from the vault. Eventually, component pins may become dislodged from their respective grooves, which will result in progressive collapse of the course. The confining pressure of outer courses helps maintain the integrity of interior courses, but once the outermost course collapses, the blocks behind it becomes unconfined and are therefore susceptible to the same instability.

It is not clear whether the progressive collapse of outer courses described above would occur in an analysis which employed realistic values for damping. Given that the presence of damping would help dissipate energy, it is possible that the local instabilities leading to partial collapse may not manifest in a damped analysis. Additional uncertainties exist due to the use of a truncated ground motion because it does not capture the effect of the rise and decay of the signal, though this is not expected to have a very significant impact on the results. To address the limitations of the current analysis, further damped analysis is needed. Additionally, ground motions should be applied in several directions to more fully characterise the dynamic response of the Nubian-type vault.

5. *"How does the structural performance of an assembly of interlocking components compare to that of an equivalent monolithic structure?"*

Without a dynamic time history response for the monolithic vault, it is difficult to comprehensively compare the structural performance of the discrete vault to that of its monolithic counterpart. Still, important insights can be drawn based on the results of the quasi-static and eigenmode analyses.

The results of the eigenmode analysis show that the natural frequencies of the monolithic vault are about half as large as the discrete vault, which may slightly reduce the risk of dynamic amplification based on the lesser degree of overlap with the peak spectral response periods defined in the assumed design spectrum. This is only accurate when considering low-amplitude ground motions, however, since the component-based vault's behaviour is otherwise dominated by inelastic sliding between components, which is expected to prevent dynamic amplification.

The quasi-static results suggest that the component-based vault may offer better performance, since the monolithic vault is expected to fail at an acceleration below the design value. On the other hand, the discrete vault was shown to be stable at the design-level acceleration, despite experiencing a large maximum displacement with significant residual deformations. It is difficult to quantitatively compare the performance of the two models, however, since an upper limit of lateral acceleration capacity for the discrete vault was not determined from the quasi-static analysis in Chapter 6. Loading beyond the design acceleration was not explored due to computational constraints, in addition to the understanding that high-magnitude loading was likely to be inaccurate without accounting for possible material non-linearities.

It is important to note that the results of the monolithic vault analysis should be approached with some caution, however, due to a mixture of both conservative and non-conservative assumptions. On one hand, the analysis may be unconservative due to the lack of sufficient mesh refinement; computational constraints required the use of a mesh size that did not appear to be sufficiently small based on the preliminary mesh refinement study. On the other hand, failure was assumed to occur once the maximum stress in the vault surpassed the tensile strength of the material, when in reality, crack evolution may result in a slightly higher capacity. Furthermore, tension softening in sintered regolith is expected to increase capacity, though the increase would likely be small due to the brittle nature of the material. Overall, the conservative aspects of the analysis are not expected to outweigh the unconservative aspects, and thus the equivalent monolithic vault is understood to be insufficiently strong. This conclusion is further justified when considering the incorporation of a material safety factor, as will be necessary for safe design. Accounting for material reliability will further reduce the maximum acceleration that can be resisted by the monolithic vault. Statistical variation of strength properties in dry-stone masonry structures is not a significant concern since they are typically governed by stability, so the acceleration capacity of the vault likely does not require reduction with a safety factor; reliability considerations are accounted for in the choice of applied loading.

In addition to its insufficient capacity for seismically-equivalent static loading, it is important to note that the monolithic vault presents other issues with structural safety. In particular, it is generally inappropriate to use unreinforced masonry structures such as the monolithic vault for seismic design because the failure mechanism would be brittle and is likely to result in progressive collapse. Energy put into the monolithic vault through shaking will not experience significant dissipation, which could lead to highly damaging dynamic

effects and sudden failure. Fabrication and lifecycle considerations are also important considerations for classifying the overall performance of a design. At this stage, there is too much uncertainty to make authoritative conclusions about which manufacturing approach is more feasible overall, but the component-based vault does offer the distinctive advantage of being reconfigurable. Additionally, components can be manufactured using conventional sintering, which is a more mature manufacturing technology than AM sintering.

6. *"How does the addition of a covering of loose regolith influence the stability and seismic response of the completed structures?"*

Although a simplified approach was taken in studying the influence of regolith overburden on the vault, important insights can still be derived by considering a 2D model. The results suggest that the addition of a loose regolith layer tends to lower the stiffness and stability of an ideal arch. A similar trend is expected for a dry-stone Nubian-type vault, except it is likely that the stiffness degradation will not be as pronounced. This conclusion is made on the basis that the inclined vault can distribute lateral forces throughout the structure via friction and interlocking at interfaces between courses, as was demonstrated in Analysis Phase I.

It is possible that under dynamic considerations, the regolith could improve damping in the structure due to its loose, dissipative nature. On the other hand, the additional mass added to the system may lead to a higher amplitude response. Dynamic time-history analysis is needed to fully understand the influence of a loose-regolith layer on the seismic performance of the vault. In the absence of more comprehensive analysis, the quasi-static results provide a useful indication of potential issues with performance degradation.

The apparent necessity of a loose regolith layer was based on the assumption that the vault itself offers no radiation protection, which is a conservative assumption. The degree of conservativeness is unclear due to a lack of understanding about how joints between components may compromise the protective capacity of the vault, but some degree of inherent protection is expected in reality. Based on the density of regolith samples obtained by Indyk and Benaroya (2017), a uniform shell made from this material could satisfy the radiation requirements determined by Akisheva and Gourinat (2021) if it had a thickness of 0.62 m. This value is slightly larger than the component width of the final vault model, which is 0.50 m. This suggests that modifying the design to have a slightly larger component width may result in a vault that can satisfy shielding requirements without additional materials, as long as the joints do not significantly compromise radiation resistance. As described in the response to Sub-question 1, tessellation issues that arise when using wide components can be resolved by changing the structural form to have lower curvature.

7. *"How does gravity influence the stability and seismic performance of these structures? "*

Increasing gravity is shown to lead to higher seismic capacity of the vault geometry due to the stabilising effect provided by larger downward forces. Relative to the respective magnitude of gravity in each environment, however, the vault geometry performs best on the Moon. This performance is measured by

normalising the capacity for resisting lateral acceleration against the vertical component of gravity. The vault likely performs best in the Lunar context due to out-of-plane instability being exaggerated by the larger material deformations brought about by higher gravity. With the larger stresses expected under higher gravity loading, the issue of material nonlinearity may be more prescient. In all analyses of the vault model, rigid blocks were used, which do not account for nonlinear material effects. Further analysis is needed to assess the likelihood of cracking or crushing of components, as well as shearing of pins. Disregarding potential material failure, the results indicate that the dry-stone, Nubian-type vault may be suitable for applications on Earth or Mars, particularly in areas of low seismic activity.

11.2 Scientific contributions

The aim of this project was to analyse the stability of the dry-stone Nubian-type vault concept developed by Konstantatou et al. (2022) under the combined influence of microgravity and seismic loading. The summary of this research provided in Chapter 11.1 demonstrates that the main objective has been met, as evidenced by a series of responses to each of the sub-questions originally formulated in Chapter 1.2. Novel scientific contributions resulted from this research, which address the gap in existing literature regarding the structural behaviour of a dry-stone variant of the Nubian vault typology found in vernacular North African architecture. Previous research into this type of structure indicated that it would likely be stable under its own weight based on limit design principles, but its behaviour under seismic loading was not studied. This project developed a novel framework for modelling and analysing the dry-stone Nubian-type vault according to the distinct element method, which yielded an understanding of its stability under the influence of microgravity and seismic loading.

11.3 Future research

Due to the novelty of the component-based structures studied in this project and in ET design overall, there are many opportunities for a wide breadth of research relating to furthering the development of the type of structure investigated in this project. The Nubian-type vault geometry shows promise for both on-and-off-Earth applications, but further analysis is needed to account for several uncertainties and limitations present in the current approach. The main research directions which require further development are identified to be:

- **Material nonlinearity:** The possibility of material failure, such as cracking of components and shearing of pins, was not accounted for in this project. Although the vault appears to behave in a compression-only manner consistent with limit design principles when loaded under self-weight and low levels of lateral acceleration, it is possible that under the large deformations observed during high levels of seismic loading, stress concentrations can form, or the vault can be reconfigured in a way that causes bending of components. Such conditions may result in material failure for sintered regolith, which has low tensile strength. Combined finite-discrete element analysis should be carried out to assess the

stress state of the model and to determine if material nonlinearity may diminish its structural performance.

- **Ground motion direction:** The analyses in this project were based on in-plane seismic loading, which means that there is a lack of understanding of how different loading directions will alter the seismic performance. Out-of-plane ground motions may have a significant impact on the performance of the vault, since these would reduce the magnitude of frictional confinement.
- **Local stability during course assembly:** Staged analysis with a finer resolution should be carried out, which more accurately studies the stability of the model as individual components are added to each course. Research in this direction would reasonably be paired with the definition of a digital fabrication methodology, since the exact mechanism of assembly may influence the behaviour of the vault.
- **Additional loading:** Seismic loading is not the only hazard expected in extraterrestrial contexts. Additional load cases must be considered, such as those arising from micrometeorite impacts or thermal strains.
- **Geometric variation:** Variation of the global rise-span ratio and component geometry may result in better performance, so geometric optimisation should be carried out. Varying the shape of the thrust surface may also improve structural performance, especially when considering the manufacturing benefits of a global geometry with less variation in the wedge proportions. Further parametric studies to examine these factors can implement several strategies to offset the significant computational demand associated with full-scale models: vaults with a reduced number of courses can be used, and simplified components can be used in place of those with mechanically interlocking, as evidenced by the results of Analysis Phase II.
- **External strengthening:** If further analysis indicates that the vault is unlikely to be sufficiently stable on its own, external strengthening measures can be studied, such as post-tensioning with cables, or the application of composite reinforcement. Joining outer courses with mortar may also increase performance.

BIBLIOGRAPHY

- Akischeva, Y., & Gourinat, Y. (2021). Utilisation of moon regolith for radiation protection and thermal insulation in permanent lunar habitats. *Applied Sciences (Switzerland)*, *11*(9). <https://doi.org/10.3390/app11093853>
- Allende, M. I., Kiremidjian, A. S., Lepech, M. D., & Loftus, D. J. (2021). Performance-Based Engineering Framework to Quantify Micrometeoroid Damage to Lunar Surface Structures. *Journal of Aerospace Engineering*, *34*(5), 04021055. [https://doi.org/10.1061/\(asce\)as.1943-5525.0001300](https://doi.org/10.1061/(asce)as.1943-5525.0001300)
- Ashby, M. F. (1999). 4.3 The Material Property Charts. *Materials selection in mechanical design (2nd edition)* (p. 41). Elsevier.
- Bell, L. (2011). Top-Level Considerations for Planning Lunar/Planetary Habitat Structures. *Journal of Aerospace Engineering*, *24*(3), 349–360. [https://doi.org/10.1061/\(asce\)as.1943-5525.0000062](https://doi.org/10.1061/(asce)as.1943-5525.0000062)
- Benaroya, H., & Ettouney, M. (1992). Design and Construction Considerations for Lunar Outpost. *Journal of Aerospace Engineering*, *5*(3), 261–273. [https://doi.org/10.1061/\(asce\)0893-1321\(1992\)5:3\(261\)](https://doi.org/10.1061/(asce)0893-1321(1992)5:3(261))
- Block, P., & Ochsendorf, J. (2007). Thrust network analysis: A new methodology for three-dimensional equilibrium. *Journal of the International Association for Shell and Spatial Structures*, *48*(155), 167–173.
- Buslov, E. P., Komarov, I. S., Selivanov, V. V., Titov, V. A., Tovarnova, N. A., & Feldstein, V. A. (2019). Protection of inflatable modules of orbital stations against impacts of particles of space debris. *Acta Astronautica*, *163*(January), 54–61. <https://doi.org/10.1016/j.actaastro.2019.04.046>
- Cannon, K. M., & Britt, D. T. (2021). Ice Prospecting on the Moon at Mining Scales. *Earth and Space 2021: Space Exploration, Utilization, Engineering, and Construction in Extreme Environments - Selected Papers from the 17th Biennial International Conference on Engineering, Science, Construction, and Operations in Challenging Environments*, 311–317. <https://doi.org/10.1061/9780784483374.031>
- Cesaretti, G., Dini, E., De Kestelier, X., Colla, V., & Pambaguian, L. (2014). Building components for an outpost on the Lunar soil by means of a novel 3D printing technology. *Acta Astronautica*, *93*, 430–450. <https://doi.org/10.1016/j.actaastro.2013.07.034>
- Cooper, B. L. (2008). Sintering of lunar and simulant glass. *AIP Conference Proceedings*, *969*(June), 186–194. <https://doi.org/10.1063/1.2844966>
- Coulomb, C. A. (1773). Essai sur une application des regles des maximis et minimis a quelques problemes de statique relatifs a l'architecture. *Memoires de l'Academie Royale pres Divers Savants*, Vol. 7.
- Danielson, K. T. (2014). Fifteen node tetrahedral elements for explicit methods in nonlinear solid dynamics. *Computer Methods in Applied Mechanics and Engineering*, *272*, 160–180. <https://doi.org/10.1016/j.cma.2014.01.012>
- De La Hire, P. (1712). Sur la construction des voutes dans les edifices. *Memoires del'Academie des Sciences*.
- Dell'Endice, A., Iannuzzo, A., Van Mele, T., & Block, P. (2021). Influence of Settlements and Geometrical Imperfections on the Internal Stress State of Masonry Structures, 2019–2030. <https://doi.org/10.23967/sahc.2021.131>

- Dewoolkar, M. M., Edwards, M., & Walsh, D. (2018). Shear Strength and Stiffness Characterization of Lunar Simulant GRC-3. *Journal of Aerospace Engineering*, 31(4). [https://doi.org/10.1061/\(asce\)as.1943-5525.0000848](https://doi.org/10.1061/(asce)as.1943-5525.0000848)
- Duarte, G., Brown, N., Memari, A., & Duarte, J. P. (2021). Learning from historical structures under compression for concrete 3D printing construction. *Journal of Building Engineering*, 43, 103009. <https://doi.org/10.1016/J.JOBE.2021.103009>
- Dyskin, A. V., Estrin, Y., Pasternak, E., Khor, H. C., & Kanel-Belov, A. J. (2005). The principle of topological interlocking in extraterrestrial construction. *Acta Astronautica*, 57(1), 10–21. <https://doi.org/10.1016/j.actaastro.2004.12.005>
- Elnashai, A. S., & Di Sarno, L. (2008). *Fundamentals of Earthquake Engineering*. <https://doi.org/10.1002/9780470024867>
- EN1998-1. (2004). Eurocode 8. Design of structures for earthquake resistance—Part 1: General rules, seismic actions and rules for buildings.
- Farries, K. W., Visintin, P., Smith, S. T., & van Eyk, P. (2021). Sintered or melted regolith for lunar construction: state-of-the-art review and future research directions. *Construction and Building Materials*, 296, 123627. <https://doi.org/10.1016/J.CONBUILDMAT.2021.123627>
- Fateri, M., Meurisse, A., Sperl, M., Urbina, D., Madakashira, H. K., Govindaraj, S., Gancet, J., Imhof, B., Hoheneder, W., Waclavicek, R., Preisinger, C., Podreka, E., Mohamed, M. P., & Weiss, P. (2019). Solar Sintering for Lunar Additive Manufacturing. *Journal of Aerospace Engineering*, 32(6), 04019101. [https://doi.org/10.1061/\(asce\)as.1943-5525.0001093](https://doi.org/10.1061/(asce)as.1943-5525.0001093)
- Fathy, H. (1973). *Architecture for the poor: an experiment in rural Egypt*. University of Chicago press.
- Ferrone, K. L., Taylor, A. B., & Helvajian, H. (2022). In situ resource utilization of structural material from planetary regolith. *Advances in Space Research*, 69(5), 2268–2282. <https://doi.org/10.1016/J.ASR.2021.12.025>
- Gaetani, A., Lourenço, P. B., Monti, G., & Milani, G. (2017). A parametric investigation on the seismic capacity of masonry cross vaults. *Engineering Structures*, 148, 686–703. <https://doi.org/10.1016/j.engstruct.2017.07.013>
- Garcia, R. F., Khan, A., Drilleau, M., Margerin, L., Kawamura, T., Sun, D., Wieczorek, M. A., Rivoldini, A., Nunn, C., Weber, R. C., Marusiak, A. G., Lognonné, P., Nakamura, Y., & Zhu, P. (2019). Lunar Seismology: An Update on Interior Structure Models. <https://doi.org/10.1007/s11214-019-0613-y>
- Garcia, R. F., Gagnepain-Beyneix, J., Chevrot, S., & Lognonné, P. (2011). Very preliminary reference Moon model. *Physics of the Earth and Planetary Interiors*, 188(1-2), 96–113. <https://doi.org/10.1016/j.pepi.2011.06.015>
- Gatto, G., Levrino, L., Hall, S., Wellons, J., Gargioli, E., Hoffman, J. A., Maggiore, P., Viola, N., & Viscio, M. A. (2014). Incremental architectures for a permanent human lunar outpost with focus on ISRU technologies. *65th International Astronautical Congress (IAC)*, (October), 1–11. <https://doi.org/10.13140/2.1.2674.5607>
- Giardini, D., Lognonné, P., Banerdt, W. B., Pike, W. T., Christensen, U., Ceylan, S., Clinton, J. F., van Driel, M., Stähler, S. C., Böse, M., Garcia, R. F., Khan, A., Panning, M., Perrin, C., Banfield, D., Beucler, E., Charalambous, C., Euchner, F., Horleston, A., ... Yana, C. (2020). The seismicity of Mars. *Nature Geoscience*, 13(3), 205–212. <https://doi.org/10.1038/s41561-020-0539-8>

- Gonen, S., Pulatsu, B., Erdogmus, E., Karaesmen, E., & Karaesmen, E. (2021). Quasi-static nonlinear seismic assessment of a fourth century A.D. Roman Aqueduct in Istanbul, Turkey. *Heritage*, 4(1), 401–421. <https://doi.org/10.3390/heritage4010025>
- Goulas, A., Binner, J. G., Engström, D. S., Harris, R. A., & Friel, R. J. (2019). Mechanical behaviour of additively manufactured lunar regolith simulant components. *Proceedings of the Institution of Mechanical Engineers, Part L: Journal of Materials: Design and Applications*, 233(8). <https://doi.org/10.1177/1464420718777932>
- Gunasekara, D., & Jablonski, A. M. (2021). Technical Aspects of Micrometeoroid Impact on Lunar Systems/Structures. *Earth and Space 2021: Space Exploration, Utilization, Engineering, and Construction in Extreme Environments - Selected Papers from the 17th Biennial International Conference on Engineering, Science, Construction, and Operations in Challenging Environments*, 894–907. <https://doi.org/10.1061/9780784483374.082>
- Heiken, G., Vaniman, D., & French, B. (1992). Lunar sourcebook. A user's guide to the moon. *Endeavour*, 16(2). [https://doi.org/10.1016/0160-9327\(92\)90014-g](https://doi.org/10.1016/0160-9327(92)90014-g)
- Heyman, J. (1966). The stone skeleton. *International Journal of Solids and Structures*, 2(2), 249–256. [https://doi.org/10.1016/0020-7683\(66\)90018-7](https://doi.org/10.1016/0020-7683(66)90018-7)
- Hoshino, T., Wakabayashi, S., Yoshihara, S., & Hatanaka, N. (2016). Key Technology Development for Future Lunar Utilization—Block Production Using Lunar Regolith. *Transactions of the Japan Society for Aeronautical and Space Sciences, Aerospace Technology Japan*, 14(ists30), Pk_35–Pk_40. https://doi.org/10.2322/tastj.14.pk{_}35
- Imhof, B., Urbina, D., Weiss, P., Sperl Waltraut Hoheneder, M., Waclavicek Hemanth Kumar Madakashira, R., Salini, J., Govindaraj, S., Gancet Makthoum Peer Mohamed, J., Gobert Miranda Fateri, T., Meurisse, A., & Lopez Clemens Preisinger, O. (2017). Advancing Solar Sintering for Building A Base On The Moon. *69th International Astronautical Congress (IAC)*.
- Indyk, S. J., & Benaroya, H. (2017). A structural assessment of unrefined sintered lunar regolith simulant. *Acta Astronautica*, 140(September), 517–536. <https://doi.org/10.1016/j.actaastro.2017.09.018>
- Itasca Consulting Group Inc. (2019). 3DEC- Three-Dimensional Distinct Element Code, Ver. 7.0.
- Jablonski, A. M., & Ogden, K. A. (2008). Technical Requirements for Lunar Structures. *Journal of Aerospace Engineering*, 21(2), 72–90. [https://doi.org/10.1061/\(asce\)0893-1321\(2008\)21:2\(72\)](https://doi.org/10.1061/(asce)0893-1321(2008)21:2(72))
- Kalapodis, N., Málaga-Chuquitaype, C., & Kampas, G. (2022). Structural efficiency of varying-thickness regolith-based lunar arches against inertial loading. *Acta Astronautica*, 191. <https://doi.org/10.1016/j.actaastro.2021.11.031>
- Kalapodis, N., Kampas, G., & Ktenidou, O. J. (2020). A review towards the design of extraterrestrial structures: From regolith to human outposts. <https://doi.org/10.1016/j.actaastro.2020.05.038>
- Kalapodis, N., Zalachoris, G., Ktenidou, O. J., & Kampas, G. (2022). On the seismic behaviour of monolithic lunar arches subjected to moonquakes. *Earthquake Engineering and Structural Dynamics*, (September), 1–17. <https://doi.org/10.1002/eqe.3754>
- Kampas, G., Kalapodis, N., McLean, T., & Málaga-Chuquitaype, C. (2021). Limit-state analysis of parabolic arches subjected to inertial loading in different gravitational fields using a variational formulation. *Engineering Structures*, 228. <https://doi.org/10.1016/j.engstruct.2020.111501>

- Karl, D., Cannon, K. M., & Gurlo, A. (2022). Review of space resources processing for Mars missions: Martian simulants, regolith bonding concepts and additive manufacturing. *Open Ceramics*, 9(December 2021), 100216. <https://doi.org/10.1016/j.oceram.2021.100216>
- Khoshnevis, B., & Zhang, J. (2012). Extraterrestrial construction using contour crafting. *23rd Annual International Solid Freeform Fabrication Symposium - An Additive Manufacturing Conference, SFF 2012*.
- Konstantatou, M., Dall'igna, M., Wilkinson, S., Gallou, I., & Piker, D. (2021). Learning lessons from Earth and Space towards Sustainable Multi-planetary Design. *Spool*, 8(2), 39–54. <https://doi.org/10.7480/spool.2021.2.5431>
- Konstantatou, M., Navarro Perez, S. C., Piker, D., Dall'igna, M., & Gallou, I. (2022). Off-Earth infrastructure assembly: A conceptual method for scaffoldless and mortarless component-based structures in static equilibrium. *International Journal of Space Structures*, 37(3), 196–210. <https://doi.org/10.1177/09560599221120032>
- Laot, M., Rich, B., Cheibas, I., Fu, J., Zhu, J.-N., & Popovich, V. A. (2021). Additive Manufacturing and Spark Plasma Sintering of Lunar Regolith for Functionally Graded Materials. *SPOOL*, 8(2), 7–29. <https://doi.org/10.7480/spool.2021.2.5258>
- Lemos, J. V. (2007). Discrete element modeling of masonry structures. *International Journal of Architectural Heritage*, 1(2). <https://doi.org/10.1080/15583050601176868>
- Lemos, J. V. (2019). Discrete element modeling of the seismic behavior of masonry construction. *Buildings*, 9(2). <https://doi.org/10.3390/buildings9020043>
- Lognonné, P., Gagnepain-Beyneix, J., & Chenet, H. (2003). A new seismic model of the Moon: Implications for structure, thermal evolution and formation of the Moon. *Earth and Planetary Science Letters*, 211(1-2), 27–44. [https://doi.org/10.1016/S0012-821X\(03\)00172-9](https://doi.org/10.1016/S0012-821X(03)00172-9)
- Málaga-Chuquitaype, C., McLean, T., Kalapodis, N., Kolonas, C., & Kampas, G. (2022). Optimal arch forms under in-plane seismic loading in different gravitational environments. *Earthquake Engineering & Structural Dynamics*. <https://doi.org/10.1002/eqe.3626>
- Malla, R. B. (1991). Earthbound Civil Engineering Experience for Space Applications. *Journal of Aerospace Engineering*, 4(4), 330–346. [https://doi.org/10.1061/\(asce\)0893-1321\(1991\)4:4\(330\)](https://doi.org/10.1061/(asce)0893-1321(1991)4:4(330))
- Marino, M., Neri, F., Maria, A. D. E., & Borri, A. (2014). Experimental Data of Friction Coefficients for some Types of Masonry and its Correlation with an Index of Quality Masonry (IQM). *Second European Conference on Earthquake Engineering and Seismology*, 1–12.
- McLean, T., Málaga-Chuquitaype, C., Kalapodis, N., & Kampas, G. (2021). OpenArch: An open-source package for determining the minimum-thickness of arches under seismic loads. *SoftwareX*, 15. <https://doi.org/10.1016/j.softx.2021.100731>
- Meurisse, A., Beltzung, J. C., Kolbe, M., Cowley, A., & Sperl, M. (2017). Influence of Mineral Composition on Sintering Lunar Regolith. *Journal of Aerospace Engineering*, 30(4). [https://doi.org/10.1061/\(asce\)as.1943-5525.0000721](https://doi.org/10.1061/(asce)as.1943-5525.0000721)
- Meurisse, A., Makaya, A., Willsch, C., & Sperl, M. (2018). Solar 3D printing of lunar regolith. *Acta Astronautica*, 152. <https://doi.org/10.1016/j.actaastro.2018.06.063>
- Michiels, T., & Adriaenssens, S. (2018). Form-finding algorithm for masonry arches subjected to in-plane earthquake loading. *Computers and Structures*, 195. <https://doi.org/10.1016/j.compstruc.2017.10.001>

- Michiels, T., Adriaenssens, S., & Dejong, M. (2019). Form finding of corrugated shell structures for seismic design and validation using non-linear pushover analysis. *Engineering Structures*, 181. <https://doi.org/10.1016/j.engstruct.2018.12.043>
- Mohanty, R., Kumar, P. S., Raghukanth, S. T., & Lakshmi, K. J. (2020). The Long-Lived and Recent Seismicity at the Lunar Orientale Basin: Evidence From Morphology and Formation Ages of Boulder Avalanches, Tectonics, and Seismic Ground Motion. *Journal of Geophysical Research: Planets*, 125(12). <https://doi.org/10.1029/2020JE006553>
- Mottaghi, S., & Benaroya, H. (2015). Design of a Lunar Surface Structure. II: Seismic Structural Analysis. *Journal of Aerospace Engineering*, 28(1). [https://doi.org/10.1061/\(asce\)as.1943-5525.0000396](https://doi.org/10.1061/(asce)as.1943-5525.0000396)
- Mueller, R. P., Prater, T. J., Roman, M., Edmunson, J. E., Fiske, M. R., & Carrato, P. (2019). NASA Centennial Challenge: Three dimensional (3D) printed habitat, phase 3. *Proceedings of the International Astronautical Congress, IAC, 2019-October*.
- Mueller, R. P., Roman, M. C., & Kim, H. S. (2017). NASA centennial challenge: Three dimensional (3D) printed habitat, phase 2. *Proceedings of the International Astronautical Congress, IAC, 18*.
- Nakamura, Y., Latham, G. V., & Dorman, H. J. (1982). Apollo lunar seismic experiment - final summary. *Journal of Geophysical Research*, 87(Supplement). <https://doi.org/10.1029/jb087is01p0a117>
- Nakamura, Y., Latham, G. V., Dorman, H. J., Ibrahim, A. K., Koyama, J., & Horvath, P. (1979). Shallow moonquakes: Depth, distribution, and implications as to the present state of the lunar interior. *10th Lunar and Planetary Science Conference; 19-23 March 1978; Houston, TX*.
- Nunn, C., Garcia, R. F., Nakamura, Y., Marusiak, A. G., Kawamura, T., Sun, D., Margerin, L., Weber, R., Drilleau, M., Wiczorek, M. A., Khan, A., Rivoldini, A., Lognonné, P., & Zhu, P. (2020). Lunar Seismology: A Data and Instrumentation Review. <https://doi.org/10.1007/s11214-020-00709-3>
- Oberst, J., & Nakamura, Y. (1992). A seismic risk for the lunar base. In NASA. *Johnson Space Center*, 231.
- Ochsendorf, J., & Block, P. (2009). Designing unreinforced masonry. In E. Allen & W. Zalewski (Eds.), *Form and forces: Designing efficient, expressive structures*. John Wiley & Sons.
- Oppenheim, I. J. (1992). The masonry arch as a four-link mechanism under base motion. <https://doi.org/10.1002/eqe.4290211105>
- Robert McNeel & Associates. (2020). Rhinoceros 3D, Version 7.0.
- Roberti, G. M., & Spina, O. (2001). Discrete element analysis on the Sardinian' Nuaraghe. *Proceedings, 3rd International Seminar on Historical Constructions*, 719–727.
- Roberts, A. D., Whittall, D. R., Breitling, R., Takano, E., Blaker, J. J., Hay, S., & Scrutton, N. S. (2021). Blood, sweat, and tears: extraterrestrial regolith biocomposites with in vivo binders. *Materials Today Bio*, 12(June), 100136. <https://doi.org/10.1016/j.mtbio.2021.100136>
- Ruess, F., Schaenzlin, J., & Benaroya, H. (2006). Structural Design of a Lunar Habitat. *Journal of Aerospace Engineering*, 19(3), 133–157. [https://doi.org/10.1061/\(asce\)0893-1321\(2006\)19:3\(133\)](https://doi.org/10.1061/(asce)0893-1321(2006)19:3(133))
- Ruiz, S., Cruz, A., Gomez, D., Dyke, S. J., & Ramirez, J. (2022). Preliminary approach to assess the seismic hazard on a lunar site. *Icarus*, 383, 115056. <https://doi.org/https://doi.org/10.1016/j.icarus.2022.115056>
- Sanders, G. B., & Larson, W. E. (2013). Progress Made in Lunar In Situ Resource Utilization under NASA's Exploration Technology and Development Program. *Journal of Aerospace Engineering*, 26(1), 5–17. [https://doi.org/10.1061/\(asce\)as.1943-5525.0000208](https://doi.org/10.1061/(asce)as.1943-5525.0000208)

- Spedding, C. P., Nuttall, W. J., & Lim, S. (2020). Energy requirements of a thermally processed ISRU radiation shield for a lunar habitat. *Advances in Space Research*, 65(11), 2467–2474. <https://doi.org/10.1016/j.asr.2020.03.015>
- Steiner, J. T., & Malla, R. B. (2022). A Study of Layered Structural Configurations as Thermal and Impact Shielding of Lunar Habitats. (2021), 1297–1309.
- Steurer, W. (1982). Extraterrestrial Materials Processing. *JPL Publication 82-41*.
- Todisco, L., Sanitate, G., & Lacorte, G. (2017). Geometry and Proportions of the Traditional Trulli of Alberobello. *Nexus Network Journal*, 19(3), 701–721. <https://doi.org/10.1007/s00004-016-0326-4>
- Venerito, M., Foti, D., & Vitti, M. (2017). On the Static and Dynamic Behavior of a Prehistoric Structure Typical of Apulia in Italy. *Procedia Engineering*, 180, 480–490. <https://doi.org/10.1016/J.PROENG.2017.04.207>
- Warren, P., Raju, N., Ebrahimi, H., Krsmanovic, M., Raghavan, S., Kapat, J., & Ghosh, R. (2022). Effect of sintering temperature on microstructure and mechanical properties of molded Martian and Lunar regolith. *Ceramics International*, 48(23), 35825–35833. <https://doi.org/10.1016/j.ceramint.2022.07.329>
- Watters, T. R., Weber, R. C., Collins, G. C., Howley, I. J., Schmerr, N. C., & Johnson, C. L. (2019). Shallow seismic activity and young thrust faults on the Moon. *Nature Geoscience*, 12(6), 411–417. <https://doi.org/10.1038/s41561-019-0362-2>
- Wendland, D. (2007). Traditional Vault Construction Without Formwork: Masonry Pattern and Vault Shape in the Historical Technical Literature and in Experimental Studies. *International Journal of Architectural Heritage - INT J ARCHIT HERIT*, 1, 311–365. <https://doi.org/10.1080/15583050701373803>
- Yazici, S. (2018). Building in Extraterrestrial Environments: T-Brick Shell. *Journal of Architectural Engineering*, 24(1). [https://doi.org/10.1061/\(asce\)ae.1943-5568.0000293](https://doi.org/10.1061/(asce)ae.1943-5568.0000293)
- Zhou, C., Tang, B., Ding, L., Sekula, P., Zhou, Y., & Zhang, Z. (2020). Design and automated assembly of Planetary LEGO Brick for lunar in-situ construction. *Automation in Construction*, 118, 103282. <https://doi.org/10.1016/j.autcon.2020.103282>

Appendix A

ADDENDA FOR CHAPTER VI

1.1 Subcontact density variation

As mentioned in Chapter 6.2.3, differences in pushover behaviour between simple and complex components appear to be attributable to differences in subcontact density, which arise from the geometry of the component variants. A larger number of edges—deriving from the presence of grooves—in the complex components results in the generation of more subcontacts, which leads to lower stiffness. Therefore, initial attempts to match the behaviour of the simple component vault with the complex component vault were based on increasing the number of subcontacts in the simple components. This was done by specifying the maximum edge length between individual subcontacts. Several different values for maximum edge length were specified for a partial vault model with fifty courses, and pushover analyses were conducted for each case according to the methodology outlined in Chapter 4. The most favourable match was obtained for an edge length of 0.2 m, for which the results are presented in Figure A.1.

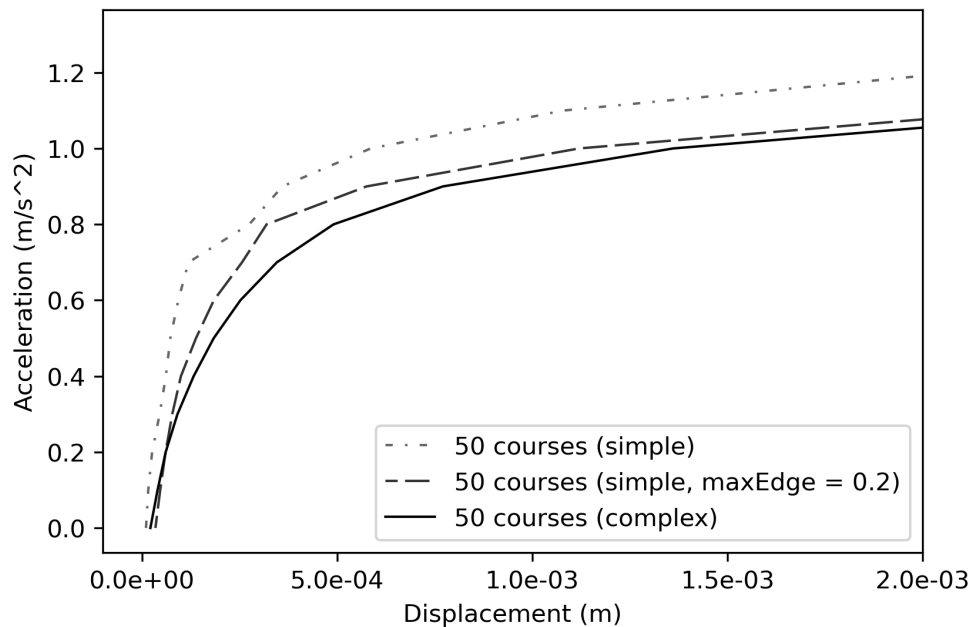


Figure A.1: Matching simple and complex component behaviour through subcontact edge length

This figure contains three pushover plots corresponding to a model with simple components, a model with complex components, and a model with modified simple components with an edge length equal to 0.2 m. The simple component variant has the stiffest response and the complex component variant has the most flexible response. The plot for the modified simple components lies between the other two. This figure illustrates how the pushover behaviour of the simple component vault can be modified to better approximate

the complex component behaviour by specifying an edge length of 0.2 m. Although favourable matching of the behaviour of the simple and complex components could be achieved using this approach, increasing the number of subcontacts greatly increases the computational overhead, making it infeasible for use with full-scale vault models.

1.2 Local stability analysis

The mechanical interlocking mechanism maintains the structural integrity of incomplete courses by confining the pins of each component to remain within the grooves of components in the course below. There is limited indication that local stability of individual components may be an issue during assembly of each course in the vault, except for models with nearly-vertical courses. At a sufficiently steep inclination, overturning of components may occur, but for the inclination of 45° assumed for the final vault model, such instability is not expected. Still, preliminary analysis was carried out for one representative course in order to affirm the stability of incomplete courses.

In order to conduct the preliminary local stability analysis, a simplified modelling approach was taken, which examines one incomplete course and assesses its stability as components are added from the ground up. Furthermore, the simplified approach does not account for how during fabrication, the settlement of each component will have a slight influence on the initial position of the following component; in reality, each block will experience a small degree of settlement from its originally-modelled position based on pin tolerances or gaps between components. Therefore, in order to accurately model the brick-wise assembly of a course, the model would have to be imported back into the geometric constraint solving algorithm defined in Chapter 3 after the settlement of each component, where the position of the subsequent component would be simulated. Then, the model would be translated back to the 3DEC environment, where the newly added component would be allowed to settle. This type of recursive modelling and analysis is out of the scope of this project, but the local stability of a newly-placed component can be approximately illustrated by removing components that follow it in the assembly process, and subjecting the resulting partial course to vertical gravity loading.

In other words, the simplified local stability analysis is carried out as follows: the ten-course vault model from Chapter 6.2.3 is modified such that the first nine courses are fixed in place; components from the outermost course are removed one-by-one from each side of the vault, starting at the top, with a new model being created each time a pair of components is removed. This process results in a series of models that represent the progression of course assembly in reverse. A reasonable assembly approach would begin by fixing the first component in each leg of the new course, as established in Chapter 4, then placing components symmetrically along each leg until the course is complete. This progression of assembly steps is illustrated for four representative phases in Figure A.2.

Each of the models from Figure A.2 is analysed in 3DEC under the influence of self-weight, with equilibrium conditions based on those defined in Chapter 4. Figure A.3 contains contour plots of displacement magnitude for each of the models, as well as velocity magnitude vectors. The largest of these vectors is $4.7\text{E-}04$, which is lower than the equilibrium threshold of $1.0\text{E-}03 \text{ m s}^{-1}$, indicating that the components are stable

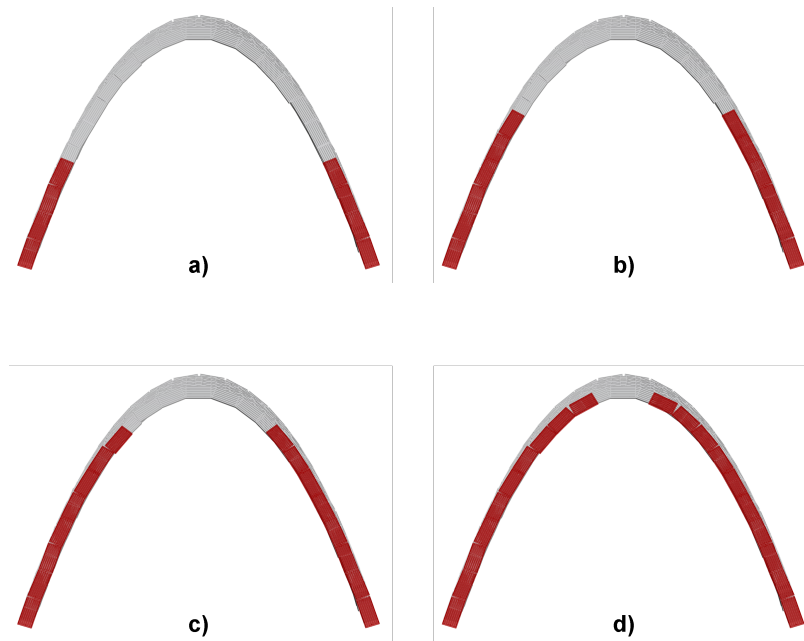


Figure A.2: Models with partially completed courses; a) 8 components; b) 12 components; c) 16 components; d) 20 components

during each phase. Although these results are specific to a single course in the vault, other courses do not deviate significantly in their configuration and are expected to behave similarly. Therefore, local instability during assembly is unlikely to be an issue for any component in the vault.

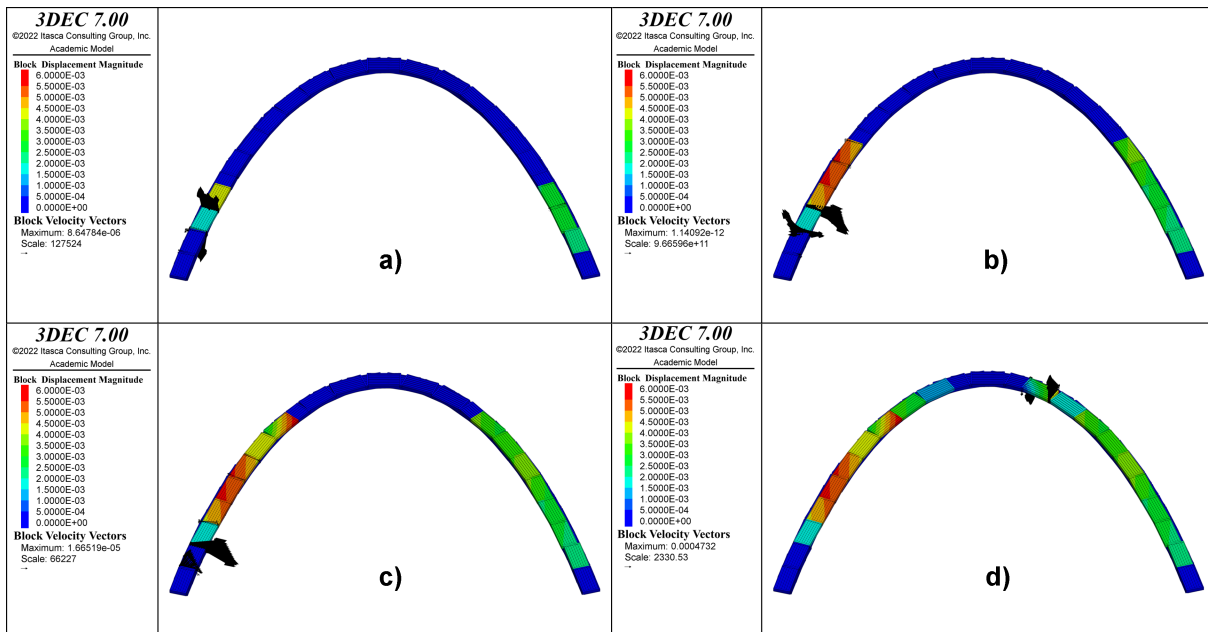


Figure A.3: Equilibrium under self-weight for models with partially completed courses; a) 8 components; b) 12 components; c) 16 components; d) 20 components

Appendix B

ADDENDA FOR CHAPTER VIII

2.1 Preliminary analysis with tetrahedral mesh

The analyses carried out in Chapter 8 are based on a hexahedral meshing of the equivalent monolithic vault geometry, which was chosen because tetrahedral elements yielded questionable results. This is evidenced by Figure B.1, which is a contour plot of principal stresses in a vault meshed with 0.25 m tetrahedral elements. This figure represents the stress state in the load step preceding failure, which results from the analysis approach described in Chapter 8.2.3. According to this analysis, the vault failed at a lateral acceleration of 2.9 m s^{-2} , which corresponds to a Load Factor of 0.58. In this figure, isolated elements show signs of stress concentration, even though a more uniform distribution of stresses is expected. Upon further consideration, it becomes clear that the results obtained for a tetrahedral mesh are likely to be inaccurate due to the tendency of first-order tetrahedral elements to experience shear locking. When loaded with a lateral acceleration, the legs of the vault are expected to experience bending due to the fixed boundary conditions at the ground surface, which can lead to significant shear locking with tetrahedral elements. According to Danielson (2014), "...tetrahedral elements generally perform very poorly, such as pathologically exhibiting shear locking in flexure..." (pg. 161). This observation would explain the higher acceleration capacity reported for the vault with tetrahedral elements, which are considered to be significantly unconservative.

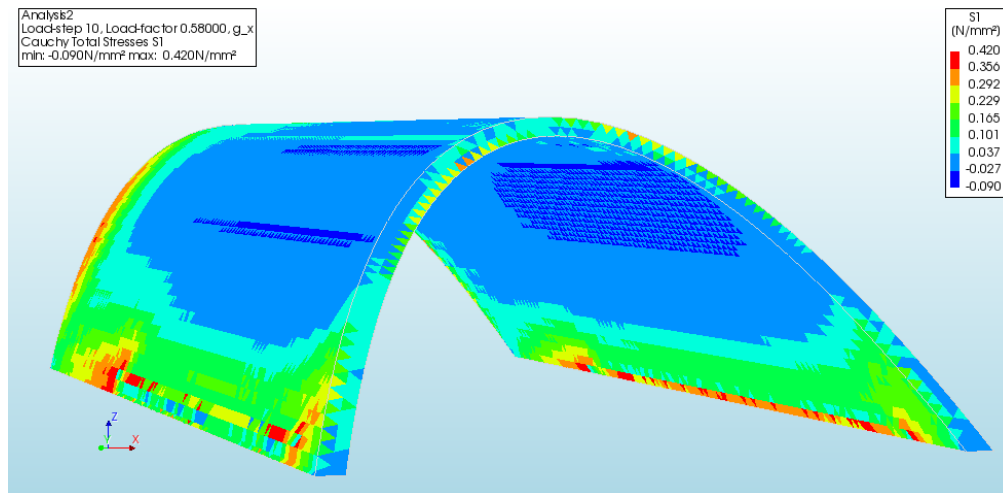


Figure B.1: Principal stress contour plot at onset of failure in vault modelled with tetrahedral elements

The contour plot of principal stresses for a mesh with hexahedral elements, pictured in Figure B.2 does not demonstrate the discontinuities seen in the tetrahedral mesh and produces a more continuous stress distribution that is expected to be more accurate. The lateral acceleration at which the vault fails is significantly lower than for the tetrahedral mesh, with failure occurring at an acceleration of 1.9 m s^{-2} . This result indicates that the original tetrahedral mesh produced significantly unconservative results, which are

likely the result of shear locking. Shear locking also occurs to some degree when using linear hexahedral elements, but its influence can become negligible with a sufficiently high mesh density. Furthermore, higher accuracy can be achieved using second order elements, which would further mitigate the influence of shear locking. Based on the above considerations, hexahedral elements were deemed to be more appropriate for the analysis in Chapter 8. The element size was established after studying the influence of mesh refinement.

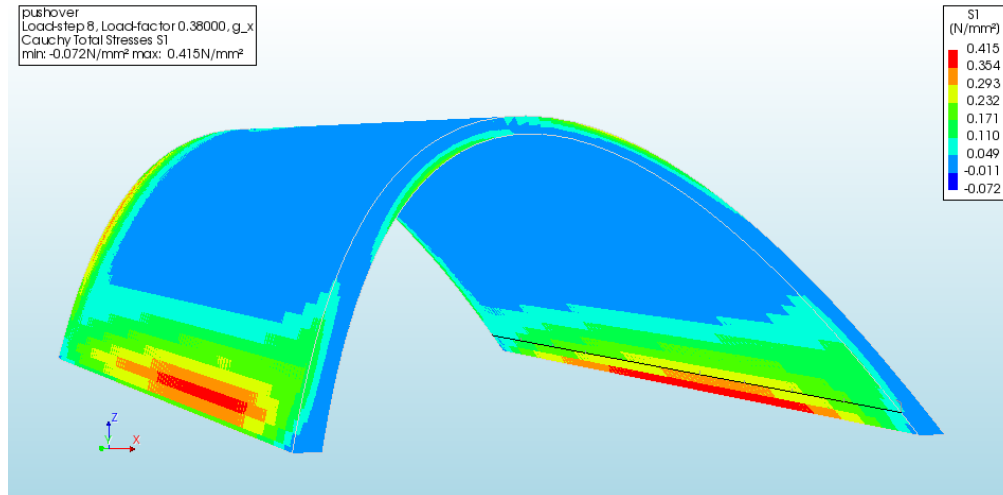


Figure B.2: Principal stress contour plot at onset of failure in vault modelled with hexahedral elements

2.2 Mesh refinement study

A basic mesh refinement study was carried out in order to determine what mesh size is needed to accurately represent the stresses in the vault. Element sizes of 0.125 m, 0.100 m, and 0.0750 m are considered aside from the initial mesh size of 0.250 m. Further refinement was not feasible due to computational constraints caused by the large model size. The smallest element size resulted in a mesh with 573,901 elements, and any further refinement resulted in an overload of available memory on the machine used for analysis. For each mesh variant, a lateral acceleration of 1.0 m s^{-2} was applied in a linear elastic analysis and the global maximum principal tensile stress was recorded, as well as the maximum stress at a height of 0.5 m above the support plane, as indicated by the contour probe curve in Figure B.2. This probe curve was chosen in order to study a region where the influence of artificial stress concentrations, which may arise from boundary conditions, is avoided. The results of the mesh refinement study are reported in Table B.1.

The mesh convergence plot shown in Figure B.3 indicate that stress concentrations do not appear to be present, since the global maximum principal tensile stress shows signs of convergence. In this figure, the maximum principal tensile stress, S_1 , is plotted as a function of the number of elements. The labels at each data point indicate the element size. The tendency toward convergence is evident from the decrease in slope between the two smallest mesh sizes, 0.1 m and 0.0750 m. Still, the change in maximum principal stress between these element sizes is 11%, which is quite large. This indicates that further mesh refinement may be necessary and that the results may be unconservative. Due to computational limitations, smaller mesh

Desired element size (m)	Global maximum principal tensile stress (MPa)	Maximum principal tensile stress along probe curve (MPa)
0.250	0.207	0.115
0.125	0.239	0.123
0.100	0.266	0.120
0.0750	0.295	0.121

Table B.1: Maximum principal stresses for different element sizes

sizes could not be implemented, however. Without data for a mesh size smaller than 0.0750 m, the results of the mesh refinement study are considered to be inconclusive, although they suggest that an element size of 0.0750 m will produce the most accurate results.

It is possible that a more robust meshing scheme can be more memory-efficient by increasing the mesh density in key parts of the vault while using a coarser mesh in other parts, but this is out of the scope of the project. The possibility of this approach is justified by the results shown in Table B.1, which show that the principal tensile stress along the probe curve seems to converge for an element size between 0.125 m and 0.100 m.

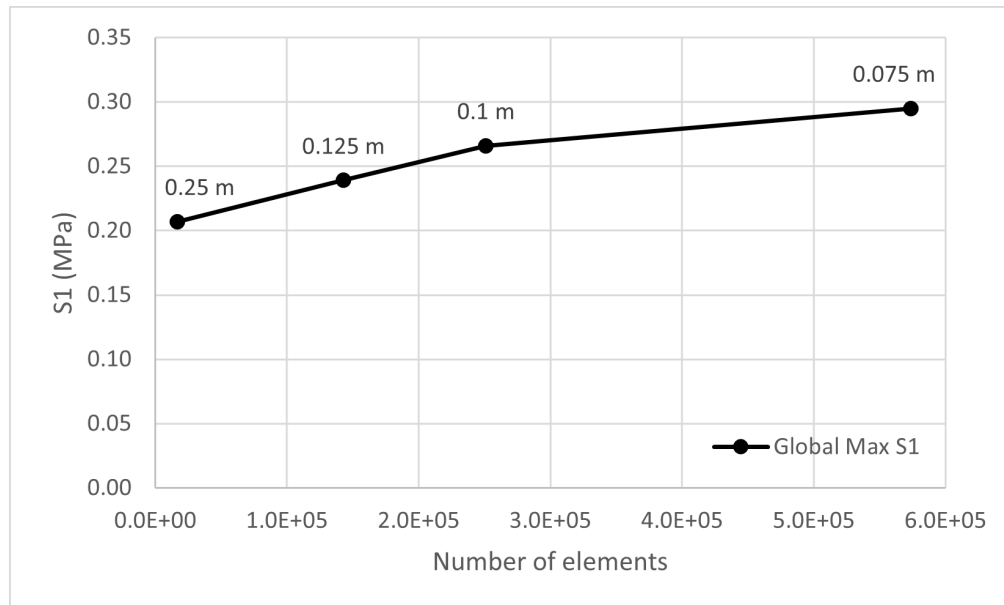


Figure B.3: Mesh convergence plot